

AD-A252 632



WL-TR-91-4149

**MECHANICAL PROPERTIES FOR
ADVANCED ENGINE MATERIALS**

**N. Ashbaugh, M. Khobaib, R. John, et al.
University of Dayton Research Institute
300 College Park
Dayton, Ohio 45469-0001**

April 1992

Final Report for Period 27 August 1987 - 17 May 1991

Approved for public release; distribution is unlimited.

**MATERIALS DIRECTORATE
WRIGHT LABORATORY
AIR FORCE SYSTEMS COMMAND
WRIGHT-PATTERSON AIR FORCE BASE, OHIO 45433-6533**



**DTIC
SELECTE
JUL 09 1992
S B D**

92 7 0 0 16

92-17883

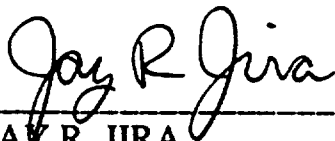


NOTICE

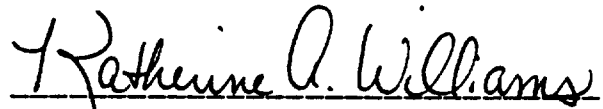
When Government drawings, specifications, or other data are used for any purpose other than in connection with a definitely government-related procurement, the United States Government incurs no responsibility or any obligation whatsoever. The fact that the government may have formulated or in any way supplied the said drawings, specifications, or other data, is not to be regarded by implication or otherwise in any manner construed, as licensing the holder or any other person or corporation; or as conveying any rights or permission to manufacture, use, or sell any patented invention that may in any way be related thereto.

This report is releasable to the National Technical Information Service (NTIS). At NTIS, it will be available to the general public, including foreign nations.

This technical report has been reviewed and is approved for publication.



JAY R. JIRA
Project Engineer
Materials Behavior Branch
Metals and Ceramics Division



KATHERINE A. WILLIAMS
Technical Area Manager
Materials Behavior Branch
Metals and Ceramics Division



ALLAN W. GUNDERSON, Chief
Materials Behavior Branch
Metals and Ceramics Division

If your address has changed, if you wish to be removed from our mailing list, or if the addressee is no longer employed by your organization, please notify WL/MLLN, Wright-Patterson AFB OH 45433-6533 to help us maintain a current mailing list.

Copies of this report should not be returned unless return is required by security considerations, contractual obligations, or notice on a specific document.

REPORT DOCUMENTATION PAGE			Form Approved OMB No. 0704-0188	
Public reporting burden for this collection of information is estimated to average 1 hour per response, including the time for reviewing instructions, searching existing data sources, gathering and maintaining the data needed, and completing and reviewing the collection of information. Send comments regarding this burden estimate or any other aspect of this collection of information, including suggestions for reducing this burden, to Washington Headquarters Services, Directorate for Information Operations and Reports, 1215 Jefferson Davis Highway, Suite 1204, Arlington, VA 22202-4302, and to the Office of Management and Budget, Paperwork Reduction Project (0704-0188), Washington, DC 20503.				
1. AGENCY USE ONLY (Leave blank)		2. REPORT DATE April 1992		3. REPORT TYPE AND DATES COVERED Final, 27 Aug 87 - 17 May 91
4. TITLE AND SUBTITLE Mechanical Properties for Advanced Engine Materials			5. FUNDING NUMBERS F33615-87-C-5243 PE: 61102F/62102F PR: 2302 TA: P1 WU: 02	
6. AUTHOR(S) N.E. Ashbaugh, M. Khobaib, G.A. Hartman, D. Coker J.L. Kroupa, R. John, K. Jata, D.A. Johnson, D.C. Maxwell, D.A. Stubbs, R.C. Goodman, B.R. Kortyna and A.C. Cheney				
7. PERFORMING ORGANIZATION NAME(S) AND ADDRESS(ES) University of Dayton Research Institute 300 College Park Dayton, Ohio 45469-0001			8. PERFORMING ORGANIZATION REPORT NUMBER UDR-TR-91-149	
9. SPONSORING/MONITORING AGENCY NAME(S) AND ADDRESS(ES) Jay R. Jira (513) 255-1358 Materials Directorate (WL/MLLN) Wright Laboratory Wright-Patterson Air Force Base, Ohio 45433-6533			10. SPONSORING/MONITORING AGENCY REPORT NUMBER WL-TR-91-4149	
11. SUPPLEMENTARY NOTES				
12a. DISTRIBUTION / AVAILABILITY STATEMENT Approved for public release; distribution is unlimited.			12b. DISTRIBUTION CODE	
13. ABSTRACT (Maximum 200 words) The experimental evaluation of advanced mechanical properties that characterize the behavior of emerging materials for aerospace structures under a broad range of conditions representative of those encountered in service was emphasized in this investigation. The information guided the development of life prediction methodologies which are based on the concept of damage tolerance as a design philosophy. The research effort was subdivided into four interrelated tasks -- a) material characterization tests, b) experimental procedure and test developments, c) analytical and modeling developments, and d) test support activities and data archival. Material characterization tests for fatigue, creep, and crack growth responses were conducted on a titanium matrix composite reinforced with continuous SiC fibers and fabricated from a foil-fiber-foil layup. The molybdenum wire used in the weaving of the fiber mats was a major factor in the development of damage under fatigue and creep test conditions. A model ceramic matrix composite composed of an aluminosilicate glass matrix and SiC fiber tows provided some interesting fatigue and fracture toughness responses. Behavior of monolithic materials were evaluated under creep, creep crack growth, fatigue crack growth, and oxidation conditions. Significant developments in test procedures and systems have been accomplished with emphasis on conducting thermomechanical fatigue (TMF) tests. TMF capabilities and associated software computer control have been developed for inert and laboratory air servo-hydraulic test systems and pneumatic/resonance actuated systems. Low cycle fatigue and high frequency test capabilities were enhanced with hardware and software developments. Test techniques were upgraded in areas of laser displacement measurement, ultrasonic detection of small cracks, and application of DC electric potential. Finite element and finite difference techniques have been applied to the analysis of composite and monolithic material responses. Residual stresses arising from processing conditions and subsequent fiber and matrix stress distributions from TMF loading conditions were investigated. Various analytical results for cracks, surface and embedded flaws, fiber pullout, deeply notched geometry, and electrical potential response have also been obtained. In addition to the research activities, material characterizations have been conducted following standard test procedures. Computer hardware has been assembled and procedures developed to archive and to maintain the laboratory data for future access and use.				
14. SUBJECT TERMS Metal Matrix Composite, Ceramic Matrix Composite, Titanium Aluminide, Thermal Fatigue, Fatigue Crack Growth, Thermomechanical Fatigue, Creep Rupture, Creep Crack Growth, Tensile Test, Oxidation, Modeling, Analysis			15. NUMBER OF PAGES 168	
			16. PRICE CODE	
17. SECURITY CLASSIFICATION OF REPORT Unclassified	18. SECURITY CLASSIFICATION OF THIS PAGE Unclassified	19. SECURITY CLASSIFICATION OF ABSTRACT Unclassified	20. LIMITATION OF ABSTRACT UL	

FOREWORD

The work described in this report was performed at the Materials Behavior Branch, Metals and Ceramics Division, Materials Directorate, Wright Laboratory (WL/MLLN) under Contract No. F33615-87-C-5243, "Research on Mechanical Properties for Advanced Engine Materials." The contract was administered under the direction of WL by Mr. Jay Jira (MLLN). The program was conducted by the Structural Integrity Division, University of Dayton Research Institute, Dayton, Ohio, with Dr. Noel E. Ashbaugh acting as the Principal Investigator and Dr. Joseph P. Gallagher acting as the Program Manager.

The investigations were conducted by Drs. Noel E. Ashbaugh, M. Khobaib, Reji John, Kumar Jata, and Messrs. George Hartman, Demirkan Coker, David Stubbs, Joseph Kroupa, David Johnson, and Scott Munro, and Ms. Bonnie Kortyna. Generation of the data was accomplished in part by Messrs. Richard Goodman, David Maxwell, George Ahrens, Richard Kleismit, Andrew Lackey, Austin Cheney, Kenneth Goecke, Thomas Carner, Timothy Johnson, and Ms. Debbie Garner. Assistance in data reduction, computer programming, fabrication of fixtures, and assembling mechanical and electrical components was provided by Messrs. Mark Flannery, Jeffrey Hanrahan, Norman Schehl, Mark Mrazek, Brian Coty, Paul Stibich, and Jeffrey Butkiewicz. Mrs. LaVonna Stathes was responsible for the typing of this document. This work was conducted during the period 27 August 1987 to 17 May 1991.

Accession For	
NTIS GRA&I	<input checked="checked" type="checkbox"/>
DTIC TAB	<input type="checkbox"/>
Unannounced	<input type="checkbox"/>
Justification	
By	
Distribution/	
Availability Codes	
Dist	Avail and/or Special
A-1	

TABLE OF CONTENTS

	PAGE
LIST OF FIGURES	viii
LIST OF TABLES	xi
SECTION 1 - INTRODUCTION	1
SECTION 2 - MATERIAL CHARACTERIZATION TESTS	4
2.1 Metal Matrix Composite (MMC): SCS-6/Ti-24Al-11Nb	4
2.1.1 Fatigue	4
2.1.2 Creep	5
2.1.3 Fatigue Crack Growth Behavior	12
2.1.4 Residual Stress Measurement	15
2.1.5 Fractographic Characterization	15
2.2 Ceramic Matrix Composite (CMC): SiC/1723	16
2.2.1 Fatigue	16
2.2.2 Tensile and Creep Behavior	17
2.2.3 Fatigue Crack Growth Behavior	17
2.2.4 Fracture Toughness	18
2.3 Monolithic Materials	19
2.3.1 Creep Behavior of Ti-24Al-11Nb	19
2.3.2 Creep Crack Growth	22
2.3.2.1 Ti-24Al-11Nb	24
2.3.2.2 Ti-1100	24
2.3.3 Fatigue Crack Growth	25
2.3.3.1 Ti-24Al-11Nb	25
2.3.3.2 IN 718	26
2.3.3.3 Alumina	27
2.3.3.4 2024-T351 Al Crack Opening/Closure Study	27
2.3.4 Oxidation Behavior of Ti ₃ Al Alloys	32
SECTION 3 - EXPERIMENTAL PROCEDURE AND TEST DEVELOPMENTS	33
3.1 Test System Developments	33
3.1.1 Thermal Cycling System	33
3.1.2 TMF Upgrade of Schenck System	34
3.1.3 High Frequency Systems	34
3.1.3.1 C-20 System Developments	34
3.1.3.2 Unholtz-Dickie Test System	35
3.1.4 TMF Vacuum System	36
3.1.5 TMF Horizontal Test Systems	37

3.1.6	LCF Test System	37
3.2	Technique Development	38
3.2.1	Automation Software Upgrades	38
3.2.2	Load-Pin-Size Effects for C(T) Specimen	38
3.2.3	Laser Interferometric Displacement Gage (LIDG) Upgrade	38
3.2.4	Application of LIDG System at Elevated Temperature	40
3.2.4.1	Displacement Measurement in Metals and MMCs	41
3.2.4.2	Displacement Measurement in a Brittle Matrix and CMCs	43
3.2.5	Ultrasonic Detection of Short Cracks	43
3.2.6	DCEPD Measurement of Short Cracks	47
SECTION 4 - ANALYTICAL AND MODELING DEVELOPMENTS		49
4.1	Elementary Elasticity Solutions	49
4.1.1	Uniaxial Model	49
4.1.2	Disk and Concentric Cylinder Models	51
4.1.3	Analysis for Orthotropic CTE	56
4.1.4	Closure Model	59
4.2	Finite Difference Technique for Elastic-Plastic Analysis	59
4.2.1	Model for Unidirectional Composite	60
4.2.2	Results for an MMC	65
4.2.2.1	Material Processing	67
4.2.2.2	Cyclic Mechanical Loads	69
4.2.2.3	Cyclic Thermal Conditions	69
4.2.2.4	Thermomechanical Fatigue	72
4.3	Finite Element Technique	78
4.3.1	Models for Unidirectional Composite	78
4.3.2	Results for Thermal Changes	82
4.3.2.1	Material Processing	84
4.3.2.2	Cyclic Thermal Conditions	88
4.3.2.3	Combinations of Fiber and Matrix Constituents	88
4.3.3	Results for Axial Loads and Thermal Changes	90
4.3.3.1	Cyclic Mechanical Loads	90
4.3.3.2	Thermomechanical Fatigue	90
4.3.4	Results for Transverse Loading	92
4.3.4.1	Perfect Interface Bond	95
4.3.4.2	Frictionless Sliding Interface	95
4.3.4.3	Transverse Response at Room and Elevated Temperature	99
4.4	Elasticity Results for Cracked Geometries	102
4.4.1	Center Cracked Panel, M(T)	102
4.4.1.1	K and Displacement Values for Selected Boundary Conditions	102
4.4.1.2	Singularity Simulation	105
4.4.1.3	Crack Length versus Compliance	105
4.4.2	Single Edge Cracked Strip, SE(T)	108
4.4.3	Middle Cracked Disk, DM(C)	108
4.4.4	Weight Function Analysis of C(T)	111
4.5	Review of Laminate Analyses	118
4.6	Crack Near Interface in 2-D Composite	122
4.7	Fiber Pullout Analysis	122

4.8	Surface and Embedded Flaws in Unidirectional Composites	125
4.9	Elastic-Plastic Analysis of Deeply Notched Tensile Specimen	126
4.10	Electric Potential Analysis of C(T)	126
SECTION 5 - DATA ARCHIVAL AND TEST SUPPORT ACTIVITIES		137
5.1	Mechanical Property Data	137
5.1.1	Coefficient of Thermal Expansion (CTE)	137
5.1.1.1	Uniaxial Test Procedure	137
5.1.1.2	Results for Ti-24Al-11Nb Foil	138
5.1.2	Tensile Behavior of Titanium Aluminides	142
5.1.3	R-Curve of Particulate Composite	145
5.1.4	Fragmentation Test for MMC	145
5.1.5	S-N Behavior of Titanium Alloy	145
5.1.6	Tensile Properties of Fibers	146
5.1.7	K_{IC} of Titanium Aluminides and Particulate Composite	146
5.1.8	Fatigue Crack Growth of Titanium Alloys	146
5.2	Electronics Fabrication	147
5.3	SiC/1723 Processing	147
5.4	Data Maintenance	147
BIBLIOGRAPHY		149

LIST OF FIGURES

FIGURE	CAPTION	PAGE
2.1.2-1	Fractograph showing the deformation modes in the matrix during creep of SCS-6/Ti-24Al-11Nb composite: a) at 650°C and b) at 760°C.	7
2.1.2-2	Fractograph showing evidence of grain boundary sliding in the matrix during creep of SCS-6/Ti-24Al-11Nb composite at 815°C.	8
2.1.2-3	Fractograph showing evidence of extensive slip in the matrix during creep of SCS-6/Ti-24Al-11Nb composite at 815°C.	8
2.1.2-4	Fractograph showing evidence of grain boundary sliding and microvoid coalescence in the matrix during creep of SCS-6/Ti-24Al-11Nb at 815°C.	9
2.1.2-5	Higher magnification view of the evidence of microvoid coalescence.	9
2.1.2-6	Evidence of extensive slip activity in the matrix during creep of SCS-6/Ti-24Al-11Nb at 815°C.	10
2.1.2-7	Higher magnification view of slip traces shown in Fig. 2.1.2-6.	10
2.1.2-8	TEM micrograph showing absence of debonding.	11
2.1.2-9	TEM micrograph showing initial stage of debonding between the carbon layers.	11
2.1.2-10	TEM micrograph showing evidence of void formation in reaction zone.	13
2.1.2-11	Evidence of dislocation loops and long intersecting dislocation.	13
2.1.2-12	Evidence of dislocation activity on nonbasal planes.	14
2.2.4-1	Damage characterization using fluorescent dye penetrants in CMCs.	20
2.3.1-1	Round bar tensile creep specimen.	21
2.3.1-2	Dislocation structure generated during creep of Ti-24Al-11Nb at 650°C.	23
2.3.1-3	Evidence of nonbasal slip activity during creep of Ti-24Al-11Nb at 650°C.	23
2.3.3.3-1	Schematic of the DM(C) geometry.	28
2.3.3.4-1	Comparison of closure loads obtained from BFS and fracture surface striation spacings.	30
2.3.3.4-2	Comparison of closure loads obtained from IDG, BFS and fracture surface striation spacings.	31
3.2.4.1-1	Schematic of optical paths in laser interferometric displacement gage.	42
3.2.4.2-1	Schematic of the tabs glued across the notch on a specimen.	44
3.2.5-1	Processed amplitude of reflected signal from a short crack.	46
3.2.6-1	DCEPD relay unit for short crack detection.	48
4.1.1-1	Models used in the Analysis of Unidirectional Composites.	50

4.1.3-1	Stress state in a hollow cylinder with orthotropic CTE, in plane stress subjected to a uniform temperature change.	58
4.2.1-1	(a) Concentric cylinder idealization of a unidirectional composite, (b) Representative volume element of a unidirectional composite represented by the concentric cylinder model.	61
4.2.1-2	Elastic-Plastic Algorithm.	63
4.2.1-3	Comparison of the stresses at the fiber/matrix interface for a model material during cool down from processing temperature as predicted by FIDEP and the Finite Element Analysis.	64
4.2.2-1	Responses of fiberless Ti-24Al-11Nb foil at room and elevated temperatures and the bilinear approximations uniaxial stress-strain.	66
4.2.2.1-1	Stresses in the matrix at the fiber/matrix interface during cool down from processing temperature for SCS-6/Ti-24-11 composite.	68
4.2.2.2-1	Loading history for (a) room temperature and (b) 650°C isothermal fatigue simulations.	70
4.2.2.2-2	Applied stress versus mechanical strain in the matrix at the fiber/matrix interface for isothermal loading.	71
4.2.2.3-1	Predicted stresses in the matrix at the fiber/matrix interface and the yield surface prior to strain hardening for thermal cycling between 600°C and 150°C.	73
4.2.2.3-2	Predicted axial stress versus predicted mechanical strain for isothermal fatigue and thermal fatigue cases.	74
4.2.2.4-1	Loading history for in-phase and out-of-phase thermomechanical fatigue simulation.	75
4.2.2.4-2	Stress distribution in the composite at (a) 150°C and (b) 650°C for out-of-phase loading.	76
4.2.2.4-3	Predicted axial stresses in the matrix at the fiber/matrix interface as a function of number of steps.	77
4.2.2.4-4	Predicted axial stress peaks in the fiber for in-phase and out-of-phase loading as a function of number of steps.	79
4.2.2.4-5	Comparison of predicted load-displacement traces after two cycles and experimental load-displacement traces after several hundred cycles for SCS-6/Ti-24-11 composite.	80
4.3.1-1	Concentric cylinder and unit cell representation of MMCs.	81
4.3.1-2	Temperature dependent material properties of titanium aluminide Ti-24Al-11Nb [Titanium Aluminide Composites].	83
4.3.2.1-1	Process induced residual stress prediction at room temperature with concentric cylinder model.	85
4.3.2.1-2	Matrix stress at the fiber/matrix interface (pt a) during initial cool down from initial processing temperature.	86
4.3.2.1-3	Process induced residual effective stress at room temperature with square and rectangular unit cell models.	87
4.3.2.2.-1	Cyclic thermal with constant axial stress loading and associated matrix stress history at fiber/matrix interface (pt a).	89
4.3.3.1-1	Cyclic axial stress with constant thermal loading and associated matrix stress history at fiber/matrix interface (pt a).	91
4.3.3.2-1	In-phase TMF loading and associated axial stress history in fiber and matrix.	93

4.3.3.2-2	Out-of-phase TMF loading and associated axial stress history in fiber and matrix.	94
4.3.4.1-1	Transverse response with a perfectly bonded fiber/matrix interface.	96
4.3.4.1-2	Effective stress state of square unit cell with perfectly bonded fiber/matrix interface with application of transverse load (stress in MPa).	97
4.3.4.2-1	Transverse response with a perfectly bonded and frictionless sliding fiber/matrix interface.	98
4.3.4.2-2	Equivalent stress state of square unit cell with frictionless sliding fiber/matrix interface with application of transverse load (stress in MPa).	100
4.3.4.3-1	Transverse response at room and elevated temperature with a sliding fiber/matrix interface and residual stress.	101
4.4.1.1-1	Geometry and load conditions for short M(T) specimen.	103
4.4.1.3-1	Models of laboratory test specimens.	106
4.4.3-1	K_I geometry correction factor for the DM(C) geometry.	110
4.4.3-2	Crack length versus compliance relationship for the DM(C) geometry.	112
4.4.4-1	Schematic of the C(T) geometry.	113
4.4.4-2	Stress distribution along the x-axis in an uncracked C(T).	116
4.4.4-3	Error between the weight function method, K_{WF} and ASTM expression, K_{ASTM} .	117
4.7-1	Fiber pull-out geometry (dimensions in mm).	123
4.7-2	Resulting matrix stress profile at fiber/matrix interface near the crack tip.	124
4.9-1	Notched tension test specimen.	127
4.9-2	Uniaxial stress-strain response of niobium-silicide at room temperature.	128
4.9-3	Stress profile and failure criterion parameters on notched plane ($z = 0$).	129
4.10-1	Compact specimen with "+" as current source locations and "-" as electric potential probe locations. (dimensions in mm)	131
4.10-2	Experimental electric potential calibration curves and base-line finite element solution.	132
4.10-3	Electric potential probe location shifts (± 0.7 mm) and resulting electric potential deviation from base-line electric potential.	133
4.10-4	Current source location shifts and resulting electric potential deviations from base-line electric potential.	134
4.10-5	Nonuniform temperature distribution and resulting electric potential deviation from baseline electric potential.	136
5.1.1.1-1	IN-718 - secant α .	139
5.1.1.1-2	WASPALLOY - secant α .	140
5.1.1.2-1	Thermal expansion plots for Ti ₃ Al in the in-plane and thickness directions.	141
5.1.1.2-2	Secant CTE (with $T_{ref}=1010^\circ\text{C}$) for Ti ₃ Al in the in-plane and thickness directions and associated curve fits.	143
5.1.1.2-3	Tangent CTE for Ti ₃ Al in the in-plane and thickness directions and associated curve fits.	144

LIST OF TABLES

TABLE	TITLE	PAGE
1-1	Materials Characterized	2
4.1.2-1	Elastic Properties Used for Comparative Calculations	56
4.1.2-2	Stresses in the Fiber and the Matrix at Fiber/Matrix Interface for a 100°C Temperature Increase	56
4.1.3-1	Material and Geometrical Properties for the Hollow Cylinder used to Compute Stress Distribution Shown in Fig. 4.1.3-1	59
4.2.2-1	Material Properties for SCS-6/Ti-24-11	67
4.2.2.2-1	Approximate Axial Stress Results for the Fiber and the Matrix at the Fiber/Matrix Interface	69
4.4.1.1-1	Centerline Displacements and Stress Intensity Factors for M(T) Specimen with $L/W = 0.72$ and $2a/W = 0.2$	104
4.4.1.3-1	Constants for M(T) Compliance	107
4.5-1	Elastic Properties for the Fiber and Matrix and their Volume Fraction in the Composite	121
4.5-2	Axial Stresses in the Fiber and Matrix for Thermal Cool Down	121
5.1.1.2-1	Secant CTE and Tangent CTE for Ti-24Al-11Nb Foil in the In-Plane and Thickness Directions	142

Section 1

Introduction

This program emphasized the experimental determination of advanced mechanical properties that characterize the behavior of emerging materials for aerospace structures under a broad range of conditions representative of those encountered in service. The information, obtained under this program, guided the development of life prediction methodologies which are based on the concept of damage tolerance as a design philosophy. The experimental investigations addressed materials and environments typical of those encountered in service and concentrated on those areas where current life prediction schemes were weakest or totally lacking.

Limited information existed on the mechanical properties of new and emerging materials. In many cases no mechanical test techniques were available to provide designers with reliable and reproducible mechanical property data. Technology was created for designing test procedures and techniques that supported the data acquisition, damage accumulation, failure analysis and modeling of a new generation of materials which did not behave like conventional metallic materials. Such materials are candidates for advanced turbine engine and hypersonic vehicle applications. The various materials, listed in Table 1-1, have been evaluated in this program. The type of test characterization and the location in this report where additional information can be found are also presented in Table 1-1.

The research effort was subdivided into four interrelated research tasks:

- Material Characterization Tests
- Experimental Procedure and Test Developments
- Analytical and Modeling Developments
- Test Support Activities and Data Archival

These tasks formed an umbrella that covered many investigations which supported major advances in the development of models for life predictions of engine related component cracking problems. The following sections discuss work in progress and work completed on these tasks.

Table 1-1 - Materials Characterized			
Generic Name	Material Designation (fiber/matrix or monolithic)	Property	Section
Metal Matrix Composites	SiC/Ti-24Al-11Nb (at.%)	Fatigue	2.1.1
" " " "	" " " " " "	Creep	2.1.2
" " " "	" " " " " "	Fatigue Crack Growth	2.1.3
" " " "	" " " " " "	Residual Stress	2.1.4
" " " "	" " " " " "	Fractography	2.1.5
" " " "	" " " " " "	Fragmentation	5.1.4
" " " "	Si/Nb	Fracture Toughness	5.1.7
Ceramic Matrix Composites	SiC(Nicalon™)/ Aluminosilicate Glass	Fatigue	2.2.1
" " " "	" " " " " "	Tension and Creep	2.2.2
" " " "	" " " " " "	Fatigue Crack Growth	2.2.3
" " " "	" " " " " "	Fracture Toughness	2.2.4
" " " "	Nb/NbSi	R-Curve	5.1.3
Ti Monolithics	Ti-24Al-11Nb (at.%), plate	Creep	2.3.1
" " " "	" " " " " "	Creep Crack Growth	2.3.2.1
" " " "	" " " " " "	Fatigue Crack Growth	2.3.3.1
" " " "	" " " " " "	Oxidation	2.3.4
" " " "	" " " , fiberless foil	Thermal Expansion	5.1.1.2
" " " "	Ti-1100	Creep Crack Growth	2.3.2.2
" " " "	" " " " " "	Fatigue Crack Growth	5.1.8
" " " "	Ti-24Al-5Nb (at.%)	Oxidation	2.3.4
" " " "	Ti-25Al-10Nb-3V-1Mo (at.%)	Tension	5.1.2

Table 1-1 - Materials Characterized (Continued)			
Generic Name	Material Designation (fiber/matrix or monolithic)	Property	Section
" " " "	Ti-25Al-25Nb (at.%)	Tension	5.1.2
" " " "	Ti-15V-3Al-3Cr-3Sn (wt.%), casting	Fatigue	5.1.5
" " " "	Gamma Ti Aluminide	Fracture Toughness	5.1.7
" " " "	IMI-834	Fatigue Crack Growth	5.1.8
" " " "	Ti-6242	Fatigue Crack Growth	5.1.8
" " " "	Ti-6242S	Fatigue Crack Growth	5.1.8
Ni Super Alloys	IN 718	Fatigue Crack Growth	2.3.3.2
" " " "	" " " " " " "	Thermal Expansion	5.1.1.1
" " " "	Waspaloy	Thermal Expansion	5.1.1.1
Ceramic	Alumina (Coors™ AD 998)	Fatigue Crack Growth	2.3.3.3
" " " "	SCS-6, SiC Fibers	Tension	5.1.6
Al Alloy	2024-T351	Opening/Closure Loads	2.3.3.4

Section 2

Material Characterization Tests

The goal of doubling the thrust-to-weight ratio of current aircraft turbine engines and the continuing quest for high performance materials have lead to a search for lightweight structural materials able to withstand high temperatures. Many advanced materials are generally recognized as materials with low density and high service temperature capability; however, their structural use has been restricted due to limited understanding of their response to service type conditions. Recently, metal matrix and ceramic matrix composites reinforced with carbon or silicon carbide fibers have been developed which retain the high temperature capabilities of the original matrices but have increased toughness and durability due to the reinforcement materials. These composites and advanced monolithic materials are being rigorously investigated as candidate materials for structural applications requiring low density, high strength, and high-temperature capability.

2.1 Metal Matrix Composite (MMC): SCS-6/Ti-24Al-11Nb

MMC [Gambone] of special interest was developed and evaluated under a Government contract. The composite was a silicon fiber (SCS-6) reinforced titanium metal matrix composite (Ti-24Al-11Nb) fabricated by a foil-fiber-foil technique. Results of experiments designed to characterize the MMC behavior are described in the following five sections.

2.1.1 Fatigue

An experimental study was conducted on the high cycle fatigue behavior of SCS-6/Ti-24Al-11Nb at elevated temperature [Kortyna and Ashbaugh]. The effects of frequency, mean stress and stress range on fatigue life and damage evolution were investigated by conducting tests at several frequencies and stress ratios and using several techniques to detect damage.

The results indicated that the failure life of the composite was time dependent at each stress ratio studied. Loading frequency had no significant effect on time to failure. However,

failure lives varied with stress ratio due to competing mean stress and stress range effects on fatigue.

Physical observations were made from surface replications and fracture surface analyses. Electric potential difference, elastic modulus and residual strength were also used to evaluate the evolution of damage during testing. The results from these techniques proved to be very useful.

By correlating the physical observations and the damage monitoring results, a description of the damage evolution was proposed. Damage initiation was determined to be directly related to the molybdenum crossweave used in the fabrication of the composite. Damage evolution was attributed to both environmental degradation and mechanical loading. The mechanical loading resulted in two distinct types of failure modes, one corresponding to mean stress dominated fatigue and the other to stress range dominated fatigue.

A phenomenological model was presented which predicted failure life of the composite. This model was based on the observations of damage evolution at the various stress conditions. Additional data and information [Kortyna] are provided on matrix cracking of the composite, effect of matrix cracks on electric potential differences, fractography, and model verification.

2.1.2 Creep

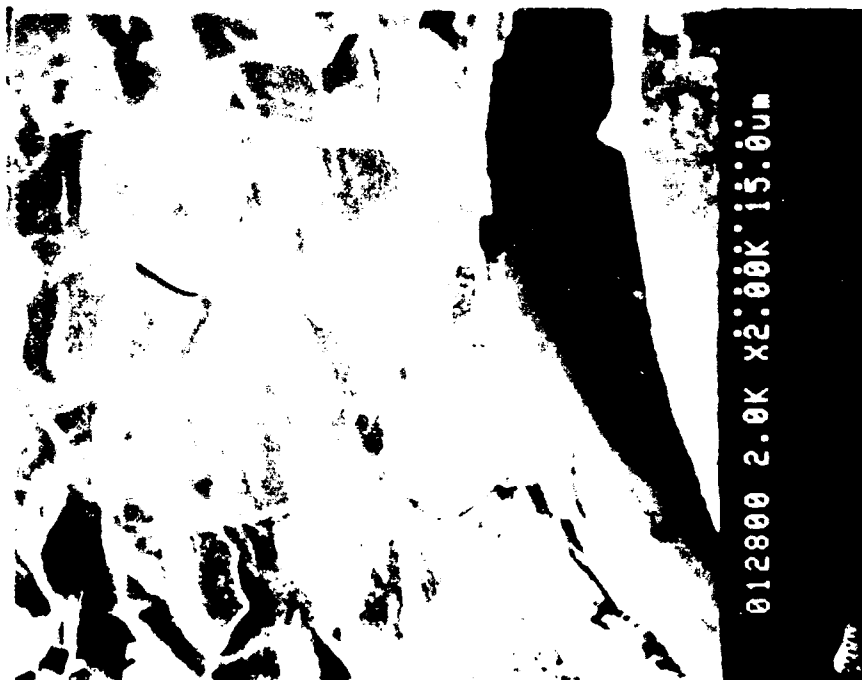
This investigation [Khobaib] studied the creep behavior of SCS-6/Ti-24Al-11Nb composite. The main objective of the study was to understand the damage evolution under sustained load at high temperature in this class of material. The detailed microstructural creep behavior correlation will provide important information for future metal matrix composite development.

Tensile creep tests were conducted over the temperature range of 650° to 815°C. Most of the tests were conducted on specimens fabricated from unidirectional panels. Limited tests were conducted with [0/90] layup. The specimens were loaded with the tensile axis parallel to fiber direction. The strain vs time plot produced a classical creep behavior with three distinct regions. The total creep strain to failure was found to be less than the strain for fiber failure. The role of environment was studied by conducting creep tests in vacuum under loading conditions similar to the tests conducted in laboratory air.

A series of tests were conducted at 650°C and 483 MPa, to study the damage evolution on continuous sustained load exposure. Tests were stopped in the primary region, corresponding to 0.08% and 0.1% creep strain, and in the secondary region with a creep strain of 0.13% and 0.14%. Another specimen was stopped at 0.175% creep strain representing the transition from secondary to tertiary stage. After the test, each specimen was thoroughly analyzed for damage (surface/edge crack, oxidation, etc.). In all cases, the matrix layers were selectively etched out to study the damage in the bulk fiber lay up. Evidence of fiber failure was observed as early as in the initial part of the secondary stage. Detailed optical and SEM analysis of the creep ruptured specimens were conducted to understand the failure mechanism.

Figure 2.1.2-1(a&b) shows negligible difference in the failure mode of the matrix during creep of SCS-6/Ti-24Al-11Nb at 650 and 760°C. Evidence of extensive amounts of grain boundary sliding at each temperature was apparent. The cracking in the outer carbon layer and reaction zone was also quite obvious. Similar observations were made for specimens creep ruptured at 815°C. Evidence of extensive grain boundary sliding and slip in the matrix shown in Fig. 2.1.2-2 occurred in a specimen tested at 815°C and 345 MPa. Apparently the matrix showed extensive creep and a complex mechanism of creep involving slip, microvoid coalescence, and grain boundary sliding was involved. Some evidence of diffusional creep was also noticed. Figure 2.1.2-3 shows remarkable evidence of slip traces present on a large number of grains within the matrix of an SCS-6/Ti-24Al-11Nb specimen tested at 760°C and 315 MPa in vacuum. Clear indication of grain boundary sliding was also found. Figure 2.1.2-4 shows evidence of the grain boundary sliding as well as microvoid coalescence activity. Figure 2.1.2-5 shows a higher magnification view of microvoids formed in the matrix. The slip activity in the matrix was also clearly noticed on specimens tested in air at 760°C and 315 MPa. Figure 2.1.2-6 shows intersecting slip traces formed in the matrix. Figure 2.1.2-7 is a higher magnification view of these slip traces.

The investigation of the creep deformed structure was further extended to TEM analysis to study the interaction of deformation between the matrix and fiber during creep of SCS-6/Ti-24Al-11Nb. Figure 2.1.2-8 is a TEM micrograph showing the continuity between the matrix and fiber (including the two outer carbon layers). Figure 2.1.2-9 is a similar TEM micrograph showing the initiation of debonding between the two outer carbon layers of SCS-6 fiber which occurred in a specimen tested to nearly 0.13% creep strain at 760° and 315 MPa in vacuum. Other evidence



(a)

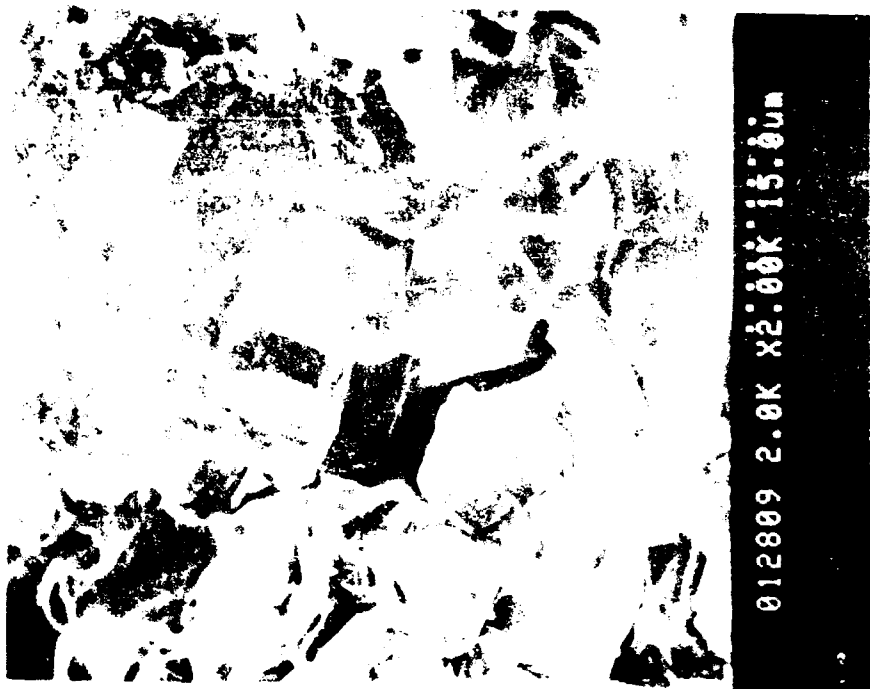


Fig. 2.1.2-1 Fractograph showing the deformation modes in the matrix during creep of SCS-6/Ti-6Al-4V at 650°C and b) at 760°C.



Fig. 2.12.2 Micrograph showing grain boundaries of grain boundary of SCS 6/Ti 24Al 10V composite at 815°C.

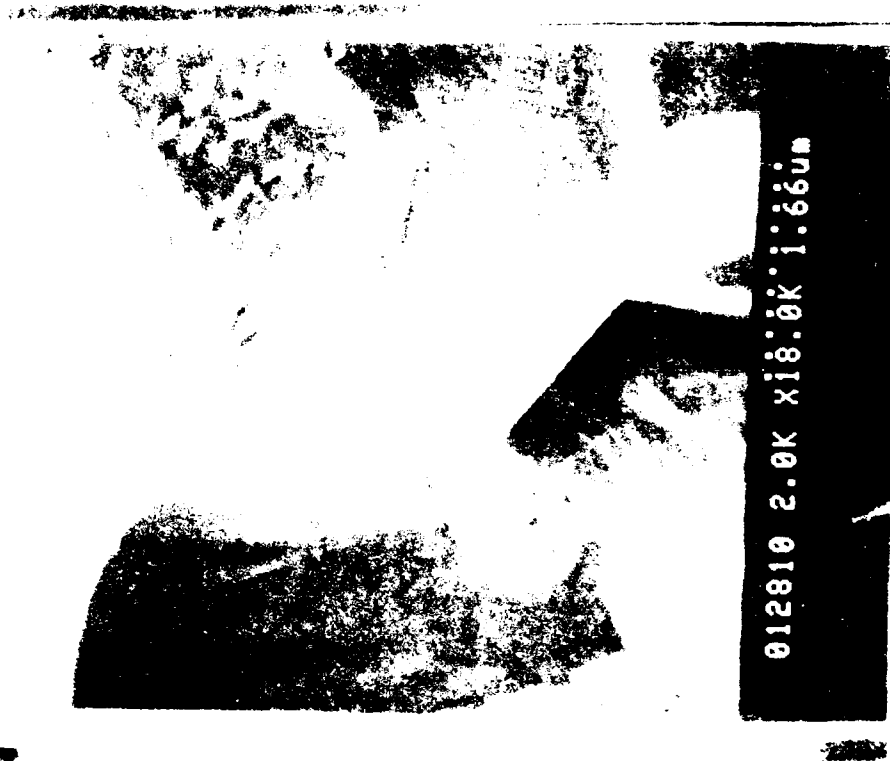


Fig. 2.12.3 Micrograph showing matrix of extensive slip in the matrix during creep of SCS 6/Ti 24Al 10V composite at 815°C.



Fig. 2.1.2-4 Fractograph showing evidence of grain boundary sliding and microvoid coalescence in the matrix during creep of SCS-6/Ti-24Al-11Nb at 815°C.



Fig. 2.1.2-5 Higher magnification view of the evidence of microvoid coalescence.



Fig. 2.1.2-6 Evidence of extensive slip activity in the matrix during creep of SCS-6/Ti-24Al-11Nb at 815°C.



Fig. 2.1.2-7 Higher magnification view of slip traces shown in Fig. 2.1.2-6.



Fig. 2.1.2-8 TEM micrograph showing absence of debonding.



Fig. 2.1.2-9 TEM micrograph showing initial stage of debonding between the carbon layers.

of initial debonding between the two outer carbon layers was found in SEM investigations. TEM observations indicated extensive dislocation activity in the matrix. Indirect evidence of the dislocation activity in the reaction zone was also noticed but documentation was difficult due to the presence of very small grains (nanometer level) in the reaction zone. However, evidence of the void formation in the reaction zone could be easily noted in Fig. 2.1.2-10. Figures 2.1.2-11 and -12 show the dislocation activity in the matrix very close to the reaction zone. Figure 2.1.2-11 shows long intersecting dislocations along with loops, while Fig. 2.1.2-12 shows the evidence of dislocation activity on nonbasal planes. The deformation apparently proceeded from matrix to fiber through some kind of dislocation activity. This activity could be clearly traced in the matrix all the way to the reaction zone. Also, indirect evidence of dislocation activity was noted in the reaction zone. However, the transformation of this deformation activity from reaction zone to outer carbon layer of SCS-6 was not clear due to the amorphous nature of carbon.

2.1.3 Fatigue Crack Growth Behavior

Generally, unidirectional-reinforced metal matrix composites can tolerate a large amount of damage in the longitudinal direction of the fibers [Larsen et al.; Mackay et al.]. However, they are susceptible to minor damage across or transverse to the fibers. For a better understanding of the limits of the transverse behavior of the composite and to provide insight for the evaluation of damage accumulation in life prediction models, the fatigue crack growth behavior parallel to the fibers was investigated under simulated service conditions [John and Ashbaugh, 1990 & 1991a].

Cyclic fatigue crack growth tests were conducted using unidirectional SCS-6/Ti-24Al-11Nb specimens which contained a crack oriented parallel to the fibers. All tests were performed in laboratory air at room temperature and 650°C. Crack growth rate data were obtained using both compact tension, C(T), and centrally notched disk, DM(C), specimens (see Section 4.4.3). In the test using the DM(C) geometry, the crack mouth opening displacement (CMOD) was measured using a laser interferometric displacement gage (IDG) system (see Section 3.2). Extensometers were used to measure CMOD in the C(T) specimens. In these tests, near crack tip displacements were also measured using the laser IDG to evaluate the closure phenomenon.

The results of this investigation were compared with those obtained using SE(T) specimens [Gambone]. Fatigue crack growth parallel to fibers at room temperature and 650°C showed a dependance on geometry. The possible causes included plate-to-plate variability,



Fig. 2.1.2-10 TEM micrograph showing evidence of void formation in reaction zone.



Fig. 2.1.2-11 Evidence of dislocation loops and long intersecting dislocation.

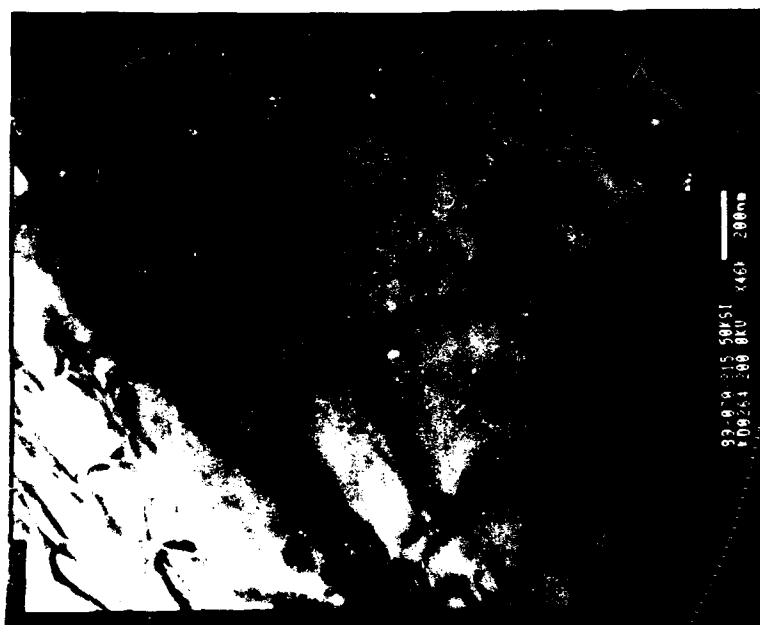


Fig. 2.1.2-12 Evidence of dislocation activity on nonbasal planes.

combined effects of orthotropy and geometry, and closure behavior. Due to limited material availability, additional tests on different geometries obtained from the same plate could not be conducted to check the feasibility of using the stress intensity factor as a crack driving parameter. Closure loads of about 40% of the maximum load were observed even at an applied cyclic stress intensity ratio of 0.5 at the crack tip. Such high closure loads can be attributed to the extensive surface roughness created by fibers on one fracture surface and its corresponding trough on the other fracture surface. Test frequency significantly affected the crack growth rate at 650°C. The frequency effect could be attributed to the environmental degradation of the matrix and/or the interface. Long term exposure to laboratory air for three to four days significantly reduced the crack growth resistance. To further characterize the environmental degradation, tests at elevated temperature in vacuum are required.

2.1.4 Residual Stress Measurement

Residual stress analyses [Jayaraman and Rangaswamy] were completed using the $\sin^2\Psi$ X-ray diffraction technique on an as-processed unidirectional fiber reinforced titanium aluminide metal matrix composite. Residual stresses were measured in the Ti-24Al-11Nb matrix α_2 phase in orientations parallel, transverse and 45° to the fibers. Stress profiles were determined by removing layers of the metal surface by electro-polishing. In general, at distances away from the fiber plane, plane stress conditions prevailed and the actual stresses appeared to be independent of depth from the surface layer. However, close to the fiber plane (10 to 30 microns from the fiber plane) steep stress gradients normal to the surface were indicated. A plane stress analysis showed a tensile stress state at layers far from the fiber plane and a compressive stress state very close to the fiber plane.

2.1.5 Fractographic Characterization

A detailed study [Jata et al.] of fracture modes was conducted on SCS-6/Ti-24Al-11Nb composite specimens. Fracture surfaces of specimens tested under tensile, creep, isothermal fatigue, thermomechanical fatigue and fatigue crack growth were examined using optical and scanning electron microscopy. Fracture surface studies showed that Mo crossweave wire, used to keep the fibers in place during HIP consolidation plays a major role by enhancing crack initiation sites and the formation of steps on the fracture surface in some test conditions. Fiber pull-out and steps in the fracture surface appeared to be prevalent fracture modes in high temperature tensile and in-phase thermomechanical fatigue tests. In low temperature tensile and

out-of-phase thermomechanical fatigue tests, flat fracture, less fiber pull-out and fewer steps on the fracture surface were common fracture modes. Steps in the fracture surface clearly appeared to be initiated at the Mo crossweave wire in thermomechanical fatigue. Optical microscopy studies of the material below the fracture plane showed microcracking of the matrix in out-of-phase thermomechanical fatigue tests and microcracking of the fibers in in-phase tests. Fibers were relatively free of such microcracks in out-of-phase tests. These results correlated well with the high stresses that are developed in the fibers during in-phase tests and high stresses in the matrix during out-of-phase tests, as predicted using elastic-plastic finite difference analysis.

Creep specimens exposed to high temperatures and sustained loads exhibited either intergranular or transgranular matrix fracture modes, step formation and degraded fibers. In isothermal fatigue, cracks initiated from faces, edges and corners of the specimen and propagated inwards. Fatigue crack growth specimens with fibers perpendicular to the main crack ($[0]_g$) showed evidence of fiber pullout, cyclic plasticity, environmental induced cracking and degradation of fibers. In this orientation, Mo wire exerted far less influence on the plane in which fatigue cracks grow as compared to thermomechanical fatigue at high strain ranges. Fatigue crack growth rates as a function of temperature in specimens oriented with fibers parallel to the fatigue crack, ($[90]_g$), could be related to cleavage and furrow-type failure modes that occurred in the matrix and to crack propagation along fiber-matrix interfaces.

2.2 Ceramic Matrix Composite (CMC): SiC/1723

Since CMCs were not readily available for characterization under anticipated service conditions, a composite was fabricated in-house to serve as a model CMC. A silicon carbide fiber (Nicalon™) and an aluminosilicate glass (1723 from Corning) were the components for the CMC. Characterization of SiC/1723 is described in the following four sections.

2.2.1 Fatigue

Two fundamental roadblocks to widespread use of CMC materials are the lack of understanding of the composite fatigue and thermomechanical fatigue behaviors and the technical difficulty in performing critical thermal and mechanical material behavior experiments. The UDRI has been involved in a project at the MLLN laboratories that is designed to study the tensile and fatigue behavior of three CMC materials at room and elevated temperature [Butkus et al.]. To

date, a number of room and elevated temperature tensile and fatigue tests have been performed. These tests have revealed that:

- 1) for the unidirectional SiC/1723 composite tested, room temperature fatigue life was controlled by the presence or absence of inelastic strains. Specimens tested at maximum stress levels above the proportional limit continually accumulated damage and failed in less than 10^6 cycles.
- 2) the elevated temperature fatigue life for stresses below the proportional limit showed some environmental degradation starting at temperatures of 500°C. No changes in the measured mechanical properties (modulus) were evident until the temperature was increased to 800°C.
- 3) Additional testing to longer cyclic lives should be performed to ascertain if the damage accumulation mechanism operating at stresses between the matrix micro-cracking level and the proportional limit saturates at about 10^5 cycles or if continued damage accumulation will cause specimen failure at longer lives.

2.2.2 Tensile and Creep Behavior

Tensile tests of SiC/1723 were conducted at room temperature, and the creep tests were conducted at 600, 700, and 750°C. Room temperature tensile test failure features exhibited a tortuous crack path and extensive fiber pull out. The failure features of SiC/1723 in creep were characterized by flat fracture and little fiber pull out [Khobaib and Zawada]. The environment appeared to play a significant role in creep failure of this composite system.

2.2.3 Fatigue Crack Growth Behavior

An investigation [John and Ashbaugh, 1991b] of fatigue crack growth in (90/0)_{3s} SiC/1723 composite was conducted at room and elevated temperatures using the C(T) geometry. All the tests were conducted in laboratory air. The stress intensity factor and compliance solutions from isotropic analysis were used to analyze the orthotropic CMC behavior. The isotropic solutions were expected to provide reasonable values of stress intensity factors and compliances because results from available analyses in the literature indicated that small variations in the values occurred when the ratio of transverse modulus to longitudinal modulus was of the order of unity.

In the room temperature tests, the damage on the surface of the specimen was distributed around the notch tip thus making it difficult to define a conventional crack length

(shown later in Fig. 2.2.4-1). Hence, in this study, the compliance crack length was used to evaluate the evolution of damage during fatigue in the composite. The unloading compliance was computed from the linear range of the load-CMOD data obtained periodically during the tests. For an applied K_{max} less than 90% of the peak fracture toughness, the composite had a high resistance to crack growth determined from compliance measurements. Additional compliance crack growth occurred only upon an increase in the applied K_{max} . Similar observations were also made on SiC reinforced lithium aluminosilicate glass composite [Luh et al.]. SEM photographs showed that even at high levels of applied K_{max} the cracks were fully bridged by fibers thus decreasing the effective stress intensity factor at the crack tip. Constant compliance crack growth rate occurred when the applied K_{max} was within 90% of the peak fracture toughness. This high damage tolerance at room temperature could be attributed to energy dissipation through distributed matrix cracking near the tip, fiber bridging, and fiber pullout. To verify the applicability of compliance to characterize fatigue damage/crack growth, additional tests on different geometries are required.

In contrast, the damage tolerance of SiC/1723 composites was decreased significantly at 650°C. The crack growth occurred in a self-similar manner with negligible macrocracking and no fiber pullout. The lack of fiber pullout indicated an improved interface bond between fiber and matrix at temperatures close to the apparent maximum use temperature of the matrix. This apparent increase in bond strength might be attributed to the formation of SiO_2 at the fiber-matrix interface [Bischoff et al.]. Additional tests in vacuum will be conducted to verify this phenomenon.

2.2.4 Fracture Toughness

The fracture behavior of $(90/0)_{3s}/SiC/1723$ was evaluated [Coker and Ashbaugh] using C(T) specimens having W of 20 mm and 40 mm. The specimens were monotonically loaded until fracture occurred and load-crack opening displacements plots were obtained. The influence of notch preparation (abrasive water-jet or diamond saw cut) and fatigue precracking was investigated.

A distinct difference existed between the fracture behavior of precracked and notch extended specimens in terms of fracture surfaces and load-displacement behavior. The stress intensity factor corresponding to the maximum load, K_{peak} , was found to yield consistent values for the precracked specimens. However, K_{peak} was found to be higher for precracked specimens than for notched specimens. This difference in K_{peak} was attributed to fiber bridging of the crack

in the precracked specimens. No difference in material behavior was observed between specimens with abrasive water-jet and diamond saw notch extensions. No size effects on K_{peak} was noticed for precracked specimens, in contrast to apparent size effects for the notched specimens.

To characterize the damage evolution of the $[90/0]_{3s}$ SiC/1723 composite, interrupted load-CMOD tests were conducted at room temperature using C(T) specimens [John and Ashbaugh, 1991a]. The specimen was held at a pre-decided load or CMOD value and then a fluorescent dye penetrant was applied on both sides of the specimen. The specimen was then removed from the machine and photographs taken under ultra-violet light. Two photographs highlighting damage on the specimen as indicated by the dye penetrant corresponding to 19% and 100% of the peak load are shown in Fig. 2.2.4-1. At very low loads, multiple cracks, i.e., distributed damage, occurred around the saw-cut notch tip; thus, the effective stress intensity was reduced at the notch tip. At the peak load, extensive damage was observed along the notch plane accompanied by large number of cracks on either side of this plane. Even at the peak load, the specimen was still intact and the region of extensive damage occurred only in about 50-75% of the original uncracked ligament of the specimen. SEM photographs of the crack surface showed clear evidence of fiber bridging the primary crack.

2.3 Monolithic Materials

2.3.1 Creep Behavior of Ti-24Al-11Nb

Titanium aluminide (Ti-24Al-11Nb) is a potential candidate for aircraft gas turbine engine application due to its high specific strength at elevated temperature. Any such application for an extended period of time will require knowledge of the creep behavior of this material. The objective of this study [Khobaib et al., 1989] was to investigate the creep behavior of Ti-24Al-11Nb which was supplied in 12.7mm thick plate form. Figure 2.3.1-1 shows the smooth round bar tensile specimens used for this study. Creep tests were conducted in the temperature range of 550-800°C, and stress range of 140 MPa to 280 MPa. The higher temperature and stress resulted in increased creep rate and shorter rupture life.

For all tests conducted in laboratory air, an abnormal amount of surface cracking over the gage length of the specimen was observed. The density of such cracking reduced with decreasing temperature and hardly any surface cracking was observed on specimens tested at



(19% peak load)



(peak Load)

Fig. 2.2.4-1 Damage characterization using fluorescent dye penetrants in CMCs.

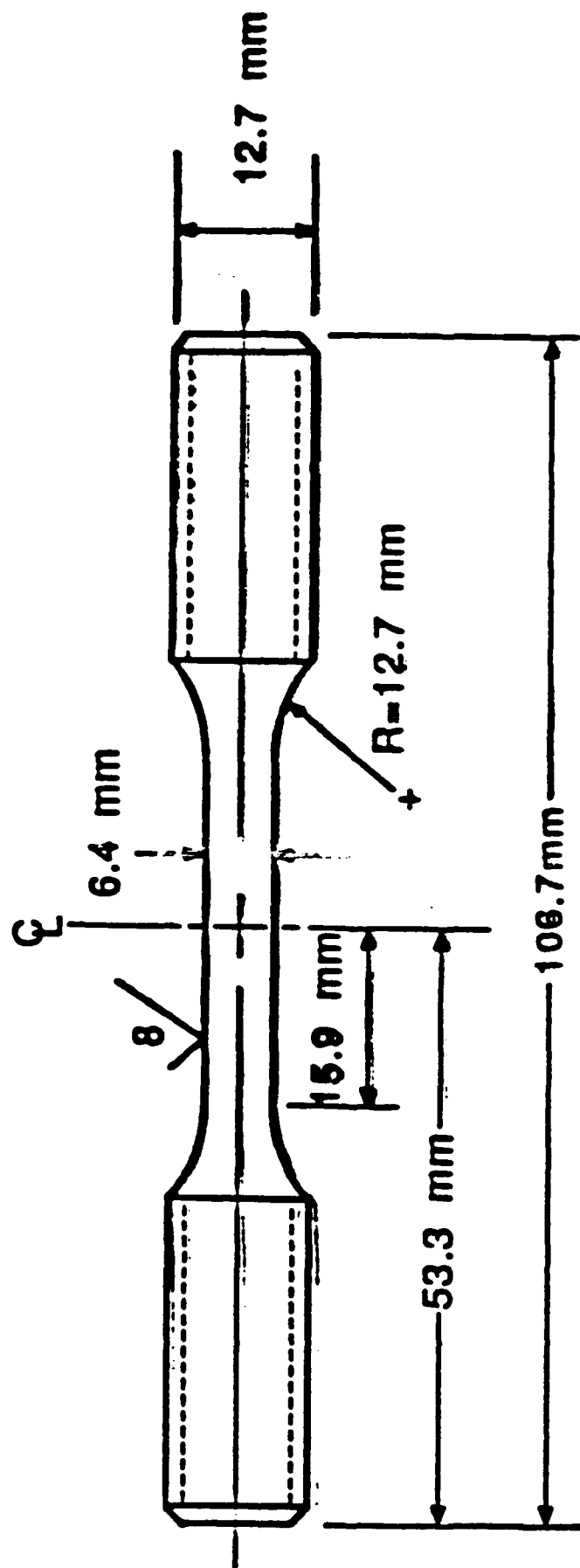


Fig. 2.3.1-1 Round bar tensile creep specimen.

550°C. Specimen surface and environment played a dominant role controlling surface cracking behavior. A substantial reduction in surface cracking also resulted by removing approximately 1 mm depth of surface material by electro-polishing. Again no visible surface crack was observed on specimens tested in vacuum. Surface cracking was apparently related to the formation of brittle surface oxide layer and the oxidation of the surface was accentuated by surface residual stresses.

The role of environment on the creep behavior of Ti-24Al-11Nb was investigated by conducting creep tests in both laboratory air and a vacuum of nearly 10^{-6} torr. Tests were conducted in the two environments under similar conditions of temperature and load. At all test temperatures (650, 700, 750 and 800°C), the steady state creep strain rate was found to be higher in vacuum as compared to laboratory air.

Fracture analysis of specimens creep tested in laboratory air revealed a transgranular mode of failure. Detailed analysis showed the failure mode to be a mixture of cleavage and ductile tearing. In contrast, the specimen failed in intergranular manner in vacuum, which apparently resulted from the separation of prior beta grain boundaries. Although the failure was intergranular, detailed SEM analysis revealed a ductile mode of failure. Extensive subcracking within the grain was also observed which occurred preferentially along the α/β interface [Ashbaugh et al.].

TEM analysis of the creep ruptured specimens showed intense dislocation activity. Figure 2.3.1-2 shows the dislocation structure in a specimen creep tested at 650°C in air. The dislocation density was quite high and apparently several slip systems were active. By using basal (0002) reflection, the activity of slip in the nonbasal plane was also revealed. Figure 2.3.1-3 shows a set of parallel dislocations in the nonbasal plane, indicating that nonbasal slip was also contributing to the deformation.

2.3.2 Creep Crack Growth

Creep crack growth (CCG) studies of titanium base alloys were conducted to understand the mechanism of time dependent crack growth process in this class of materials. Ti-24Al-11Nb was selected as the representative titanium aluminide material while Ti-1100 was chosen as a conventional high temperature titanium alloy.

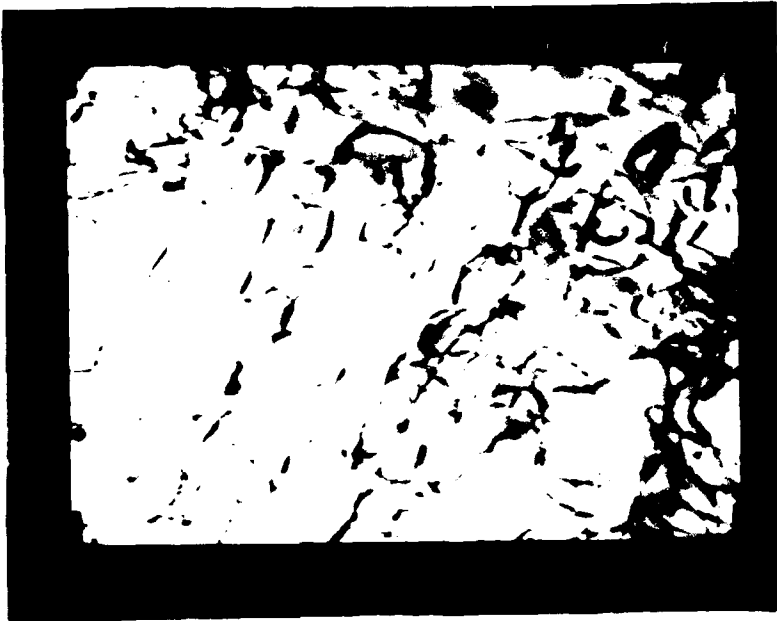


Fig. 2.3.1-2 Dislocation structure generated during creep of Ti-24Al-11Nb at 650°C.



Fig. 2.3.1-3 Evidence of nonbasal slip activity during creep of Ti-24Al-11Nb at 650°C.

2.3.2.1 Ti-24Al-11Nb

The CCG behavior of β -heattreated Ti-24Al-11Nb was studied over the temperature range of 650-800°C. Sustained load tests were conducted both in laboratory air and in a vacuum environment of 10^{-6} torr. The laboratory air tests were conducted with standard metric compact tension specimens, ($W=40.6\text{mm}$) while subcompact specimens ($W=20.3\text{mm}$) were used for tests in vacuum. However, some selected tests in laboratory air were conducted with subcompact specimens to provide comparative data for the two environments. All the specimens used in this investigation were side grooved to enhance a plane strain condition along the intended crack plane.

The results [Ashbaugh et al.] showed a negligible effect of environment on CCG behavior of Ti-24Al-11Nb. At all temperatures, either the CCG rates obtained from vacuum tests were slightly higher or similar to the CCG rates obtained from laboratory air tests. The results are dissimilar to behavior observed with most metallic materials where the environment (laboratory air) is known to accelerate the CCG.

Detailed analyses of fracture surfaces were conducted to understand the mechanism of crack growth process in this material. The failure mode for specimens tested in laboratory air appeared to be transgranular at all temperatures except at 800°C, where the fracture appears to be intergranular. In general (from 650-750°C), the failure appeared to be cleavage type and crystallographic. However, at high magnification, there was good evidence of ductility. In contrast to the fracture surface features obtained in laboratory air, the failure mode of specimens tested in vacuum at 650-800°C appeared intergranular.

2.3.2.2 Ti-1100

Standard metric compact tension specimens were prepared from 12.7mm thick forged plate. The specimens were precracked to nearly 9.40mm (0.370 in). Tests were conducted at temperatures of 590, 650 and 700°C. A range of initial K values ($16\text{ MPa}\sqrt{\text{m}}$ to $35\text{ MPa}\sqrt{\text{m}}$) were used at each temperature to obtain crack growth rate. In each case the crack blunted after negligible growth. Step increases in K values resulted in extensive blunting.

2.3.3 Fatigue Crack Growth

2.3.3.1 Ti-24Al-11Nb

The fatigue crack growth behavior of an alpha-2 titanium aluminide, Ti-24Al-11Nb, was studied [Balsone et al.] as a function of temperature (25 to 800°C), frequency (0.001 to 1.0 Hz), superimposed hold times (1,10,100, 1000 s), and environment (air and vacuum) under computer controlled constant K_{max} testing conditions. Results indicated that the fatigue crack growth rate exhibited time dependent behavior and was sensitive to environment over the entire temperature range studied. Growth rates were found to depend on frequency at elevated temperature in both laboratory air and vacuum but growth rates in air were as much as an order of magnitude higher than those obtained in vacuum. Further, hold times at maximum load were found to increase the cyclic crack growth rates due to a contribution of environmentally assisted crack growth. Fractographic analyses revealed no change in fracture mode as a function of frequency.

The fatigue crack growth behavior of an orthorhombic + beta titanium aluminide, Ti-25Al-25Nb, was studied [Balsone and Maxwell] as a function of temperature (25 to 750°C), environment (air and vacuum), frequency (0.001 to 1.0 Hz), and superimposed hold times (1,10,100,1000 s) under computer controlled constant K_{max} testing conditions. In addition, fatigue crack growth rates from the near threshold region to approximately 10^{-6} m/cycle were determined at room and elevated temperatures. Results indicated that the fatigue crack growth rate exhibited a combination of cyclic- and time-dependent behavior and was sensitive to environment over the entire temperature range. At elevated temperature, crack growth per cycle was found to increase with decreasing frequency in both laboratory air and vacuum, suggesting a contribution due to environmentally assisted crack growth even at 10^{-6} torr vacuum. Growth rates in air were as much as an order of magnitude higher than those obtained in vacuum. Further, hold times were found to slightly increase the cyclic crack growth rates at elevated temperatures due to a contribution of sustained load crack growth. At elevated temperatures, crack growth behavior appeared to be a complex interaction of environmental degradation at the crack tip, crack tip blunting due to creep, and cyclic fatigue (resharpening of the crack tip). The crack growth characteristics were compared with those of the alpha-2 titanium aluminide, Ti-24Al-11Nb, and a conventional high temperature titanium alloy, Ti-1100.

2.3.3.2 IN 718

The following two investigations on fatigue crack growth at load ratios, R , near unity and at near-threshold conditions were conducted. For load ratios near unity, fatigue crack growth rates were determined in Inconel 718 middle cracked tension [M(T)] specimens at 649°C under conditions of high frequency (10 to 100 Hz) [Nicholas and Ashbaugh]. Under these conditions, the material experienced cycle-dependent crack growth as well as time-dependent crack growth. At R values approaching unity, the observed growth rates were lower than those obtained under sustained load at the same mean load in the absence of the superimposed cyclic loading. Tests on compact tension [C(T)] specimens at lower frequencies were used to demonstrate the existence of three regions of behavior--cycle-dependent, mixed mode, and time-dependent.

A linear cumulative damage model was used to predict the growth rates due to combined cycle-dependent and time-dependent mechanisms. The model was developed from 427°C data for the cyclic term and sustained load crack growth data at higher temperatures for the time-dependent term. Although the model could not predict the synergistic effect for R near unity, it provides a reasonable representation of much of the data. The authors concluded that the use of low-temperature data for the cyclic term was inadequate for representing the threshold values and growth rates at low ΔK values at the higher temperature.

For near-threshold crack growth behavior, an experimental program [Ashbaugh and Nicholas] was conducted to evaluate the effects of frequency and load ratio of Inconel 718 at 649°C in laboratory air. Frequencies from 0.01 to 400 Hz and R from 0.1 to 0.9 were applied to C(T) and M(T) specimens under decreasing- K conditions using computer-controlled test systems. Digital load-displacement data were obtained to determine crack length and closure load. The fatigue crack growth threshold in Inconel 718 at 649°C obtained using decreasing ΔK testing was generally associated with a crack arrest phenomenon which could be attributed to the buildup of oxides with time. Over the ranges of R and frequency used in this investigation, the growth rate behavior at the onset of crack arrest appeared to be a combination of time-dependent and cyclic-dependent behavior. Even at 400 Hz, purely cyclic behavior was apparently never reached. For crack growth rate modeling, both frequency and stress ratio had to be incorporated in the characterization of ΔK_{th} . Over the ranges of parameters tested, a cyclic threshold was approached at high frequencies and low R and a sustained load time-dependent threshold was obtained for R near unity, indicating that the cyclic contribution to the growth rate was negligible.

2.3.3.3 Alumina

For a better understanding of the reinforcing effect of the fibers during fatigue crack growth in the CMCs, it was essential to determine the cyclic crack growth behavior in the plain brittle matrix. For this purpose, a new fatigue crack growth testing system was developed using a disk with a middle crack subjected to compressive loading, DM(C), shown in Fig. 2.3.3.3-1. The DM(C) geometry was previously used for mixed mode fracture toughness tests on brittle materials such as sintered carbide [Yarema et al.], PMMA [Atkinson et al.], graphite and marble [Awaji and Sato], and alumina [Shetty et al.], and was suggested for studying cyclic crack growth in concrete [Wang and Petroski]. Other geometries that were used to study fatigue crack propagation in plain ceramics include compact tension [Dauskardt and Ritchie], double cantilever beam [Reece et al.] and four-point bend [Beals and Bar-On]. The advantages of the DM(C) geometry were discussed elsewhere [Ashbaugh et al.; John and Ashbaugh, 1991b]. The LEFM expressions for K and CMOD for the DM(C) geometry were developed during this investigation as discussed in Section 4.4.3. To conduct automated tests, a noncontact displacement measuring method was developed by adapting the laser IDG system, described in Section 3.2.4.2.

An alumina (Coors[™] AD 998) ceramic disk specimen was tested at a frequency of 5 Hz at room temperature in laboratory air with a stress intensity ratio of 0.10 ($=K_{min}/K_{max}$) [John and Ashbaugh, 1991b]. Load versus crack mouth opening displacement response for the ceramic specimen were obtained periodically during the test. From the load-CMOD data, material behavior such as compliance and closure loads were obtained during the cyclic crack propagation. Total displacements on the order of 1.5-2.0 μm were measured accurately. The following summarizes the conclusions based on this fatigue crack growth study: (1) fatigue crack growth in alumina was both trans- and inter-granular, (2) closure loads were about 25% of the maximum load, (3) crack closure can be attributed to wedging of crack surface asperities, (3) transmission electron microscopy of replicates of unloaded specimen did not reveal crack bridging on the surface of the specimen, and (5) high magnification views of replicates taken near the crack tip indicated features similar to microcracking, which could provide the mechanism for fatigue crack growth in alumina ceramic.

2.3.3.4 2024-T351 Al Crack Opening/Closure Study

An investigation was conducted to compare two techniques for the determination of fatigue crack closure/opening loads. One technique involved load-displacement or load-strain

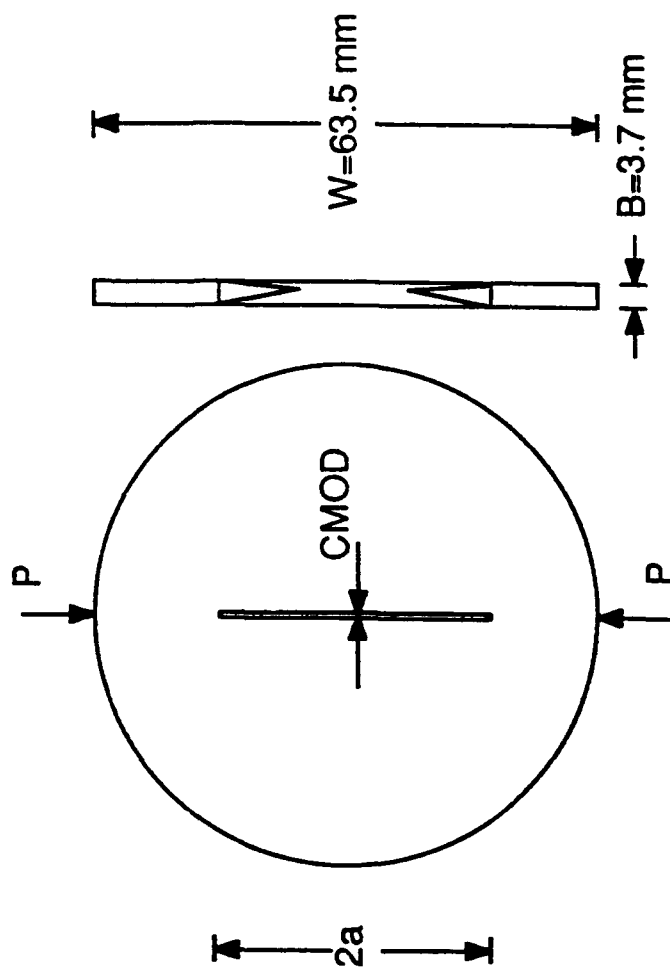


Fig. 2.3.3.3-1 Schematic of the DM(C) geometry.

data acquired during a specimen loading cycle. The displacements were determined across the crack both at the center and near the crack tip. The strains were measured with strain gages located at the intersections of the crack plane and the edges of the specimen. The second technique involved the evaluation of striation formations on the crack surfaces.

Fatigue crack growth tests were conducted on an M(T) specimen, 318mm (12 1/2 inches) long, 76 mm (3 inches) wide, and 9.5 mm (3/8 inch) thick, of 2024-T351 aluminum alloy. Crack growth was produced under block loading conditions where a constant stress-intensity amplitude with $R = 0.1$ was nominally maintained within a block. Each constant K loading block was applied to produce approximately 2 mm of crack growth. Single and multiple periodic overload cycles were also applied within certain blocks.

Specially designed programmed loading was used to introduce minor variations in the load cycles to create striation spacings on the fracture surface so that the cycle count and an opening load for crack growth could be identified. Two stress intensity ranges of 9.9 and 14.8 $\text{MPa}\sqrt{\text{m}}$ were chosen to obtain striation formation on the fracture surface. An interferometric displacement gage (IDG) was used to obtain the displacements across both the middle of the crack and near the crack tip region. The applications of back face strain (BFS) gages and of IDG for determination of closure loads have been described in a previous investigation [Ashbaugh]. The striation technique has also been reported [Sunder and Dask].

Some preliminary closure results from striation spacings and from load-strain data are presented in Fig. 2.3.3.4-1 as a function of crack length; additional closure results from striation spacing have been discussed [Sunder]. Even though the closure loads indicated by striation markings and by load-strain responses have shown consistency for a given technique, the results from one technique compared to the other have been different. The determination of closure loads has been further complicated by the results from IDG measurements shown in Fig. 2.3.3.4-2. The displacement data for these closure loads were obtained at locations approximately 75 microns behind the crack tip. Since a large amount of scatter occurred in the IDG closure load data, the mean value of closure load and the range of plus and minus one standard deviation have been shown. Generally, the mean values of the IDG closure loads were higher than the striation results, which were higher than the BFS results. Perhaps, the large scatter in near tip IDG closure loads was created by slight variations in the contact between crack

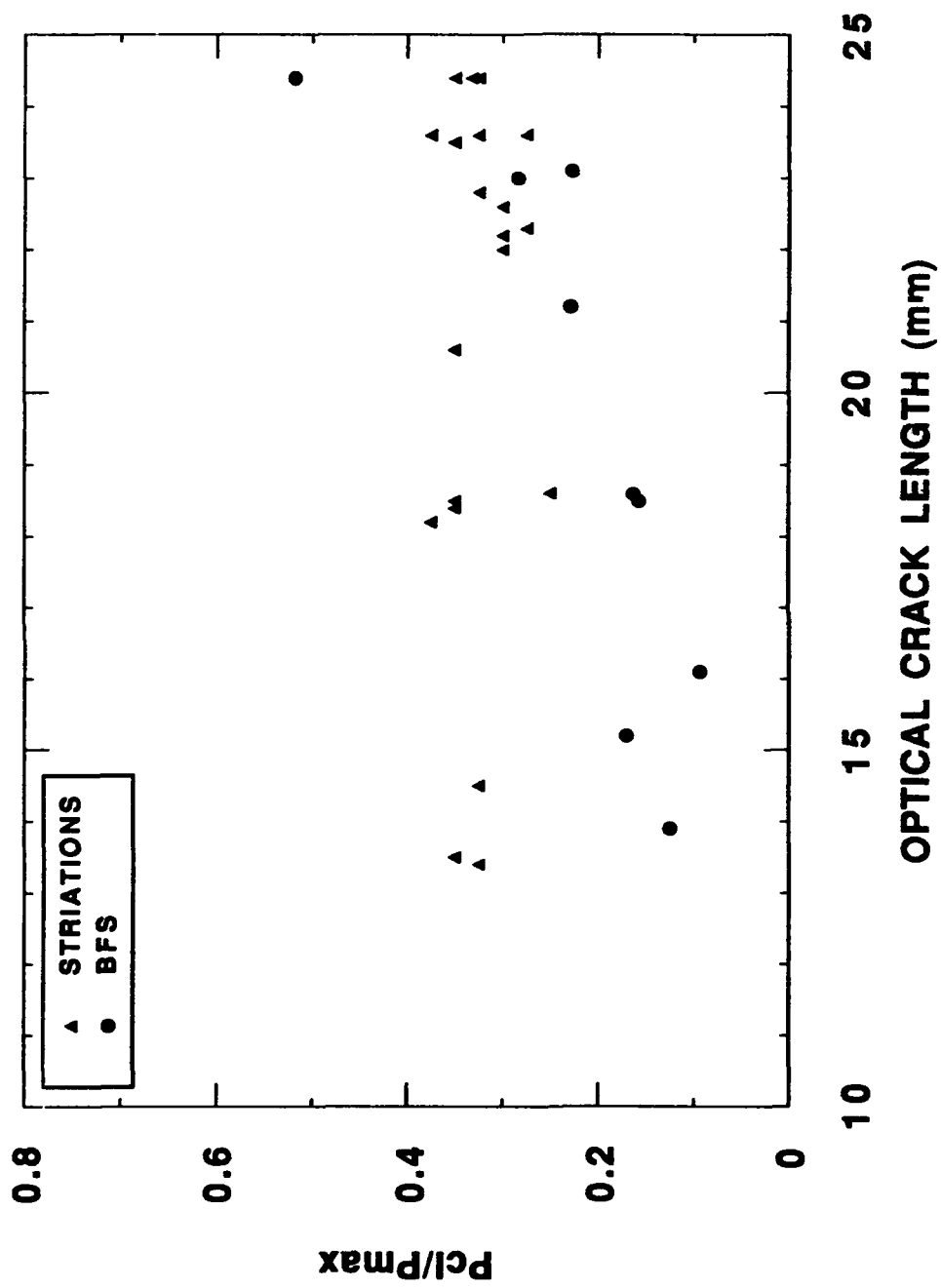


FIG. 2.3.3.4-1: Comparison of Closure Loads Obtained From BFS and Fracture Surface Striation Spacings.

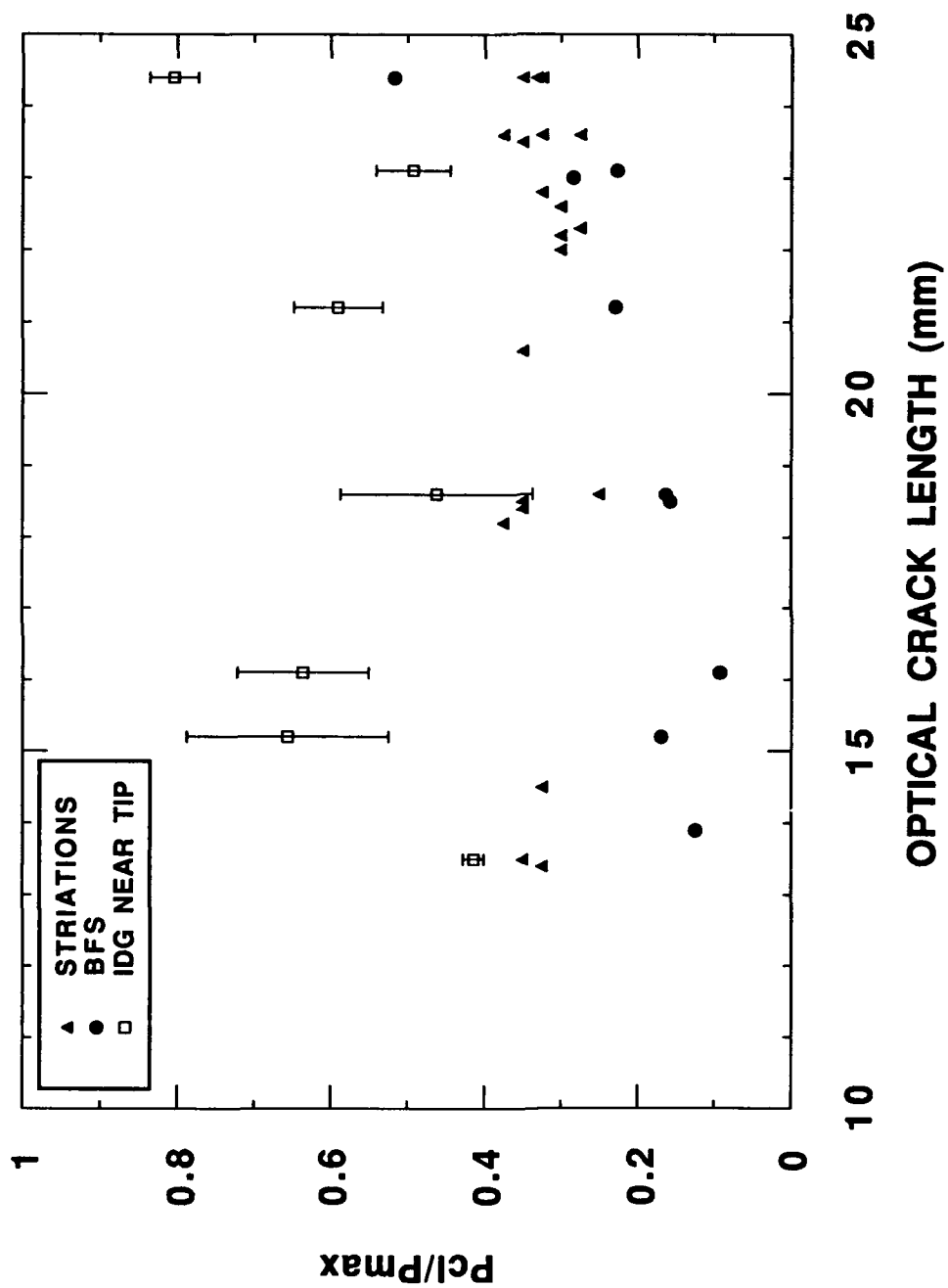


FIG. 2.3.3.4-2: Comparison of Closure Loads Obtained From IDG, BFS and Fracture Surface Striation Spacings.

surfaces near the tip from one loading cycle to another. The IDG technique used in this investigation could resolve displacement changes as small as 20 nanometers.

The trend of the IDG closure loads being higher than the striation closure loads was consistent with observations from striation results [Sunder] that indicated higher closure load values for striations nearer the sides of the specimen than in the middle of the fracture surface. The low values of the BFS closure load could be attributed to the fact that the strains being a far-field response of the deformation represented an average specimen strain. Thus, the local conditions at the crack tip could be masked by the global deformation of the specimen. Also, the BFS technique might not be sensitive enough to exhibit the initial surface contact behind the crack tip. The evaluation of the techniques and the interpretation of the data have yet to be resolved completely.

2.3.4 Oxidation Behavior of Ti₃Al Alloys

High temperature oxidation behavior of two Ti₃Al alloys has been studied at 700 mm Hg oxygen pressure in the temperature range of 700-850°C. Weight changes were obtained from tests conducted at specified time intervals up to 100 hours. Results were compared with data obtained on a commercial high temperature titanium alloy, IMI834. The weight gain results showed improved oxidation resistance of Ti₃Al alloys as compared with IMI834. The higher concentration of Nb also had a significant effect in increasing the oxidation resistance. SEM analysis of the oxidized surfaces was conducted to understand the mechanism of oxidation on these alloys [Khobaib and Vahldiek].

Section 3

Experimental Procedure and Test Developments

A major portion of the total research effort involved developing new material test methodologies and equipment to meet the basic research mission of the MLLN laboratories. The recent interest in the behavior of MMC and CMC materials in complex service environments presented new challenges for researchers studying the mechanical behavior of these materials. The significant accomplishments of the UDRI in developing both appropriate test with emphasis on thermomechanical fatigue (TMF) capability equipment and techniques are described in the following subsections.

3.1 Test System Developments

3.1.1 Thermal Cycling System

The difference in the thermal coefficients of the matrix and fiber materials in continuously reinforced MMC and CMC materials produces internal stresses as the temperature of the composite is changed. Studying the behavior under imposed thermal and/or mechanical cycles and in aggressive or inert environments is necessary to understand the complex interactions of the various service conditions that these materials are expected to experience. Three thermal cycling systems have been designed and developed to apply thermal cycles simulating service loading under both inert and aggressive environments.

Each system consisted of a horizontal tube furnace, a forced air cooling system, a long stroke pneumatic cylinder, and a multiloop control system. A specimen was attached to the end of the air cylinder rod which could be (a) extended to place the specimen in the tube furnace or (b) retracted to place the specimen in the forced air cooling area outside the furnace. For inert environment testing, the specimen was encapsulated in a glass tube that had been either evacuated or filled with an inert gas. The control system monitored both the furnace and specimen temperature and could be programmed to produce a wide variety of thermal cycles

including hold times. These thermal cycling systems have been used successfully to study the effects of environment and thermal cycling on SCS-6/Ti-24Al-11Nb MMC materials [Revelos and Smith].

3.1.2 TMF Upgrade of Schenck System

As part of a significant MLLN laboratory enhancement program, the UDRI has rebuilt two Schenck resonant fatigue test systems for use as low frequency (less than 0.1 Hz) TMF systems. To accomplish this task, the UDRI performed the following steps:

- 1) removed all mechanical and electronic controls from the machines,
- 2) repaired load frame components as necessary,
- 3) refitted machines with pneumatic cylinders for load application,
- 4) refitted machines with precision aligned rigid grip systems for composite materials,
- 5) designed, constructed, and installed electronic closed loop load controllers,
- 6) installed computer hardware and software to perform TMF tests, and
- 7) checked out and demonstrated the use of the machines for laboratory researchers.

These machines performed isothermal or TMF fatigue or creep tests at temperatures from ambient to 1500°C and have been used to support several test programs [Russ and Nicholas].

3.1.3 High Frequency Systems

3.1.3.1 C-20 System Developments

The following enhancements have been implemented on the C-20 high frequency test system. Load train alignment capability of the C-20 frame has been greatly improved by the development of a sensitive three-axis alignment device which was installed between the cross head and load cell. The UDRI design provided translational as well as angular adjustment of the upper load train. When alignment mode was activated, the moving components floated on air cushions which resulted in very low friction to adjustment motion. With low friction, the load train was easily moved into alignment by a simple fixture. The alignment was then locked-in by activation of a clamping cylinder. Using a cylinder for clamping reduced the shift often introduced when tightening bolts.

The heating apparatus consisted of three quartz lamps. Two were oriented horizontally on one side of the specimen, the third was oriented vertically on the other side of the specimen.

The two were controlled by separate control loops with the respective thermocouples located at the upper and lower extremes of the gage zone. The vertical lamp was operated at a fixed power level. To avoid fixing the thermocouples to the specimen surface, the control thermocouples were welded to a dummy specimen located adjacent to the test specimen. The dummy-to-actual specimen temperature correlation was established by a periodic temperature uniformity survey.

Because of short specimen lengths typically used in the C-20, extra effort was required to achieve an acceptable temperature uniformity for elevated temperature testing. Specimen-to-grip gradient was minimized two ways. A thermal barrier was established between the specimen and the grip by bonding sheet mica tabs to the grips. These tabs also provided electrical insulation for EP purposes. Secondly, the grips were maintained at a slightly elevated temperature by using air cooling rather than water. The air flow was adjusted for grip temperatures of about 150°C which would cause erratic flow of water coolant. With only 70 mm of specimen length exposed between the grips and operating at 815°C, a gradient of less than 10°C was achieved over a distance of 30mm.

When two new power amplifiers were acquired (for the C-20 and another system), there was concern that these "switching" amplifiers might generate high frequency electrical interference. Investigators have demonstrated that the level of radiation experienced in operation has been small and has posed no serious problems with other laboratory instrumentation.

3.1.3.2 Unholtz-Dickie Test System

The Unholtz-Dickie test system design was based on an Unholtz-Dickie model M506 shaker. This is an air cooled shaker with a maximum force rating for 45kN (10,000 lb) peak-to-peak. Although this is 2.8 times the force rating of the C-20 system, it has an armature weight twice that of the C-20. The net performance gain over the C-20 system would therefore be maximum at lower frequencies and diminished at higher frequencies where inertial effects dominate. A massive cross-head (over 18kN) would contribute to the actual specimen loading capability at high frequencies.

The mean load range of the new Unholtz-Dickie test system was 70 to -70kN. Operation at mean loads above 44kN required air pressure higher than normally supplied. Thus, an air pressure booster has been installed in the utility core adjacent to the Shaker system. This

booster was capable of supplying the maximum working pressure (150 psig) of both the C-20 and Unholtz-Dickie systems.

The air chamber on the new system has been designed for full compressive loading. This capability has been at the expense of added complexity of design and load control and with a small penalty in high frequency loading. Dual air chambers (one for the tension side of the piston and one for the compression side) required extra piston hardware to accommodate two rolling diaphragms. Also required are two voltage-to-pressure transducer units with the associated control software.

The cross-head has been assembled on four 102mm (4.0 inches) diameter columns and the hydraulic systems for clamping, raising and lowering have been tested.

3.1.4 TMF Vacuum System

The expected service environments for CMC and MMC materials included elevated temperatures, thermal cycling, mechanical loadings, and aggressive environments. An initial understanding of the behavior of these materials in service could be obtained by performing experiments that vary one or two of the service conditions while maintaining the other(s) constant. The results of these simplified tests could be used to develop models that predict the behavior of materials under the complete service environment. Ultimately, simulation of the complete service environments on laboratory coupon specimens or performance of full scale tests to validate the predictive models must be completed. Obviously, performance of tests on laboratory specimens, if possible, to minimize the cost and time required was desirable.

The UDRI has designed and is in the final stages of installing of a mechanical test system capable of performing mechanical tests on MMC and CMC materials under conditions that closely simulate the expected service environment. The specifications considered for the system were:

- 1) applying mechanical loads to frequencies of 50 Hz,
- 2) providing vacuum, inert, or ambient (oxidizing) environments for tests,
- 3) maintaining isothermal specimen temperatures from -200°C to 1500°C,
- 4) applying thermal cycles to the specimen anywhere in the range from -200°C to 1500°C, and

- 5) monitoring applied load, axial displacement in the specimen gage section, multiple temperatures on the specimen surfaces, and DC electric potential difference across the specimen.

The availability of this type of system has greatly expanded the range of tests that could be performed and has allowed researchers to design test programs that more completely identify potentially damaging service environments and the material's response in such environments.

3.1.5 TMF Horizontal Test Systems

Additional demands for TMF and isothermal test capability in the MLLN laboratories have led to the installation of three additional test systems similar to the two existing MMC/CMC test stations [Butkus et al.]. These systems have a specially designed grip system that provides excellent alignment to minimize bending stresses in the test specimen. These systems also have, a multi-zone heating system that maintains uniform spatial temperature fields over the complete cycle for TMF tests. These three new systems were specifically intended to support the NASP Institute for the Mechanics and Life Prediction of High Temperature Composites (NIC) by providing capability to conduct tension, fatigue, creep, and TMF tests on advanced CMC and MMC materials being considered for hypersonic vehicles.

3.1.6 LCF Test System

A servo-hydraulic test system has been assembled for conducting low-cycle-fatigue (LCF) strain controlled tests at temperatures up to 650°C. The system utilized a standard 50 kN MTS 880 servo-hydraulic test frame. Several types of self-aligning grips were evaluated. Total bending within a strain gaged test specimen was reduced below 5% of the operating strain amplitude with MTS Model 647 hydraulically actuated grips, in conjunction with an MTS alignment fixture. During tests, an MTS Model 632.51B-04 water-cooled, 12.7mm (1/2 inch) gage length extensometer measured axial displacements. A 64mm (2-1/2 inches) high, 3 zone, quartz lamp furnace maintained a uniform temperature within the specimen gage length.

A computer control program was developed for total strain control LCF testing. The program, written in BASIC, was executed in compiled version to provide adequate speed for control of the test, to monitor various test parameters and to allow the operator a real-time interface. In addition to prompting the operator for appropriate control, preliminary cycling was

allowed to checkout the test setup. Load-strain hysteresis data were acquired and saved at operator selected or preselected cycles or times throughout the test.

3.2 Technique Development

3.2.1 Automation Software Upgrades

The UDRI has been in the forefront of test automation for the past decade and, as part of this automation activity, has provided advanced automation software to the MLLN laboratories. This software consisted of an integrated suite of programs designed to perform a wide variety of automated material tests and to analyze the resulting data [Hartman and Ashbaugh, 1990]. Currently, hardware and software for the automation systems have been designed and installed on virtually all of the test stations in the MLLN laboratory (totalling 24 systems).

3.2.2 Load-Pin-Size Effects for C(T) Specimen

Part of the mission of the MLLN laboratory and the UDRI under this contract was to investigate anomalous data that was collected as a result of the mechanical tests that were performed. In collecting data from C(T) geometry specimens using the existing ASTM standard E647-88, significant nonlinearity was noted in the load vs. displacement characteristics, even in the absence of a crack (specimens with machined notches only). A number of potential causes for this phenomenon were studied including crack closure, friction in the loading apparatus, and misalignment of the load train. None of these could explain the anomalous behavior.

A kinematic analysis of the loading clevises, loading pins, and loading holes in the specimen revealed that the close fitting pins, as recommended in the standard, created a significant translation of the point of application of the loads on the specimen during a loading cycle [Hartman and Ashbaugh, 1991]. The analysis also showed that this translation could be minimized by using somewhat smaller loading pins. Experimental verification of the results of the analysis was obtained by performing loading cycles with various size pins. As a result of this work, the ASTM standard was changed to recommend the use of either smaller loading pins, "D" shaped loading holes in the clevis, or bearings in the loading holes.

3.2.3 Laser Interferometric Displacement Gage (LIDG) Upgrade

The LIDG system design [Khobaib et al., 1988] was upgraded from a prototype system design to a fully developed laboratory tool. The upgrade covered three areas: electronics,

fixturing hardware, and software with primary consideration given to the user interface, ease of maintenance, and trouble shooting. Subsequently, three new laser IDG systems were constructed.

As part of the upgrade of the system electronics, the power supplies (5V and +/- 15V), gain and filter circuits, and output signal connectors were mounted on a customized rack-mount panel. A lighted on/off switch was added to the panel. The EG&G mother boards were mounted in an aluminum housing with cable harnesses connecting the boards to 25-pin D-type connectors. The satellite boards, also housed in aluminum enclosures, were each fitted with a cable harness and 25-pin D-type connector. Electrical connection between the power supplies and the mother boards was made through a single, off the shelf, commercial-grade, 25-conductor serial cable with D-type connectors. The same type cable was also used to link the satellite receiver boards with the mother boards. Thus, only three cables were needed to hook up the upgraded system; allowing easy system setup, trouble shooting, and repairs. Separating the power supplies and the gain/filter circuits from the mother boards made the system modular which also helps the maintenance process.

Before the LIDG system upgrade had begun, several conversations were held with users of the prototype systems to get their recommendations for improvements. One of the main suggestions was to improve the capability for positioning the optics. The optics were mounted on a baseplate that attached to the test frame via an extension arm with an elbow-type joint. Vertical adjustment of the system required loosening the test frame clamp at the end of the arm, shifting the entire baseplate/arm assembly up or down, and then tightening the clamp. The baseplate with optics was heavy (20-25 kg) so the adjustment was difficult for one person. Similarly, the receiver housings were adjusted by loosening a set screw, sliding the housings up or down along a slot, and then tightening the screw. Although the receiver housings were not heavy, the adjustment was a cumbersome process usually requiring several attempts for alignment of each receiver. To improve the setup process, slides were added for adjusting the vertical location of the baseplate and each of the receivers. A shop-grade, low-profile slide was inserted between the baseplate and the extension arm. Raising or lowering the baseplate was now possible simply by turning a handle on the slide. Similarly, slides were placed between the receiver housings and the baseplate so that the vertical adjustment of the receivers was done by

turning a handle. These improvements significantly reduced the setup time required for each test, made the setup a one-person process, and overall, improved the user-friendliness of the system.

The software [Khobaib et al., 1988] was upgraded to increase the data acquisition speed. Lower level data acquisition routines were coded in assembly language providing a significant increase in speed. Setup routines, such as "FRTRACK," were rewritten to upgrade the information presented to the user and to improve the update rate.

3.2.4 Application of LIDG System at Elevated Temperature

Development and verification of life prediction models for advanced high-temperature materials such as CMCs and MMCs required the mathematical modeling of the closure phenomenon near the crack tip. This closure behavior could be attributed to mechanisms such as grain bridging, fiber bridging and plastic deformation. Modeling of these closure mechanisms required experimental validation through accurate measurements of the crack opening displacement (COD) at various locations along the crack length under simulated service environmental conditions. An available technique for this purpose is the in-situ measurement of COD on SCS-6/Ti-15V-3Cr specimens loaded in a specially designed stage which was mounted inside a SEM [Kantzos et al.]. This method required the use of relatively small specimens. In addition, automated study of crack growth behavior in high stiffness brittle matrices used in the CMCs needed non-contact high-resolution displacement measurement techniques at elevated temperatures. A suitable technique for this purpose was the laser IDG (Interferometric Displacement Gage) system, which was developed for precise measurement of small displacements in metals [Sharpe; Hartman and Nicholas]. This technique was used for fracture toughness testing of ceramics at elevated temperatures [Jenkins et al.].

The LIDG system has been used at the Materials Directorate for the evaluation of fatigue closure loads using near crack tip displacements [Ashbaugh, 1988] and near-threshold crack growth behavior of surface flaws [Sharpe et al.]. These studies were conducted on metals at room temperature. During the present study, the laser IDG system was adapted to measure near crack tip displacements in metals at 650°C using a special coating and crack mouth opening displacements in a brittle material using metallic tabs glued to the specimen, as described in the following sections.

3.2.4.1 Displacement Measurement in Metals and MMCs

The optical paths of the LIDG system, shown as a schematic in Fig.3.2.4.1-1, developed interference patterns from reflections from pyramidal indents located on a polished surface of the specimen. For application at elevated temperatures, the reflectivity of the indent facets should be maintained. A survey of available specialized coatings which have been developed to prevent or minimize oxidation of surfaces indicated that these coatings would be unable to prevent the deterioration of the reflectivity of the indented surface. During this investigation, many other coatings such as gold, platinum, chromium and even a gold/rhodium mixture were applied on Ti-24Al-11Nb specimens. Tests at elevated temperatures revealed that these coatings either peeled off or lost their reflectivity. These problems were thought to be caused by oxidation of the substrate or from diffusion through the thin coating, and/or residual stresses arising from thermal mismatch between the coating and the specimen material. A fused quartz coating of 0.25 μm thickness proved to be partially successful as described next.

A Ti-24Al-11Nb compact tension specimen was coated with fused quartz, in a zone of about 6.4 mm on either side of the probable crack path along the entire width prior to testing. Indentation on the fused quartz surface yielded usable indents at room temperature even though small cracks were observed on the coating at the four corners of the indents. The specimen was then heated to 650°C and the indents were still usable. Fatigue crack growth tests were then successfully conducted on this specimen until the crack propagated a certain distance. The test was then stopped, the specimen cooled and new indents made near the crack tip. Then the specimen was reheated and the fatigue crack growth test restarted at 650°C. During the crack growth tests, load versus laser IDG displacement data were acquired periodically. This procedure was repeated by placing a new set of indents at regular intervals of crack growth increment. Every time a new set of indents were made on the specimen, both the specimen and the coating were subjected to thermal cycling. This cycling resulted in slow deterioration of the reflectivity of the facets of the previous indents possibly due to oxidation of the indent facets aided by the cracks in the fused quartz.

The above method of using the fused quartz coating was considered to be partially successful because the coating enabled displacement measurements at elevated temperatures. However, the effectiveness of the coating deteriorated with thermal cycling and long term

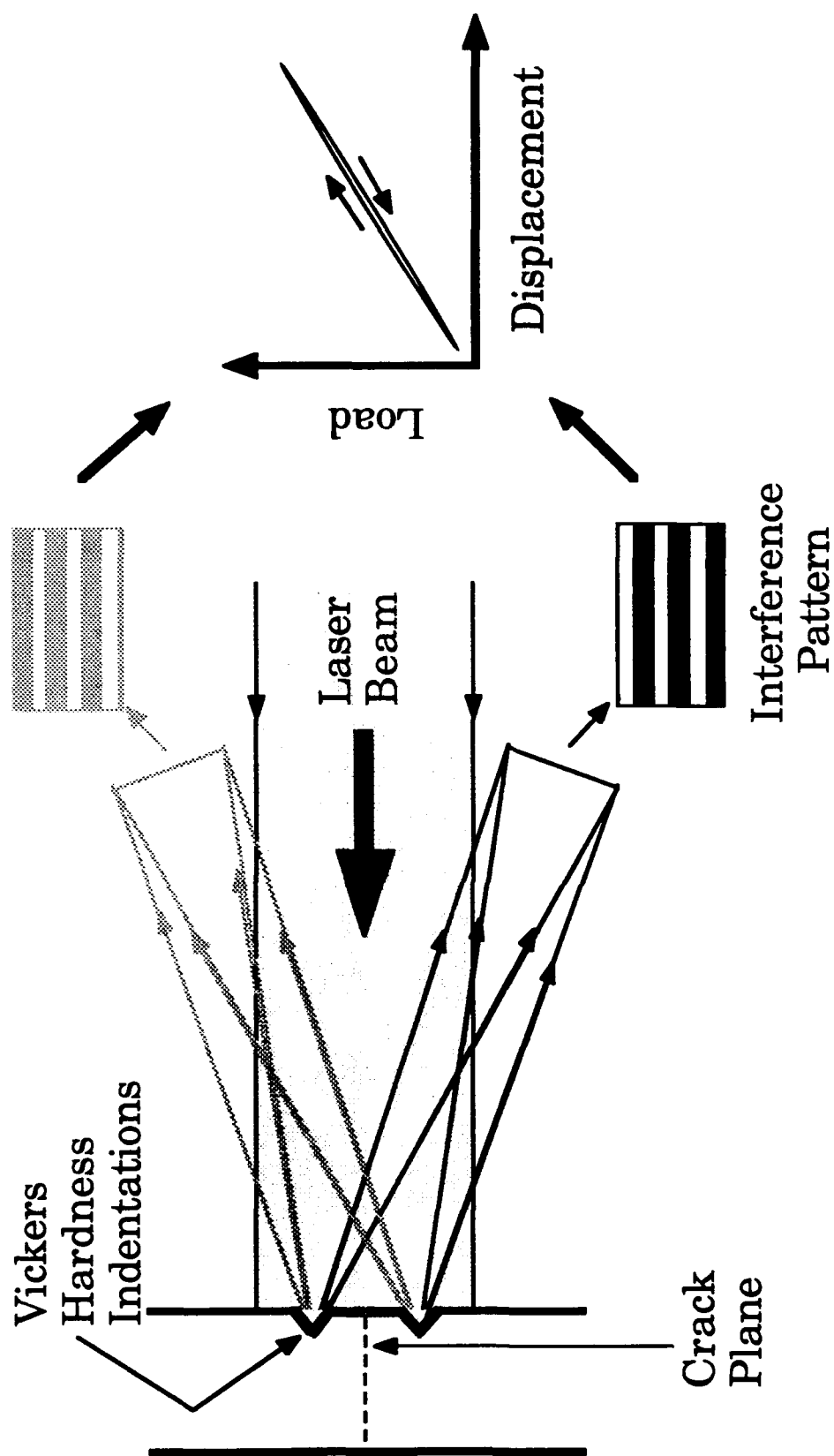


Fig. 3.2.4.1-1 Schematic of optical paths in laser interferometric displacement gage.

exposure to laboratory air at 650°C. A more durable coating would be required for obtaining near crack tip displacements in metals and MMCs subjected to long term crack growth tests.

3.2.4.2 Displacement Measurement in a Brittle Matrix and CMCs

During the investigation, the laser IDG technique was adapted to the measurement of crack mouth opening displacements in ceramic materials and CMCs. Since direct indentation of brittle materials would initiate local fracture, metallic tabs bonded on the surface were used for the indentation sites. At elevated temperatures, non-oxidizing tabs must be used [Jenkins et al.]; but for the development of the technique, steel tabs were used. The tabs were glued across the notch on the specimen using a high temperature ceramic adhesive and the indents placed on these tabs [Ashbaugh et al.], as shown in Fig.3.2.4.2-1.

This technique was successfully used to conduct a fatigue crack growth test in a plain alumina ceramic specimen. During the crack growth tests, total crack opening displacements of about 1.7 μm was measured accurately. The results of this test were discussed earlier in Section 2.3.3.3. Application of this technique to crack growth tests at elevated temperatures required further validation experiments using platinum tabs. The advantages of this technique included: (i) displacement measurements on composites and nonmetallic materials at elevated temperatures, (ii) displacement measurements across wide notches in geometries such as DM(C), C(T), M(T), SE(T) and SE(B), even in metals, and (iii) strain measurements in tensile specimens with tabs glued across the gage length. One possible disadvantage of the technique would be the averaging of displacements across the glued area. Hence, the bond area of the tabs should be as small as possible.

3.2.5 Ultrasonic Detection of Short Cracks

This investigation of the initiation and growth of a crack under fatigue loading was performed to determine if the presence of an initiated crack could be detected and the crack growth could be monitored using off-the-shelf manufactured ultrasonic transducers. After predetermined blocks of fatigue cycles, the crack was photographed and the associated ultrasonic reflection pattern was stored. The lengths of the crack in the photographs were digitized and associated with the corresponding processed peak to peak waveform in the ultrasonic reflection pattern.

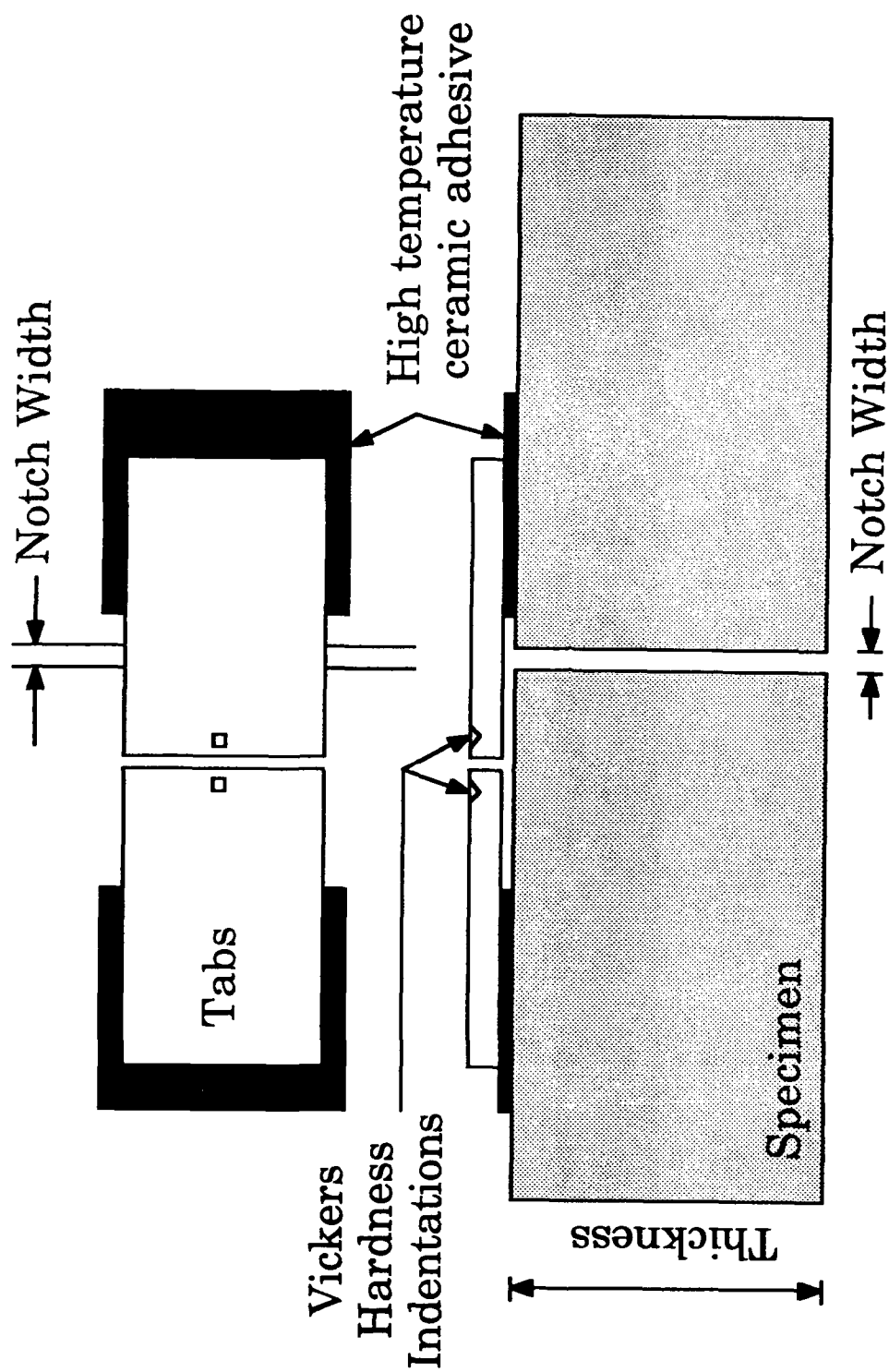


Fig. 3.2.4.2-1 Schematic of the tabs glued across the notch on a specimen.

This experiment utilized a square shanked aluminum-lithium T841 alloy with an electro-polished hourglass gauge section. The effective gauge area was $8.940 \times 10^{-5} \text{ m}^2$ and rectangular in shape. The crack initiation and growth test was performed under constant P_{\max} with $P_{\min}/P_{\max} = -1.0$. The maximum load of 22 kN was chosen to produce a maximum stress which was 45% of the 551.2 MPa yield strength. Previous data from small crack work with Al-Li T841 indicated that crack initiation occurred at this load level within 5 kcycles. So blocks of 250 cycles for the inspection intervals were chosen. After each block of cycles the reflected signal from the transducer was averaged 16 times and then stored on 5-1/2 inch floppy disk. Once an indication that a crack appeared, the test was temporarily stopped and a photograph was taken to record the crack.

Conformation of the crack was easily accomplished by touching the crack with a methanol soaked cotton swab and watching the reflected waveform on the oscilloscope. When the methanol fills the crack, the reflected amplitude indication on the scope disappears. So while simultaneously watching the crack through the camera and the reflected waveform on the scope, one can be assured that the crack producing the ultrasonic signal is the one within the camera viewfinder. The ultrasonic indication of a crack appeared on the reflected waveform around Sample No. 62 and the preceding procedure was used to identify the crack. A total of 28 reflected waveforms were taken and stored along with photographs to correspond for each.

The unprocessed waveforms indicated a crack reflection at Sample No. 62 which had a surface crack length of 151 μm . The crack was successfully tracked up to a length of 397 μm .

Although the test seemed very successful, a computer hardware problem created anomalies in the stored reflected waveforms; this problem was discovered after testing was completed when split spectrum processing of the waveforms was implemented. The processed waveform would give a peak to peak amplitude of the reflected signal which would correspond to a digitized crack length. It would also tell when the crack had initiated somewhere previous to Sample No. 62 by stripping the noise level off and leaving only a special reflection from the minute crack. However, a random off-set which occurred when the computer stored the waveform produced a very large scatter in the processed amplitudes as shown in the log plot of processed amplitude versus cycle count, Fig. 3.2.5-1

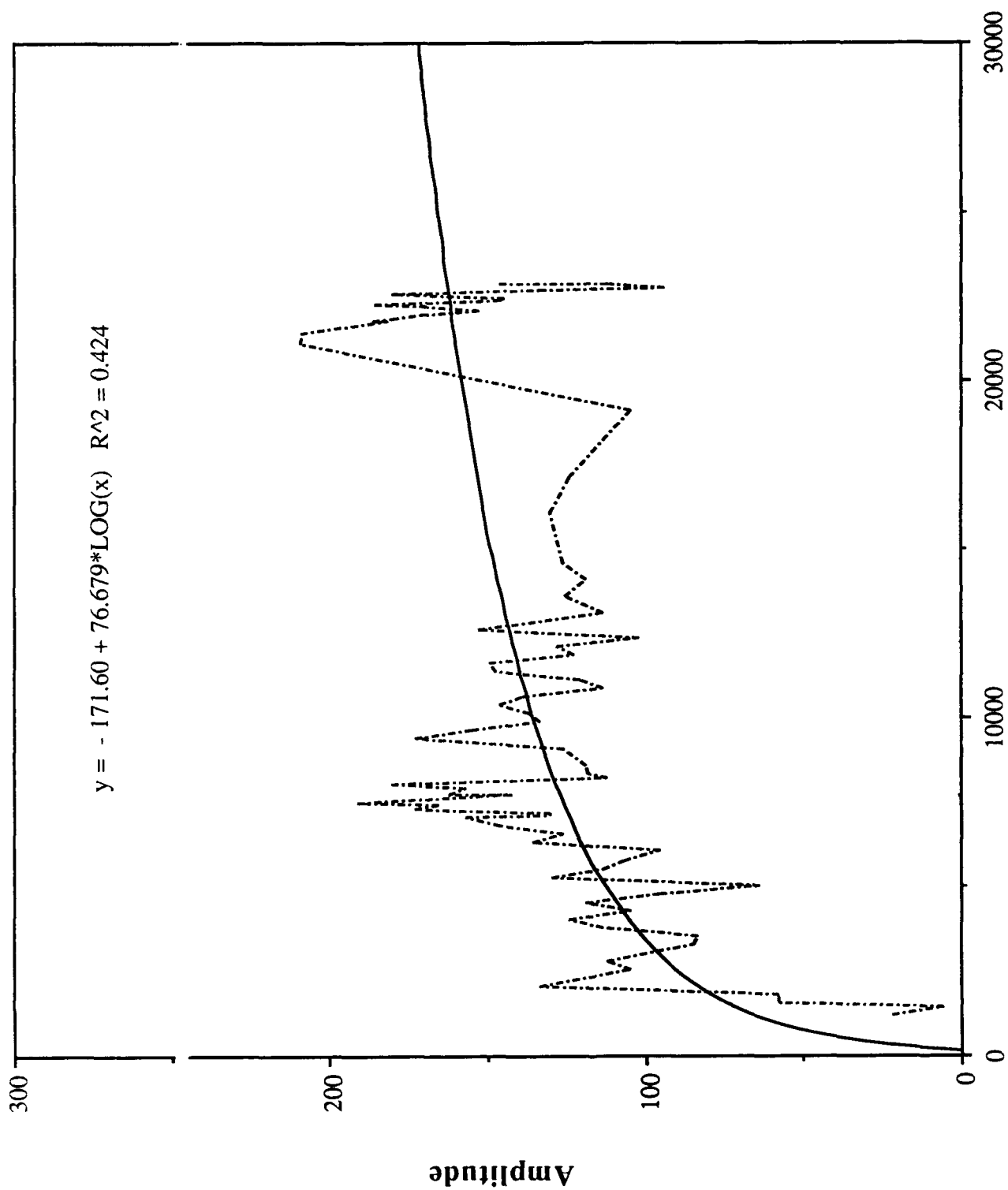


Fig. 3.2.5-1 Processed amplitude of reflected signal from a short crack.

3.2.6 DCEPD Measurement of Short Cracks

To accommodate crack initiation studies, an extra sensitive DCEPD (DC electric potential difference) system was developed for the Instron high frequency test system. Utilizing this DCEPD system, cracks smaller than 20 microns have been resolved in Ti-24Al-11Nb [Parida and Nicholas]. The power supply and digital voltmeter (DVM) were the same models used for the standard DCEPD systems throughout this laboratory. The higher sensitivity required for crack initiation resolution was obtained by making EP measurements at three locations -- two locations near the specimen notch and at one reference point location. The reference point measurements were utilized to cancel variations in conductivity of the specimen. Thermal EMF was canceled by duplicate measurements with the current direction reversed. The relay unit (Fig. 3.2.6-1) enabled software control of the current reversal and the measurement of all three points using one DVM. It consisted of three relays interfaced to the computer I/O port. To control the I/O ports, an assembly language routine was written which may be called from within the main program (MATE version 253A).

Two approaches for utilizing the reference point measurements have been used by other researchers -- the ratio and the algebraic correction techniques. Being initially uncertain of which technique was most effective, the crack length algorithm was written to calculate results from both techniques so the two methods could be compared. Thus, four crack lengths were calculated from each data acquisition -- two each for the left and right sides of the notch. A number of tests revealed that the ratio technique was slightly more accurate and, subsequently, the algebraic portion of the algorithm was removed.

Section 4

Analytical and Modeling Developments

To develop material models and life prediction capability for metal matrix composites, it was necessary to conduct a thorough evaluation of the stress and strain states generated in the composite under typical processing and service conditions. The determination of thermally induced residual stresses has been a major concern in the development of metal matrix composites. During the cooling of these composites, which are usually processed at very high temperatures and pressures, residual stresses develop within both the fibers and the matrix due, primarily, to the thermally induced strains caused by the fiber/matrix thermal expansion mismatch. In metal matrix composites, the difference between the fiber and matrix coefficients of thermal expansion (CTE) results in very high stresses at room temperature that can cause matrix yielding and microcracking. The residual stresses can also influence the material behavior under subsequent application of thermomechanical loadings.

In the following subsections, analytical results are presented for the stress and strain states in a composite and its components subjected to simulated processing and service conditions. The final subsection summarizes results from an electric potential analysis of a common crack growth test specimen.

4.1 Elementary Elasticity Solutions

4.1.1 Uniaxial Model

The simplest model for a unidirectional composite was based on uniaxial stress states in the matrix and the fiber. The matrix and the fiber were modeled as two infinite strips bonded together having the same relative cross-sectional area as in the composite (Fig. 4.1.1-1a).

The uniaxial model approximated the axial stresses in the fiber and the matrix under temperature changes and an axial external force. The axial strains were equal for the fiber and

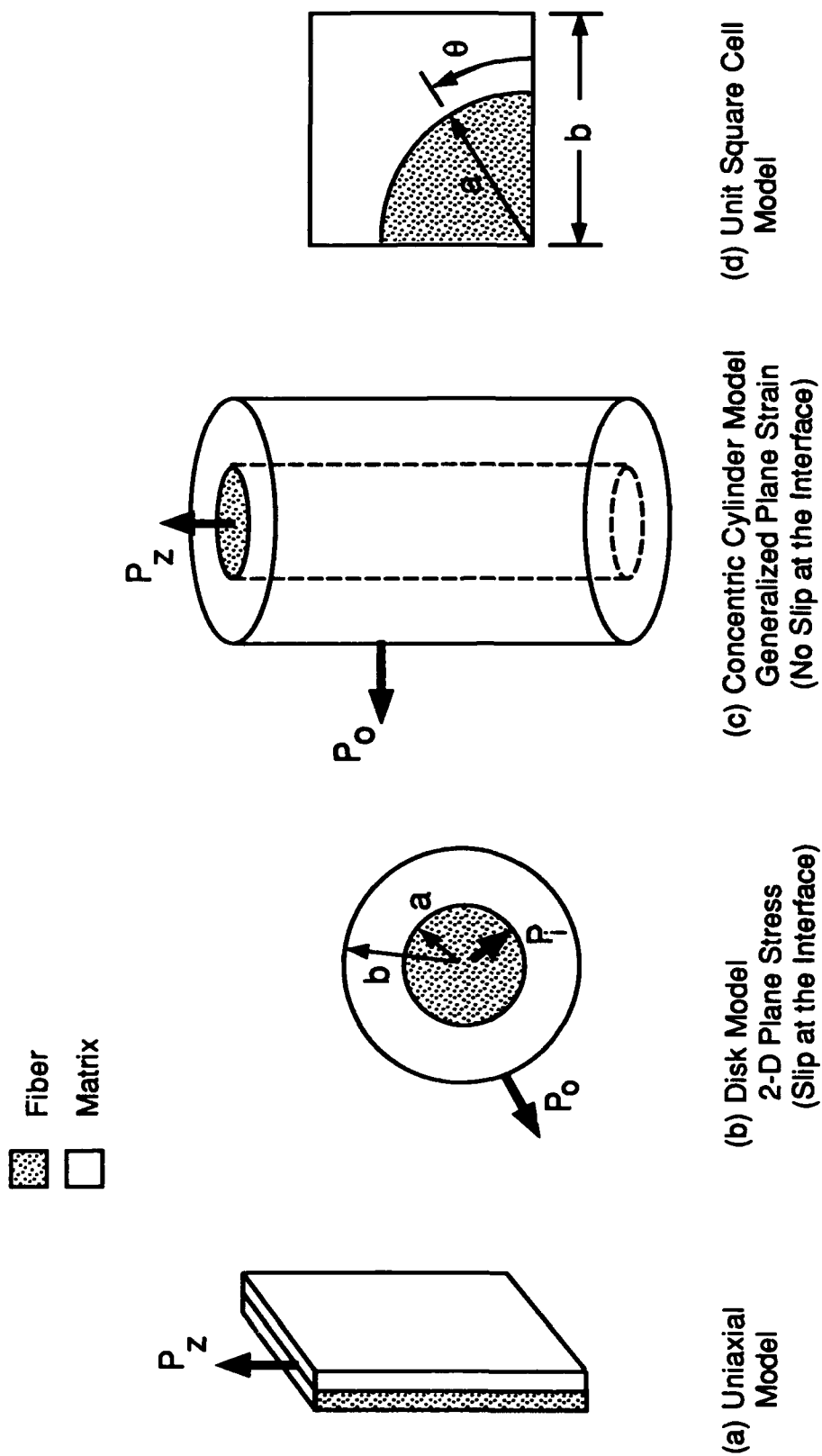


Fig. 4.1.1-1 Models Used in the Analysis of Unidirectional Composites.

the matrix and the sum of the forces were equal to the applied mechanical load. The stresses in the matrix and fiber were given by:

$$\sigma_m = \frac{E_m}{E_c} [-V_f E_f (\alpha_m - \alpha_f) \Delta T + P_z],$$

$$\sigma_f = \frac{E_f}{E_c} [(1 - V_f) E_m (\alpha_m - \alpha_f) \Delta T + P_z],$$

where:

(1)

$$E_c = V_f E_f + (1 - V_f) E_m$$

V_f is the volume fraction of fiber, P_z is the applied axial stress, ΔT is the change in temperature, E_m and E_f are the elastic moduli of the matrix and the fiber, respectively, and α_m and α_f are the thermal expansion coefficients of the matrix and the fiber, respectively.

4.1.2 Disk and Concentric Cylinder Models

The concentric cylinder model for a unidirectional composite provided a more realistic simulation of the stress and strain distributions than a uniaxial model or a two-dimensional planar model. Even though simplifying plane-stress or generalized plane-strain assumptions were made, the results could yield appropriate three-dimensional field distributions.

The two-dimensional plane-stress analysis of the disk model (Fig. 4.1.1-1b) provided radial and hoop stresses for thermal and radial loading conditions applied to a composite with a very weak bond at the fiber/matrix interface. For the boundary conditions, the radial stresses and radial displacements were continuous at the fiber/matrix interface, a radial stress of P_o was applied at the outer radius, of the matrix and the stresses were finite at the center of the fiber. For continuity of the radial displacements, the radial stress at the interface was assumed to be negative under thermal and radial loading conditions. Using the equilibrium and compatibility

equations together with the radial stress boundary conditions, the stresses [Timoshenko] for the fiber were given by:

$$\sigma_{rf} - \sigma_{\theta f} = P_i \quad (2)$$

and for the matrix:

$$\begin{aligned} \sigma_{rm} &= \frac{P_o b^2 - P_i a^2}{b^2 - a^2} + \frac{(P_i - P_o) a^2 b^2}{b^2 - a^2} \frac{1}{r^2} \\ \sigma_{\theta m} &= \frac{P_o b^2 - P_i a^2}{b^2 - a^2} - \frac{(P_i - P_o) a^2 b^2}{b^2 - a^2} \frac{1}{r^2} \end{aligned} \quad (3)$$

where [Ashbaugh et al., 1990]:

$$P_i = \frac{\frac{2P_o}{E_m (1 - V_f)} + (\alpha_m - \alpha_f) \Delta T}{\frac{1}{E_m} \left(\frac{1 + V_f}{1 - V_f} + \nu_m \right) + \frac{1}{E_f} \nu_f}, \quad (4)$$

P_i is the stress at the interface, P_o is the external radial stress, V_f is the volume fraction of the fiber, a is the radius of the fiber, b is the radius of the matrix, ν_f and, ν_m are the Poisson's ratios for the fiber and matrix, respectively.

The generalized plane-strain model incorporated external stresses P_o and P_z acting in the radial and axial directions, respectively, as shown in Fig. 4.1.1-1c, and thermally induced strains.

For this analysis the following assumptions were made:

- (1) Axially symmetric behavior of the fiber and matrix element (no shear),
- (2) No slip at the interface,

- (3) Constant temperature change throughout the composite,
- (4) Linear elastic behavior of the fiber and matrix,
- (5) Isotropic properties for the fiber and matrix,
- (6) An initial stress-free state,
- (7) Plane sections remain as planes,
- (8) Continuity of radial stress and radial displacement at the interface.

The details of the derivation of the general stress expressions for this axisymmetric linear elastic problem could be found in the literature [Timoshenko].

The following boundary conditions were used in the solution:

- (1) Radial stress at $r=b$ was equal to applied radial stress P_o ,
- (2) Radial displacements at the interface were equal for the matrix and fiber,
- (3) Axial displacements for the matrix and fiber were uniform and equal,
- (4) Radial stresses at $r=a$ for the matrix and fiber were equal,
- (5) The integration of the axial stresses over their respective areas in the matrix and fiber equaled to the applied mean axial stress P_z , and
- (6) The stresses at the center of the fiber were finite.

For the generalized plane-strain solution [Ashbaugh et al, 1990], the stresses in the matrix became:

$$\begin{aligned}
 \sigma_{rm} &= A \left(1 - \left(\frac{b}{r} \right)^2 \right) + P_o \left(\frac{b}{r} \right)^2, \\
 \sigma_{\theta m} &= A \left(1 + \left(\frac{b}{r} \right)^2 \right) - P_o \left(\frac{b}{r} \right)^2, \\
 \sigma_{zm} &= C,
 \end{aligned}
 \tag{5}$$

and the stresses in the fiber:

$$\begin{aligned}\sigma_{rf} &= A \left(1 - \left(\frac{b}{a}\right)^2\right) + P_o \left(\frac{b}{a}\right)^2, \\ \sigma_{\theta f} &= \sigma_{rf}, \\ \sigma_{zf} &= C \left(1 - \left(\frac{b}{a}\right)^2\right) + P_z \left(\frac{b}{a}\right)^2,\end{aligned}\tag{6}$$

where:

$$\begin{aligned}A &= \frac{n}{sm-pn} \left(\left(\frac{b}{a}\right)^2 (u_1 - u_2 \frac{m}{n}) + (\alpha_m - \alpha_f) \Delta T \right), \\ C &= \frac{s}{sm-pn} \left(\left(\frac{b}{a}\right)^2 (u_1 - u_2 \frac{p}{s}) + (\alpha_m - \alpha_f) \Delta T \right),\end{aligned}\tag{7}$$

and:

$$\begin{aligned}m &= \left(1 - \left(\frac{b}{a}\right)^2\right) \frac{1}{E_f} - \frac{1}{E_m}, \\ n &= \left(1 - \left(\frac{b}{a}\right)^2\right) \frac{(1 + \nu_f)}{E_f} - \frac{(1 + \nu_m)}{E_m}, \\ p &= 2 \left(1 - \left(\frac{b}{a}\right)^2\right) \frac{\nu_f}{E_f} - 2 \frac{\nu_m}{E_m}, \\ s &= \left(1 - \left(\frac{b}{a}\right)^2\right) \frac{(1 + \nu_f)}{E_f} - \left(1 + \left(\frac{b}{a}\right)^2\right) \frac{(1 + \nu_m)}{E_m}, \\ u_1 &= P_o \frac{2\nu_f}{E_f} - \frac{P_z}{E_f}, \\ u_2 &= (P_o - P_z) \left(\frac{(1 + \nu_f)}{E_f} \right) - P_o \frac{(1 + \nu_m)}{E_m}.\end{aligned}\tag{8}$$

A comparative study was conducted of the stresses resulting from these three models (Fig. 4.1.1-1a-c) and from the unit square cell model (see Section 4.3). In all cases, calculations were based on a composite (a 35% fiber volume fraction) that was subjected to a temperature increase of 100°C. Typical room temperature properties were assumed for a silicon carbide fiber and a titanium aluminide matrix; these are given in Table 4.1.2-1. The resulting stresses are compared in Table 4.1.2-2. The effective stress, given in the last line of Table 4.1.2-2:

$$\sigma_{eff} = \frac{1}{\sqrt{2}} [(\sigma_r - \sigma_\theta)^2 + (\sigma_\theta - \sigma_z)^2 + (\sigma_r - \sigma_z)^2]^{1/2}, \quad (9)$$

was used to determine yielding (von Mises criterion) for a complex stress state, assuming no shearing stress.

Because of the assumptions made, the uniaxial model did not produce transverse stresses and the disc model did not produce axial stresses. The two stresses listed for the unit square cell finite element model were for angles of 0° and 45° (see Fig. 4.1.1-1d); these stresses correspond to the limiting stress values.

When no bonding at the interface was simulated in the disk model the radial hoop, and axial stresses, were all lower in magnitude than those obtained from the perfectly bonded concentric cylinder and unit square cell models. The axial stresses computed from the uniaxial model approximated the stress values obtained from the concentric cylinder and unit square cell models. As expected, the more realistic models (triaxial stress state) resulted in substantially higher σ_{eff} stresses in the matrix.

Table 4.1.2-1 Elastic Properties Used for Comparative Calculations

	Fiber	Matrix
Modulus (GPa)	413.7	65
Poisson's Ratio	0.3	0.3
CTE (E-6/ $^{\circ}$ C)	4.86	10.6

Table 4.1.2-2 Stresses in the Fiber and the Matrix at Fiber/Matrix Interface for a 100 $^{\circ}$ C Temperature Increase

	Uniaxial Model	Disk Model	Concentric Cylinder Model	Unit Square Cell Model for Θ = 0, = 45
σ_r -matrix	0	15.0	20.5	27.8, 15.2
σ_{Θ} -matrix	0	-31.2	-42.7	-41.2, -44.2
σ_r -fiber	0	15.0	20.5	27.4, 15.1
σ_z -matrix	-28.9	0	-35.5	-32.9, -33.0
σ_z -fiber	53.6	0	66.0	66.8, 66.1
σ_{eff} -matrix	28.9	40.8	59.9	65.7, 54.7

4.1.3 Analysis for Orthotropic CTE

Several references were available on the analysis of a concentric cylinder model with anisotropic properties [Vedula et al.; Mikata et al.]. However, these previous works assumed isotropic CTE in the transverse plane. To investigate the effect of anisotropic CTE in the transverse plane on the residual stresses, stress analyses of hollow and solid cylinders with orthotropic CTE properties in the r and Θ directions were conducted.

Using the equilibrium equation, strain-displacement relations and the constitutive relations with orthotropic CTEs taken into account, the radial displacement, u , was derived in a similar fashion to previous derivations [Ashbaugh et al.]:

$$u = k r \ln r + c_1 r + \frac{c_2}{r},$$

where:

(10)

$$k = -(\alpha_\theta - \alpha_r)(1 - \nu) \frac{\Delta T}{2},$$

and r is the radial distance, c_1 and c_2 are constants, α_r and α_θ are the radial and hoop CTEs, respectively, ν is the Poisson's ratio, and ΔT is the temperature change from the zero stress reference temperature. For isotropic CTE, the constant k is zero and the classical solution is obtained [Timoshenko].

Using Equation 10 for the displacement, the stresses are computed for a solid cylinder and a hollow cylinder. For a solid cylinder, the stresses and displacements at the center must be finite and be well defined. Therefore, $c_2 = 0$ and $k = 0$. This implies that the CTE for a solid cylinder cannot be orthotropic in the plane. For a hollow cylinder, with zero stress boundary conditions at the inner and outer surfaces, radial and hoop stresses become:

$$\sigma_r = \frac{E k}{1 - \nu} \frac{a^2 b^2}{b^2 - a^2} \left[\frac{1}{a^2} \ln \left(\frac{r}{b} \right) - \frac{1}{b^2} \ln \left(\frac{r}{a} \right) - \frac{1}{r^2} \ln \left(\frac{a}{b} \right) \right],$$

(11)

$$\sigma_\theta = \frac{E k}{1 - \nu} \frac{a^2 b^2}{b^2 - a^2} \left[\frac{1}{a^2} \ln \left(\frac{r}{b} \right) - \frac{1}{b^2} \ln \left(\frac{r}{a} \right) + \frac{1}{r^2} \ln \left(\frac{a}{b} \right) + \frac{b^2 - a^2}{a^2 b^2} \right],$$

where σ_r and σ_θ are the radial and hoop stresses, a and b are the inner and outer radii of the cylinder, respectively.

The stress distribution in the hollow cylinder for a temperature change of -100°C is plotted in Fig. 4.1.3-1. The properties used are shown in Table 4.1.3-1. The plot shows nonzero residual stress distribution for the hollow cylinder. The maximum radial stress of 3 MPa is reached near the center of the hollow cylinder. The tangential stress at the inner radius is tensile

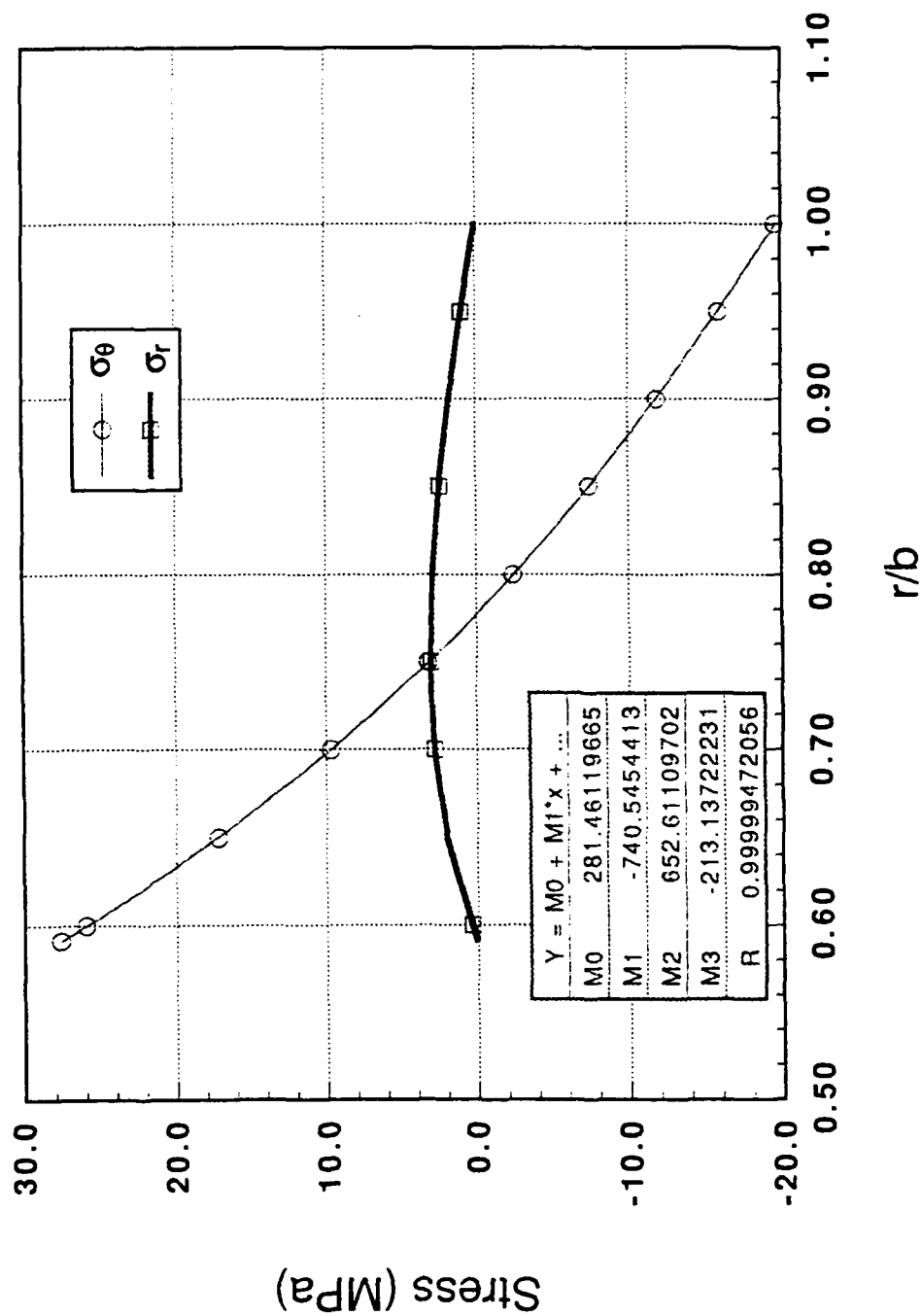


Fig. 4.1.3-1 Stress state in a hollow cylinder with orthotropic CTE, in plane stress subjected to a uniform temperature change.

and compressive at the outer radius and changes from about 27 MPa to -20 MPa for a 100°C drop in temperature. Hence, this analysis shows that significant residual stresses will accrue in the matrix material due to processing if the CTEs in the hoop and radial direction are different.

Table 4.1.3-1 Material and Geometrical Properties for the Hollow Cylinder used to Compute Stress Distribution Shown in Fig.4.1.3-1.

α_r (°C)	18.0E-6
α_θ (°C)	9.0E-6
E (GPa)	400
ν	0.3
a	$\sqrt{0.35}$
b	1.0
ΔT (°C)	-100

4.1.4 Closure Model

A model was developed [Johnson and Ashbaugh] for the analysis of crack closure and its effect on the stress-intensity factor at a crack tip of a center cracked panel in a uniaxially loaded infinite plate. This model incorporated contact of the crack surfaces caused by plastic deformation, asperities, or oxidation. The stress-intensity factor at the crack tip was obtained from superposition of the stress-intensity factors resulting from the applied loading and the contact stresses on the crack surface. The model included contact occurring adjacent to the crack tip or anywhere along the crack length. The effect of this crack-surface contact on the displacement across the middle of a crack has been evaluated with the model.

The information from the crack contact model has been compared to experimental load and displacement data from various sources, especially from a laser-interferometric displacement gage (LIDG). The actual crack-contact size and the stresses on the contact surface were estimated through this comparison. The range of the stress-intensity factor associated with the range of the applied load was estimated through an evaluation of the load-displacement relationships near the crack tip. This information was used to correlate fatigue-crack propagation data influenced by different levels of crack closure.

4.2 Finite Difference Technique for Elastic-Plastic Analysis

Previous linear elastic analyses predicted stress states which would exceed the yield state of the matrix. In addition, the mechanical properties of the constituents of metal matrix

composites were highly temperature-dependent. Therefore, an inelastic constitutive model with temperature dependent properties was required to accurately model the behavior of these composites.

Various finite element packages could predict the stress and strain distributions around the fiber. However, these codes were developed for mainframe computers and would require familiarity with finite element analysis to execute. To support the design of a large number of experiments on various composite systems, a PC based user-friendly program was required. A PC compatible computer program called FIDEP (Finite Difference Code for Elastic-Plastic Analysis) was developed to fulfill this requirement. The theory is briefly reviewed in Section 4.2.1 and some results are shown in Section 4.2.2.

4.2.1 Model for Unidirectional Composite

An effort was directed at developing a model to predict stresses and strains in a unidirectional metal-matrix composite subjected to processing conditions and thermomechanical cyclic loading. A representative volume element of the composite was approximated by two concentric cylinders with the inner cylinder representing the fiber and the outer cylinder representing the matrix (Fig. 4.2.1-1). The fiber and the matrix radii were a and b , respectively, and the direction of the z -axis was along the fiber.

A generalized plane-strain state in the z -direction has been imposed where the axial strains were uniform and equal in both the fiber and the matrix. No spatial variation in temperature was assumed to occur. A perfect bond existed between the matrix and fiber so that no slippage or separation of the constituents was allowed. The concentric cylinders were subjected to axisymmetric loadings and displacements so that the shear stresses were zero. Both of the constituents were assumed to be isotropic. The matrix followed a von Mises yield surface and was incompressible in the plastic region, i.e., hydrostatic stresses did not cause plastic deformation. The plastic deformation was governed by the Prandtl-Reuss flow rule.

The boundary conditions used to obtain the subsequent results for this model were 1) zero radial stress at the surface of the outer cylinder, 2) finite stresses at the center, and 3) continuous radial stress and radial displacement at the fiber/matrix interface.

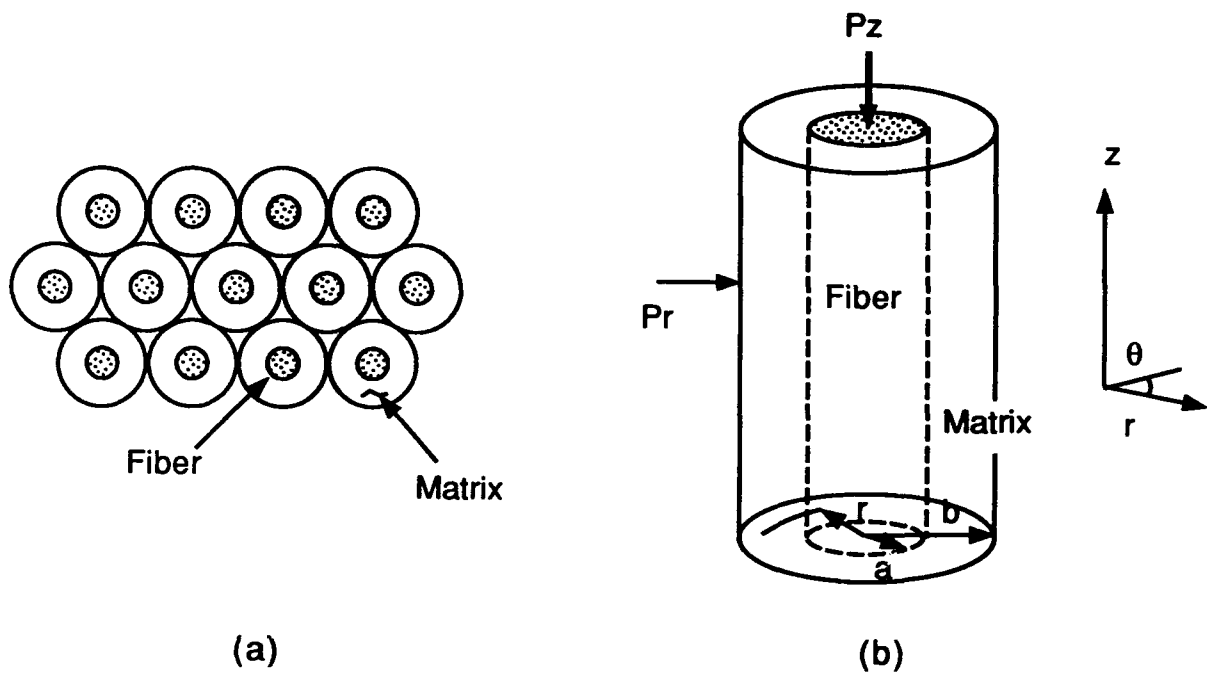


Fig. 4.2.1-1 (a) Concentric cylinder idealization of a unidirectional composite, (b) Representative volume element of a unidirectional composite represented by the concentric cylinder model.

The derivation of the elastic-plastic concentric cylinder equations [Coker and Ashbaugh, 1991b] followed very closely to a previous derivation [Mendelson]. Incremental plastic strains were determined using a modified total strain method. In this method the Prandtl-Reuss equations were modified to relate the incremental plastic strains to modified total strains instead of the stresses. Modified total strains are defined as total strains minus the current plastic strain increments. The advantage of this method is its convergence for most loading cases and material plastic behaviors. Using this analysis technique, a computer code called FIDEP (Finite Difference Code for Elastic-Plastic Analysis) was developed.

Initially, the algorithm for FIDEP, shown in Fig. 4.2.1-2, read the temperature dependent material data and the loading from a tabular input file. The temperature and the load were divided into steps and the load and the temperature were incremented to the first step. The finite difference equations were solved elastically for the new stress state. A new yield surface was computed for the present temperature at all stations. The effective stress was compared to this new yield surface for each station. If the effective stress was less than the yield strength (or flow stress) at all nodes, the next thermal and mechanical load increment would be applied. Otherwise, a plastic strain increment was assumed. The finite difference equations, with the assumed plastic strain increment, were solved for the stresses. The modified total strains and the equivalent total strain were computed. The effective incremental plastic strain was computed from the uniaxial curve and finally the new incremental plastic strains were computed from the plastic strain-modified total strain relations. These strains were then compared with the previous plastic strain increments, and if the difference was less than a certain value, the next loading increment was applied. Otherwise, the finite difference equations were solved with the new incremental plastic strains and the plastic subroutine was repeated until convergence of the incremental plastic strains is obtained.

The code was verified with finite element analysis (Section 4.3) for a cool down from a processing temperature for a model material. In Fig. 4.2.1-3, the stresses in the matrix at the fiber/matrix interface computed by FIDEP and the finite element analysis are plotted as a function of temperature. During cool down, the stresses increased elastically until the yield surface was reached after which plastic deformation with strain hardening occurred. The two methods were found to be in excellent agreement.

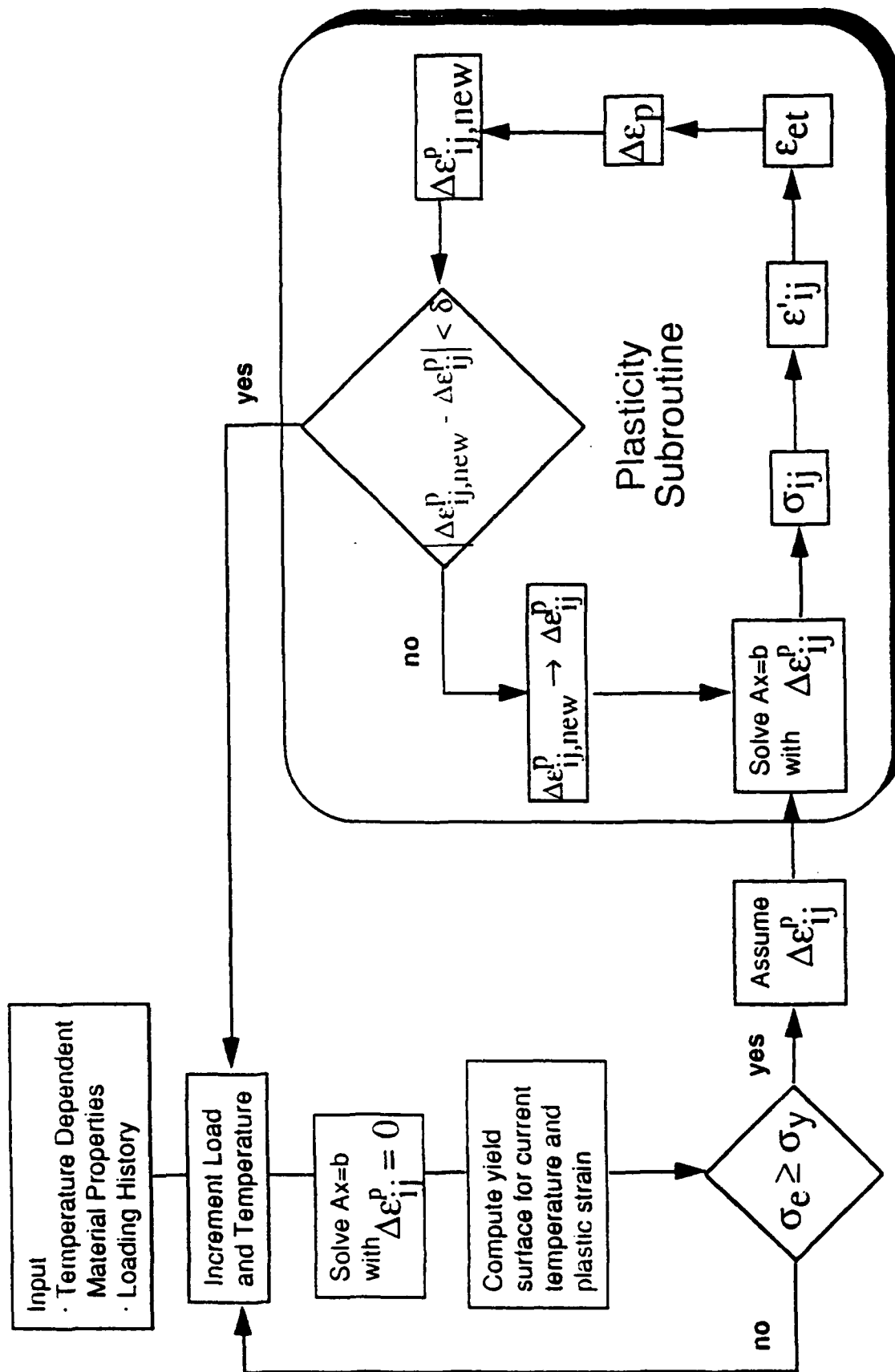


Fig. 4.2.1-2 Elastic-Plastic Algorithm.

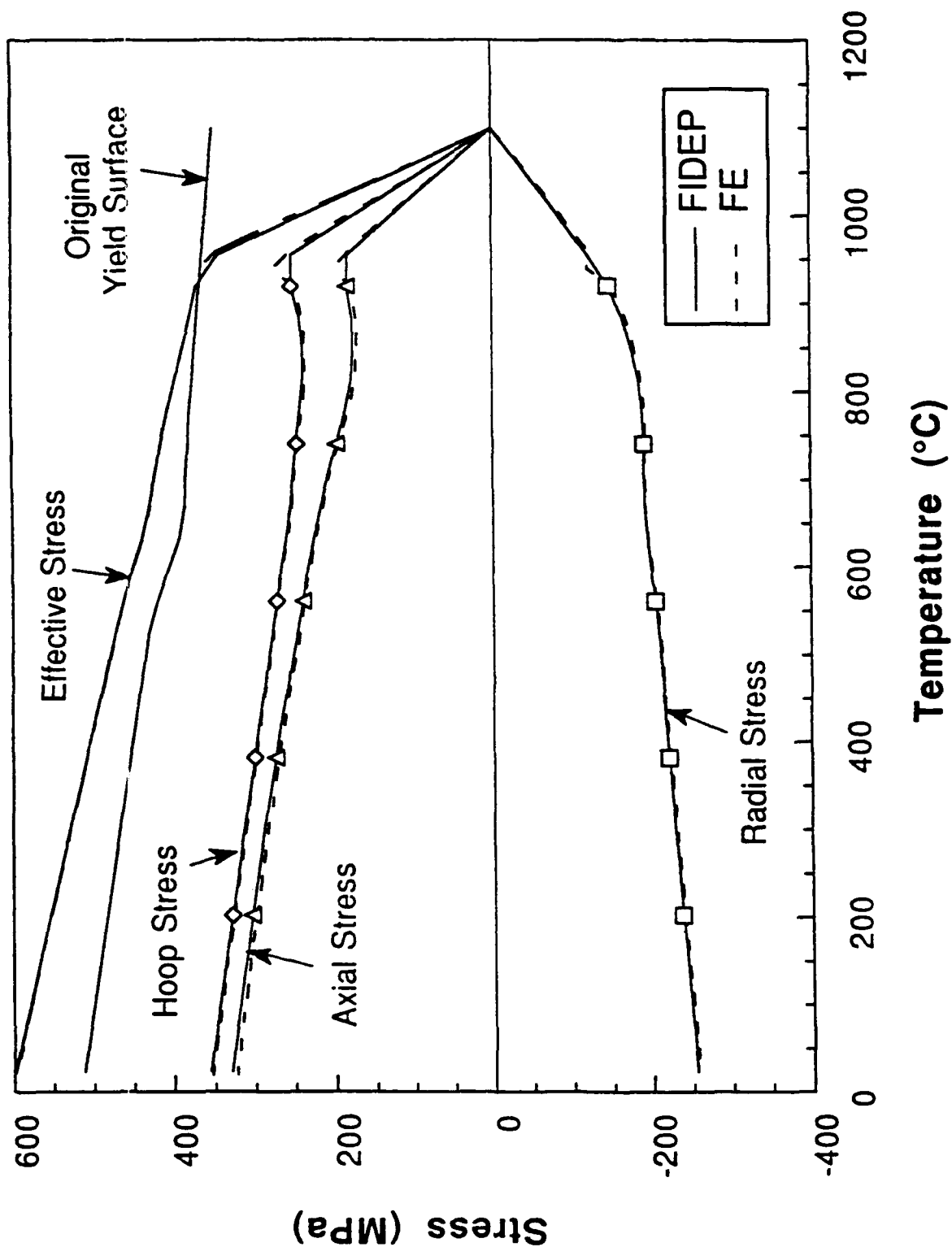


Fig. 4.2.1-3 Comparison of the stresses at the fiber/matrix interface for a model material during cool down from processing temperature as predicted by FIDEP and the Finite Element Analysis

4.2.2 Results for an MMC

Analyses of processing, cyclic mechanical loading, cyclic thermal loading, and thermomechanical fatigue were conducted. In these analyses, the fiber (SCS-6) was assumed to be elastic with temperature independent modulus and Poisson's ratio, ν . The CTE for the fiber was temperature dependent. The titanium aluminide matrix properties were temperature dependent with the stress-strain behavior being characterized with a bilinear representation. The properties for this bilinear representation were the elastic modulus, E , the plastic modulus, E_P , and the initial yield strength σ_{ys} .

The bilinear material properties of titanium aluminide, Ti-24Al-11Nb, were determined from unidirectional stress-strain data [Gambone] for a variety of temperatures. The elastic and plastic bilinear moduli were evaluated from best-fit lines through the elastic and plastic portions, respectively of the data shown in Fig. 4.2.2-1. The high initial yield strength at room temperature (950 MPa) was chosen arbitrarily high to prevent the occurrence of plastic deformation (since none was apparent at room temperature.)

The fiber properties and matrix properties [Titanium Aluminide Composites] used in the analyses are given in Table 4.2.2-1. Values for the CTE are discussed in Section 5.1.1.2 of this report. Since the analyses were based on isotropic material behavior, the in-plane CTE values were used to characterize the matrix. The fiber volumetric content was 35%.

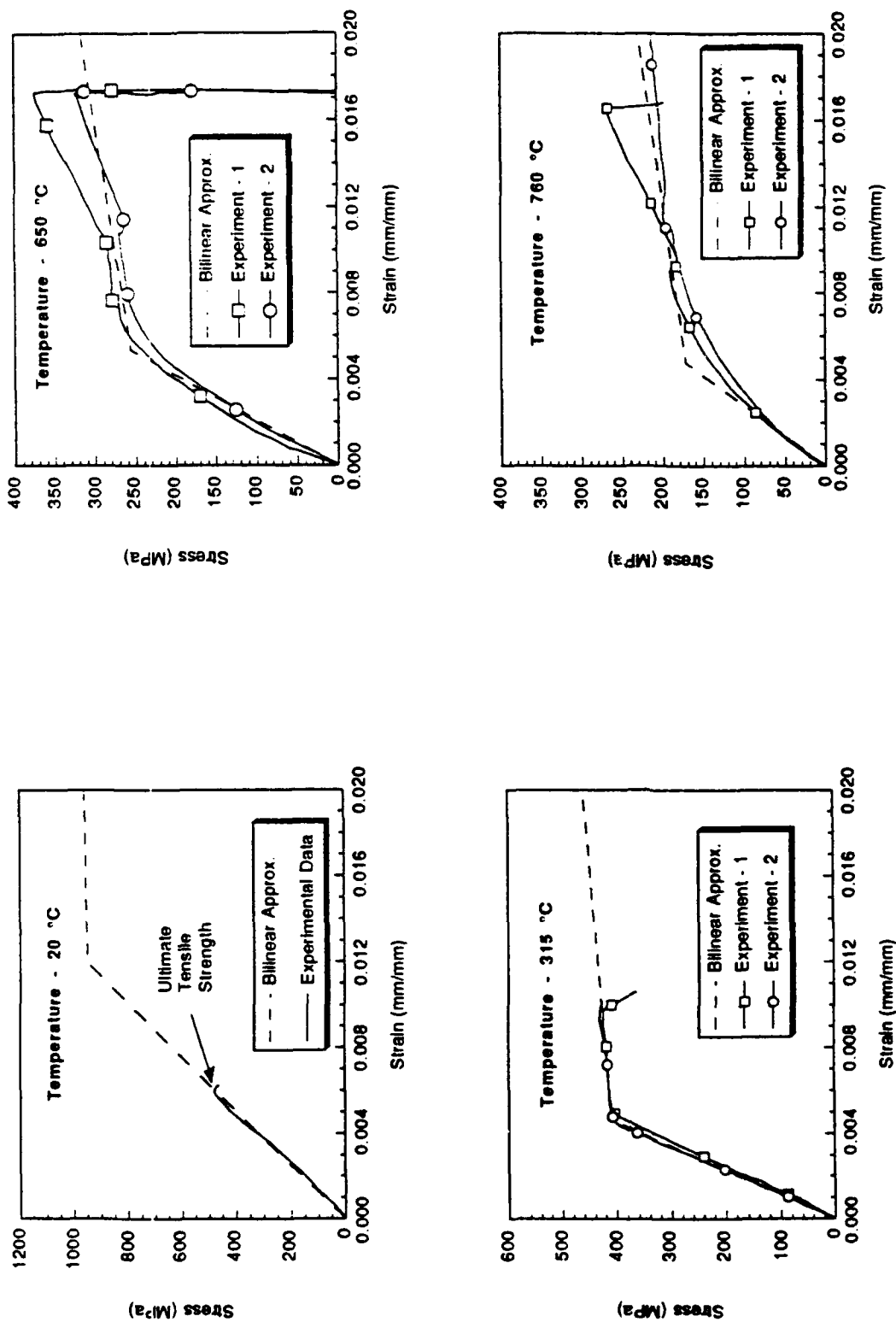


Fig. 4.2.2-1 Responses of fiberless Ti-24Al-11Nb foil at room and elevated temperatures and the bilinear approximations uniaxial stress-strain.

Table 4.2.2-1 Material Properties for SCS-6/Ti-24-11.

SCS-6 Fiber			
Temperature (°C)	E(GPa)	CTE* (1E-6/°C)	ν
20	414	4.70	0.22
93	414	4.81	0.22
204	414	4.97	0.22
316	414	5.12	0.22
427	414	5.26	0.22
538	414	5.38	0.22
649	414	5.50	0.22
760	414	5.60	0.22
871	414	5.70	0.22
982	414	5.78	0.22
1010	414	5.80	0.22

Ti-24-11 Matrix					
Temperature (°C)	E(GPa)	CTE* (1E-6/°C)	ν	σ_{ys} (MPa)	EP(GPa)
20	84.1	11.31	0.3	950.0	1.00
93	85.2	11.48	0.3	819.0	1.58
204	86.7	11.69	0.3	614.8	2.41
316	88.4	11.88	0.3	410.0	3.29
427	74.9	12.096	0.3	355.7	3.57
538	61.4	12.365	0.3	308.0	3.83
649	48.1	12.727	0.3	256.6	4.12
760	36.1	13.217	0.3	171.7	3.67
871	24.95	13.87	0.3	120.5	3.95
982	13.9	14.72	0.3	65.9	4.09
1010	11.25	14.98	0.3	53.8	4.15

* Secant CTE with reference temperature of 1010°C.

4.2.2.1 Material Processing

The stresses are assumed to be zero at the consolidation temperature of 1010°C. During cool down, the fiber and matrix constrain each other's movement so that stresses are created in each constituent. Figure 4.2.2.1-1 shows the axial, hoop, radial and effective stresses

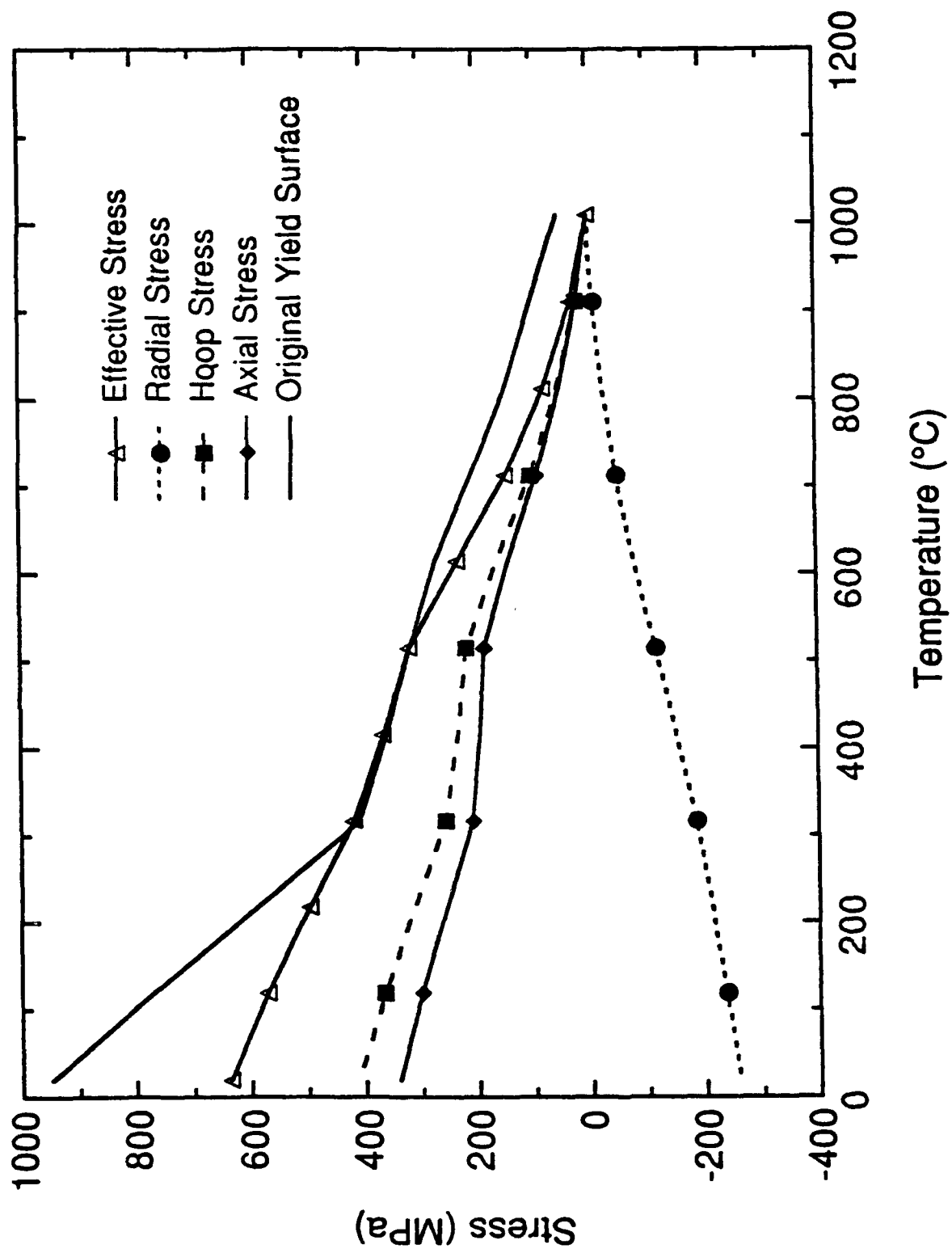


Fig. 4.2.2.1-1 Stresses in the matrix at the fiber/matrix interface during cool down from processing temperature for SCS-6/Ti-24-11 composite.

as the temperature is decreased to room temperature. This analysis has shown that, during consolidation, plastic deformation occurred at around 500°C when the effective stress reached the yield condition.

4.2.2.2 Cyclic Mechanical Loads

Cyclic mechanical loading was applied at 650°C and at room temperature to simulate isothermal fatigue. The loading histories, shown in Fig. 4.2.2.2-1, included the residual stresses from the consolidation phase. The x-axis denotes the number of computational steps used in the incremental plasticity solution. The maximum applied stress was 700 MPa and the stress ratio was 0.1. The axial stress behavior in the fiber and the matrix at the interface are shown as a function of temperature in Table 4.2.2.2-1.

Table 4.2.2.2-1 Approximate Axial Stress Results for the Fiber and the Matrix at the Fiber/Matrix Interface.

Temp. (°C)	Matrix Stress (MPa)				Fiber Stress (MPa)			
	σ_{\max}	σ_{\min}	$\Delta\sigma$	σ_{ave}	σ_{\max}	σ_{\min}	$\Delta\sigma$	σ_{ave}
20	600	300	300	450	600	-800	1400	-100
650	200	0	200	100	1500	0	1500	750

The maximum stress and the average stress were more severe for the matrix at room temperature and more severe for the fiber at 650°C. This transfer in severity was due to the fact that at high temperature the matrix yielded, because of a low yield stress surface and low modulus, and transferred most of the load to the fiber. At the two temperatures the stress ranges were approximately the same in each constituent.

Figure 4.2.2.2-2 shows the mechanical stress versus mechanical strain in the matrix. Some plasticity accrued at the higher temperature initially, but the stress-strain response at high temperature and low temperature stabilized after a couple of cycles. The moduli are equal to the rule of mixture moduli at those temperatures.

4.2.2.3 Cyclic Thermal Conditions

After cool down, the composite was thermally cycled between 650°C and 150°C. The stresses in the matrix at the fiber/matrix interface and the temperature dependent original yield

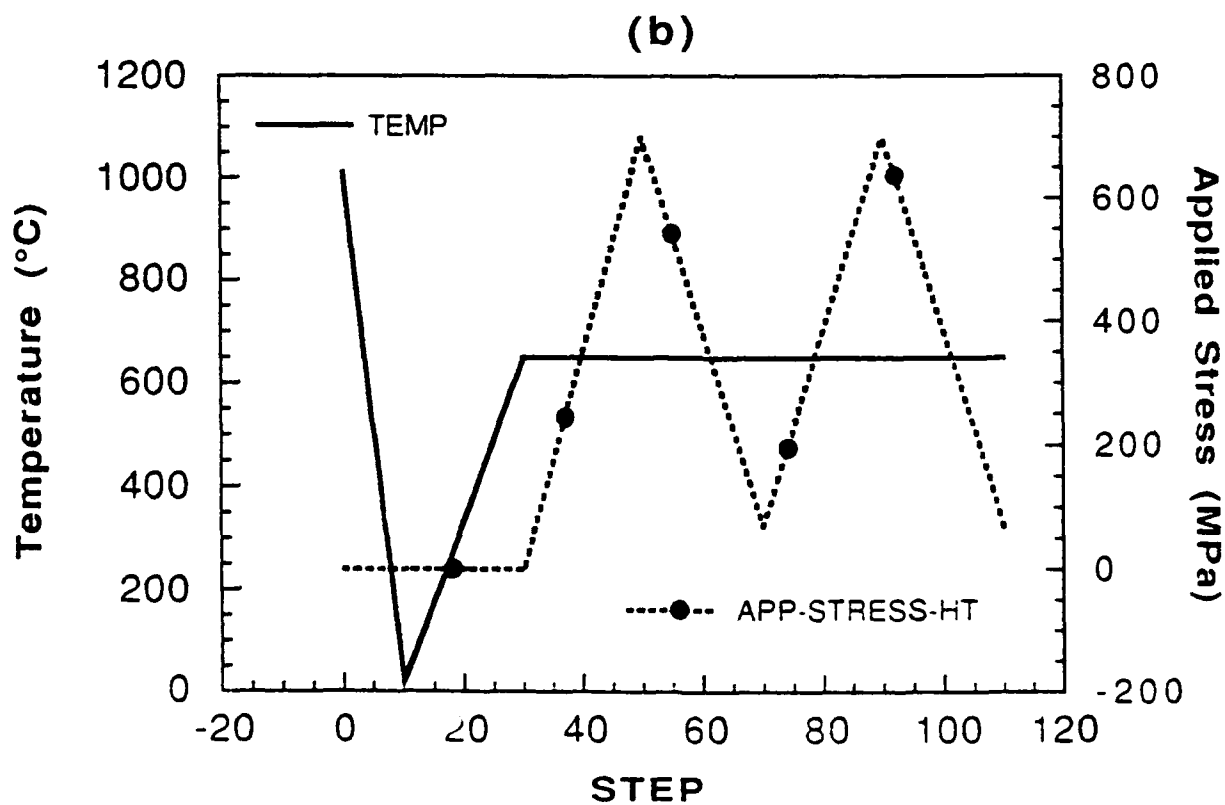
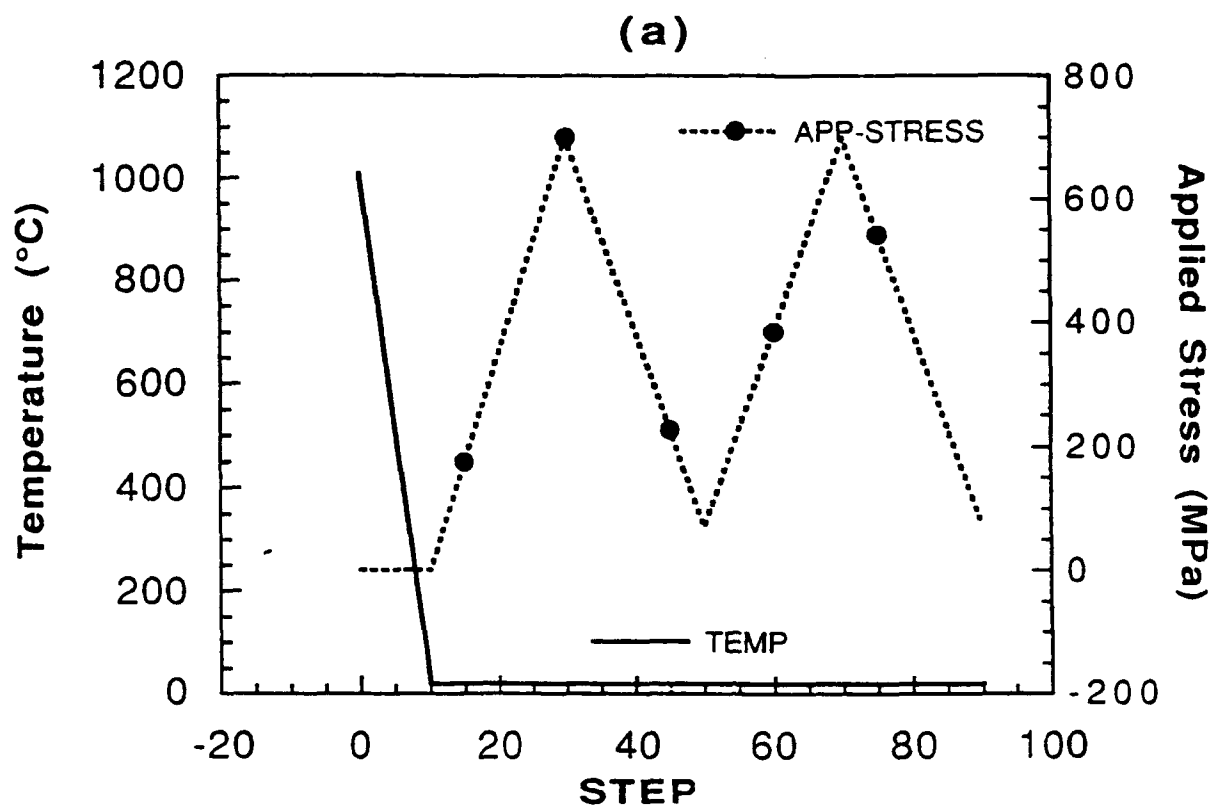


Fig. 4.2.2.2-1 Loading history for (a) room temperature and (b) 650°C isothermal fatigue simulations.

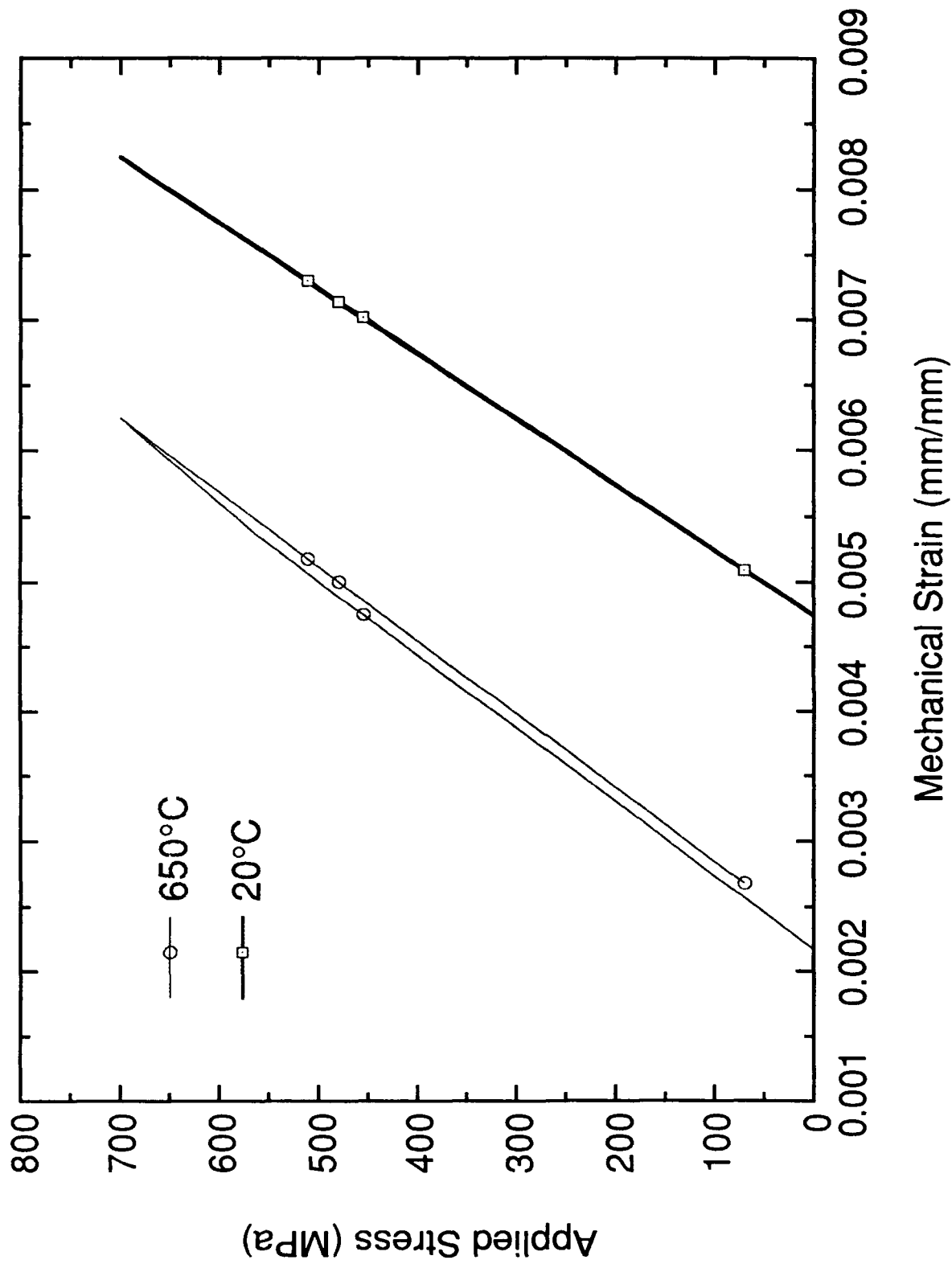


Fig. 4.2.2.2-2 Applied stress versus mechanical strain in the matrix at the fiber/matrix interface for isothermal loading.

surface before strain hardening are shown in Fig. 4.2.2.3-1. The results indicated that the stresses stabilized after two cycles.

Figure 4.2.2.3-2 shows the axial stress versus axial mechanical strain in the matrix for the thermal fatigue case and the two previous isothermal fatigue cases. The initial region before point 1 consisted of cool down from the 1010°C processing temperature to room temperature. The thermal cycling curve after point 1 is represented by triangles in Fig. 4.2.2.3-2. The two isothermal fatigue curves at 20°C and 650°C, represented by closed and open circles, bounded the thermal fatigue response.

4.2.2.4 Thermomechanical Fatigue

In-phase and out-of-phase thermomechanical fatigue were simulated using the FIDEP code. The conditions were the same as in experiments conducted in-house [Russ and Nicholas]. The maximum load for out-of-phase was 700 MPa and for in-phase was 650 MPa. The stress ratio was 0.1. The temperature profile consisted of consolidation from the processing temperature to room temperature and thermal cycling between 650°C and 150°C (Fig. 4.2.2.4-1).

The stress distributions in the composite in the out-of-phase case at minimum temperature and at maximum temperature are shown in Figs. 4.2.2.4-2a & b. At a given temperature, the stress distributions in the fiber were constant, and in the matrix they varied. The axial stress in the matrix did not necessarily attain its maximum at the interface. In this case, the maximum value occurred at the edge of the matrix which resulted from matrix yielding near the interface. At 650°C (and for a 70 MPa applied stress), almost no stress occurred in the matrix. At this high temperature, small compressive axial and hoop stresses and tensile radial stresses existed in the matrix; the fiber carried all of the load.

Figure 4.2.2.4-3 shows the axial stress history for the in-phase and out-of-phase cases in the matrix at the fiber/matrix interface. Again, these stresses were not necessarily the highest stresses in the matrix. The initial loading was due to cool down from processing temperature so that the stresses were identical in both cases. The stress curve repeated after a few cycles implying that no more plastic strain accumulation occurred; further strain increments were elastic. The out-of-phase loading created larger stress ranges and maximum stresses in the matrix than the in-phase loading. If the stress range in the matrix is the critical life parameter, these results could imply that out-of-phase loading is more severe for the matrix than in-phase loading.

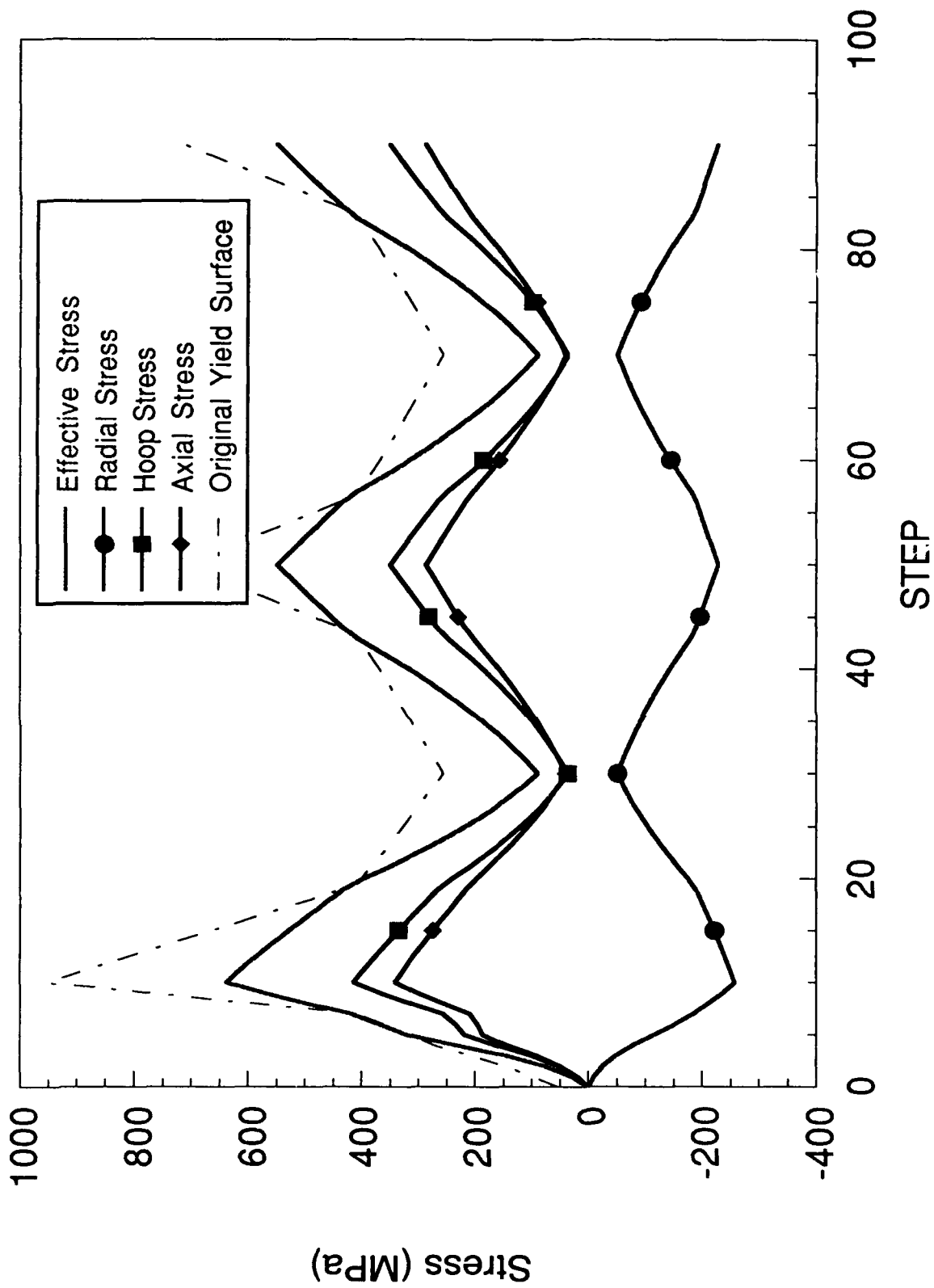


Fig. 4.2.2.3-1 Predicted stresses in the matrix at the fiber/matrix interface and the yield surface prior to strain hardening for thermal cycling between 600°C and 150°C.

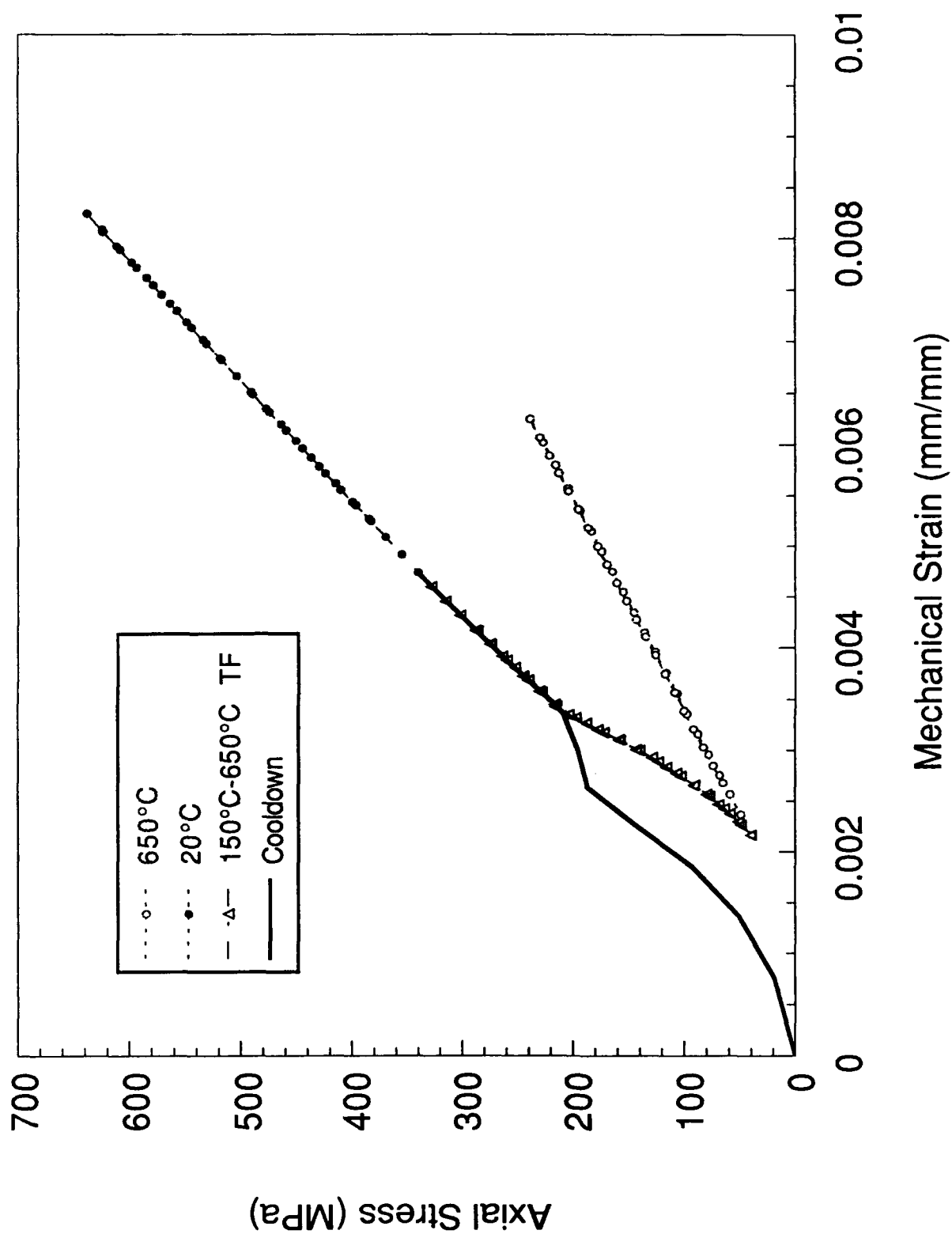


Fig. 4.2.2.3-2 Predicted axial stress versus predicted mechanical strain for isothermal fatigue and thermal fatigue cases.

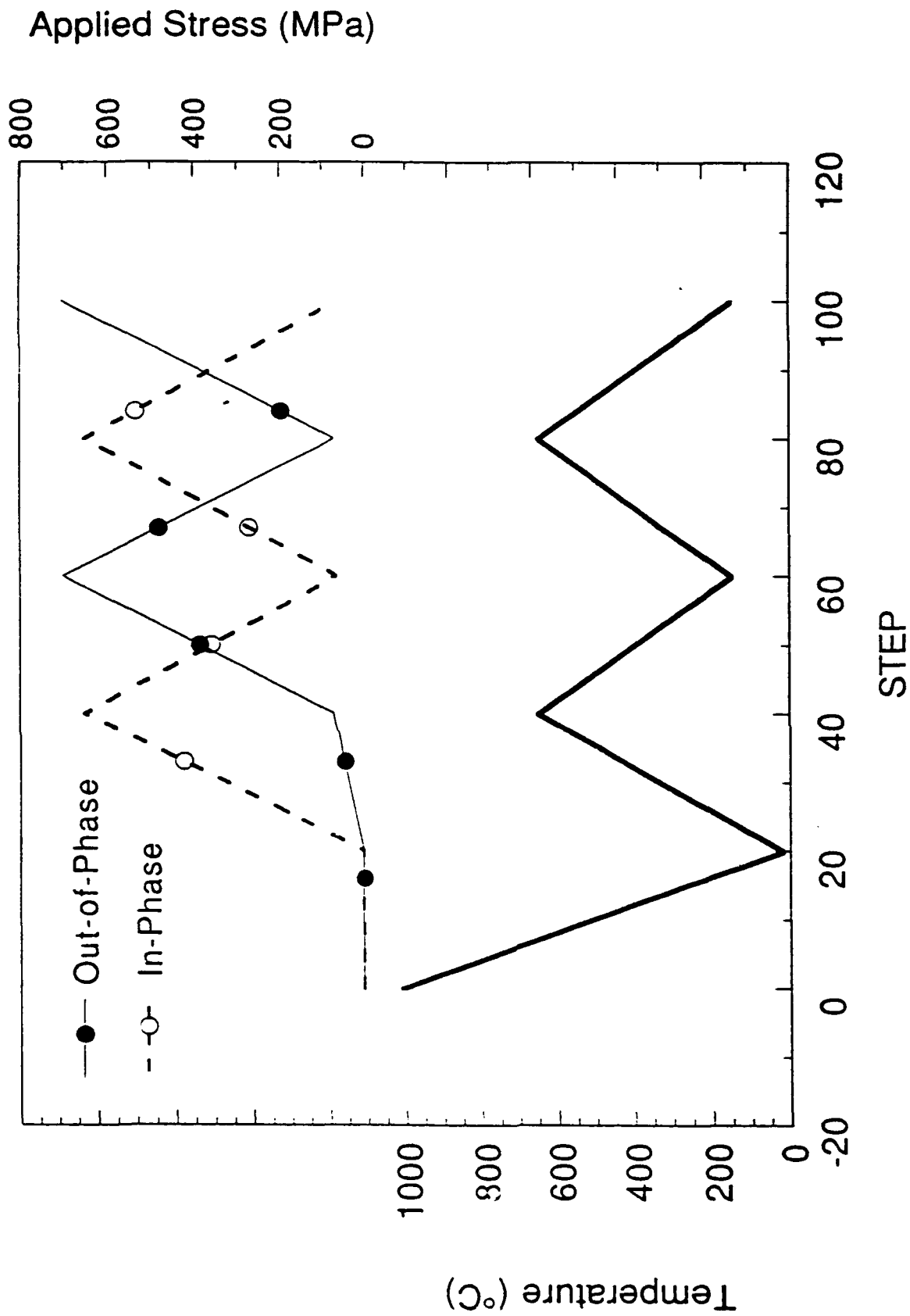


Fig. 4.2.2.4-1 Loading history for in-phase and out-of-phase thermomechanical fatigue simulation.

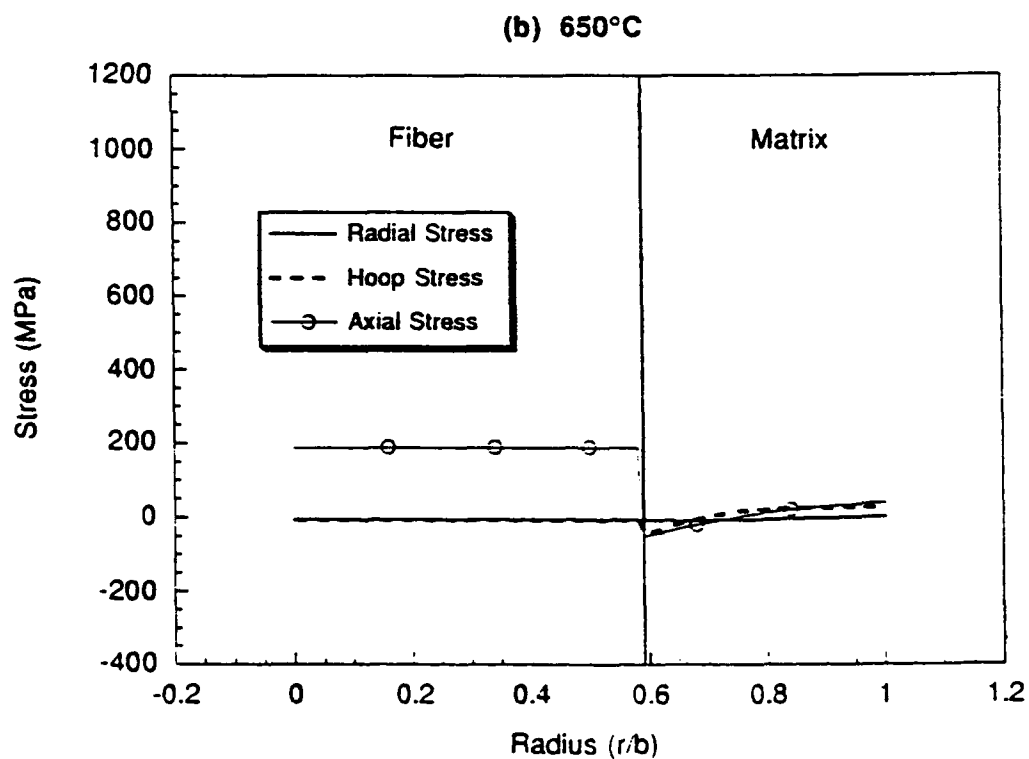
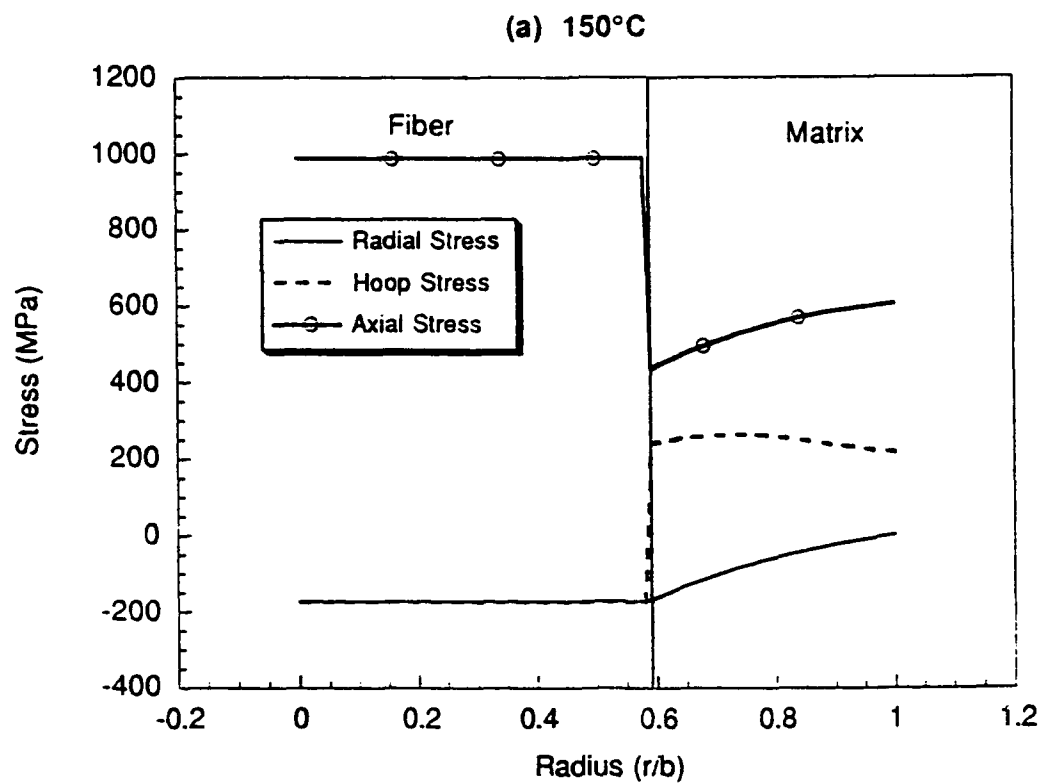


Fig. 4.2.2.4-2 Stress distribution in the composite at (a) 150°C and (b) 650°C for out-of-phase loading.

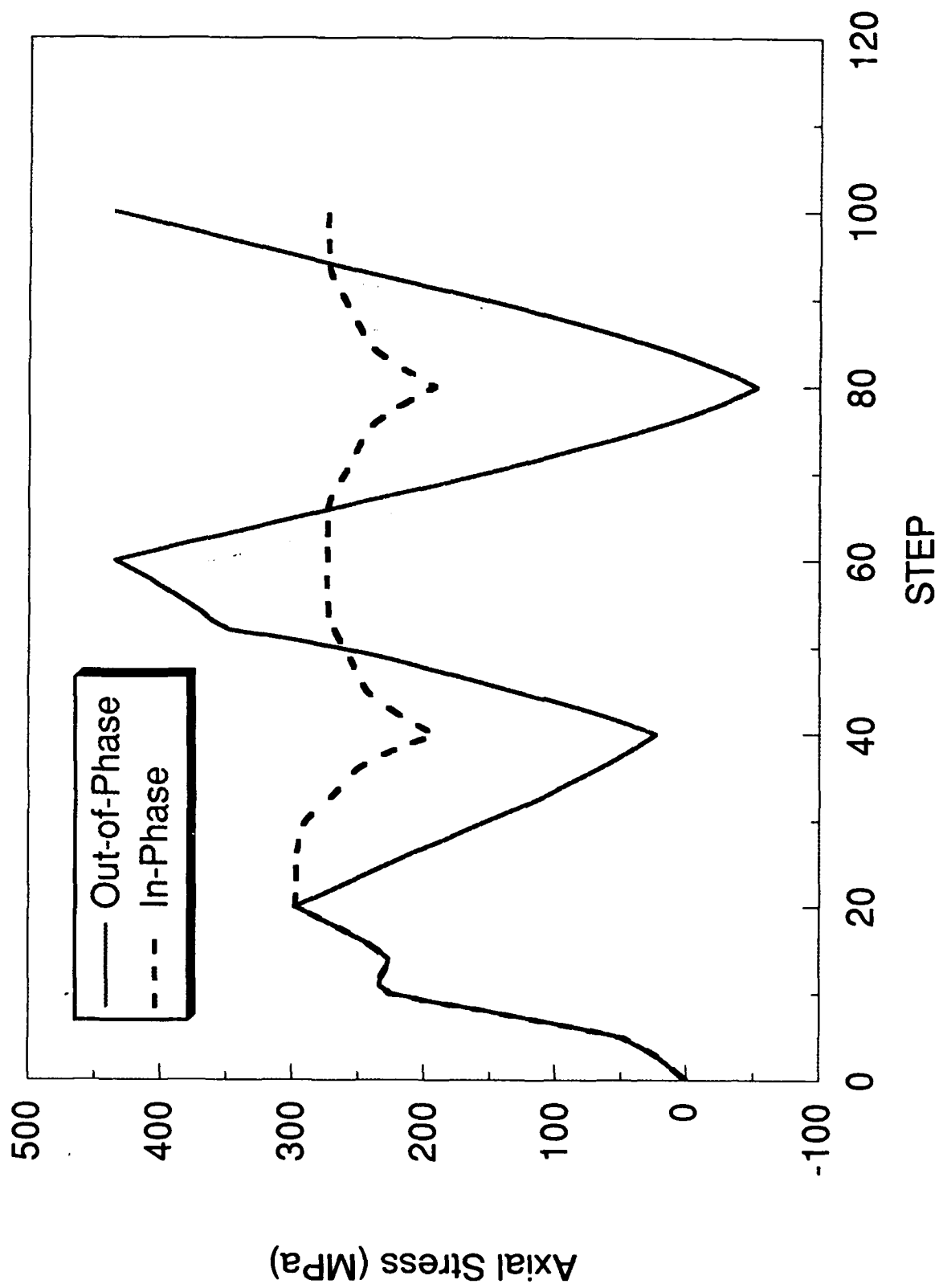


Fig. 4.2.2.4-3 Predicted axial stresses in the matrix at the fiber/matrix interface as a function of number of steps.

Figure 4.2.2.4-4 shows the axial stress in the fiber for the in-phase and out-of-phase TMF cases. After cool down, the maximum stress and the stress range in the in-phase case were higher than in the out-of-phase case. The thermal stresses in the fiber were compressive at room temperature so that an applied tensile load would be compensated by the thermal stresses.

Experimental applied stress-total strain curves [Russ and Nicholas] were compared with the predicted curves in Fig. 4.2.2.4-5. The experimental data were taken after a couple of hundred cycles. The predicted results were the stabilized stress-strain curves after 2-3 cycles. Excellent correlations were obtained between predicted and experimental stress-strain curves.

4.3 Finite Element Technique

The finite element method was employed to analyze the stress and strain distributions within the fiber and matrix materials of unidirectional composites subjected to thermal and mechanical loadings. Two- and three- dimensional geometries and complex fiber/matrix interface conditions have been modeled using the finite element method. The results presented in this section on finite element technique have been derived for material behavior based on a classical constitutive model. A small project [Sherwood] was initiated to optimize a unified constitutive model for later evaluation that is being implemented into the ADINA finite element program.

Since composite materials have been targeted for application in a high temperature environment with dynamic thermal and mechanical loading conditions, the composite models were subjected to a number of thermal and mechanical load histories. Preliminary investigations considered thermally induced stress states due to composite consolidations. Then, simplified cyclic load cases were conducted to isolate the response of the composite during simultaneous thermal and mechanical loading [Kroupa]. Additional investigations considered thermomechanical fatigue and transverse loaded composites.

4.3.1 Models for Unidirectional Composite

Preliminary investigations indicated that the one-dimensional models could not predict the multiaxial stress state found in unidirectional composites. For a tractable analysis, the concentric cylinder and the unit cell models, as shown in Fig. 4.3.1-1, were chosen to predict the multiaxial stress state. The concentric cylinder model was constructed in a two dimensional

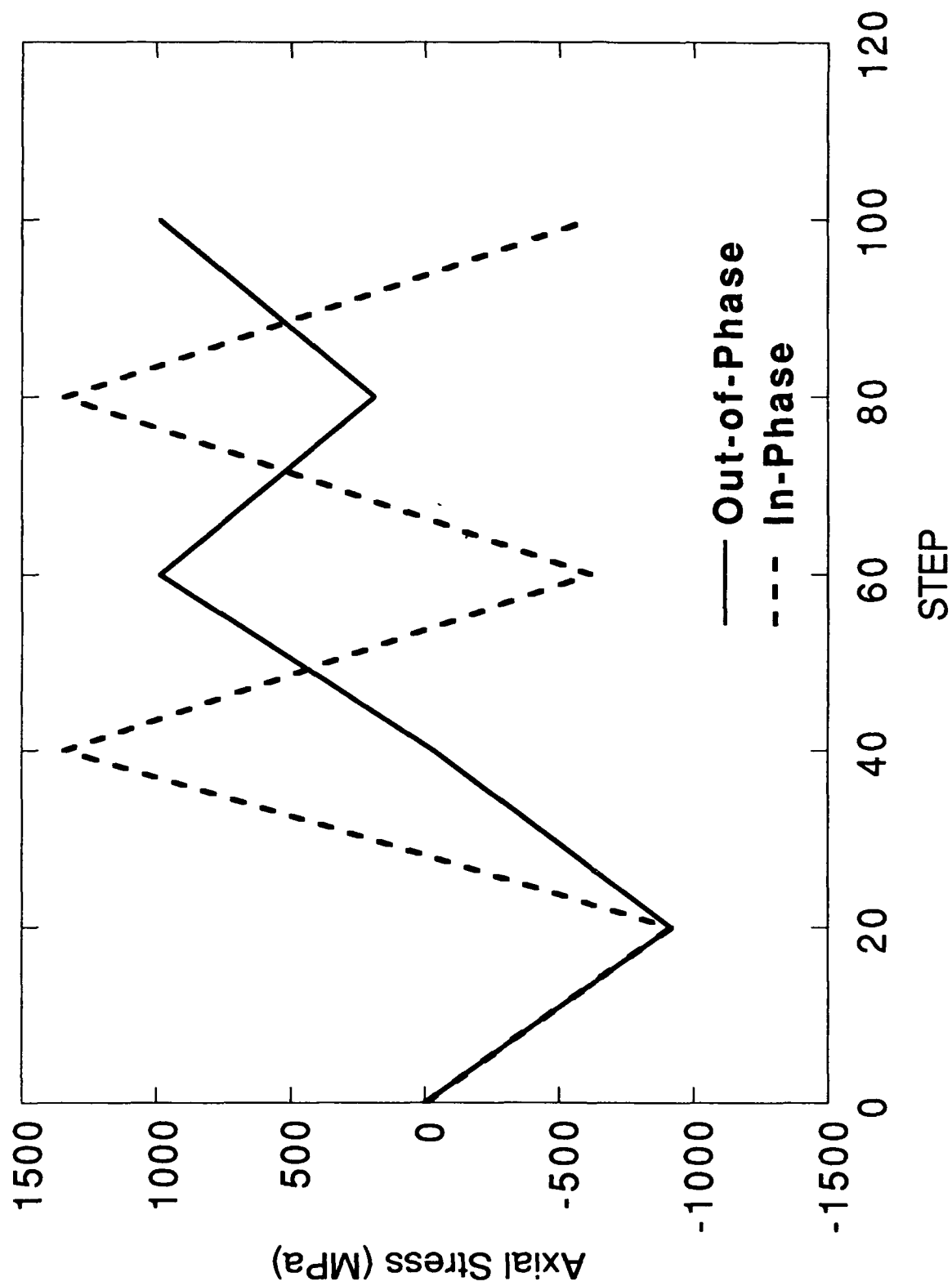


Fig. 4.2.2.4-4 Predicted axial stress peaks in the fiber for in-phase and out-of-phase loading as a function of number of steps.

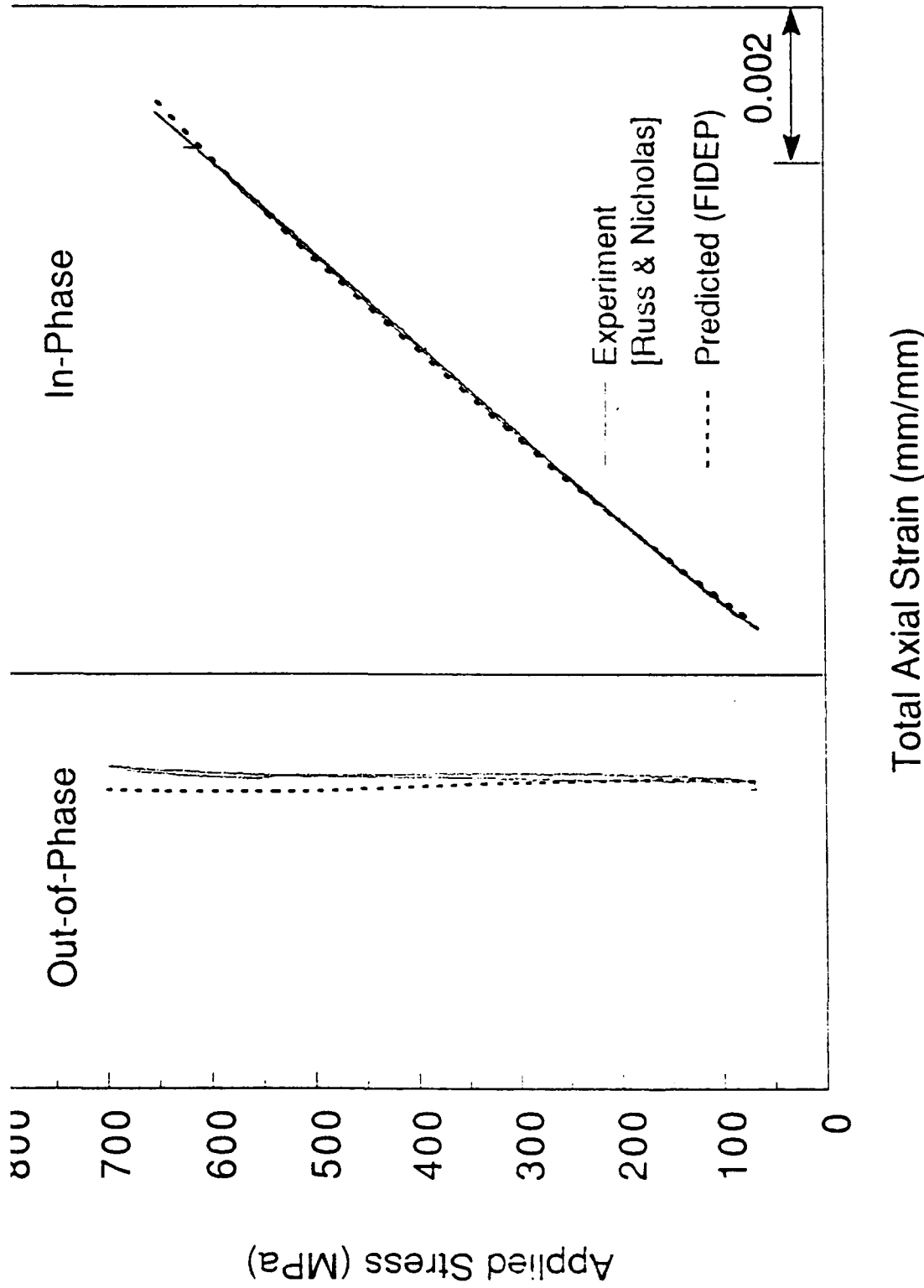


Fig. 4.2.2.4-5 Comparison of predicted load-displacement traces after two cycles and experimental load-displacement traces after several hundred cycles for SCS-6/Ti-24-11 composite.

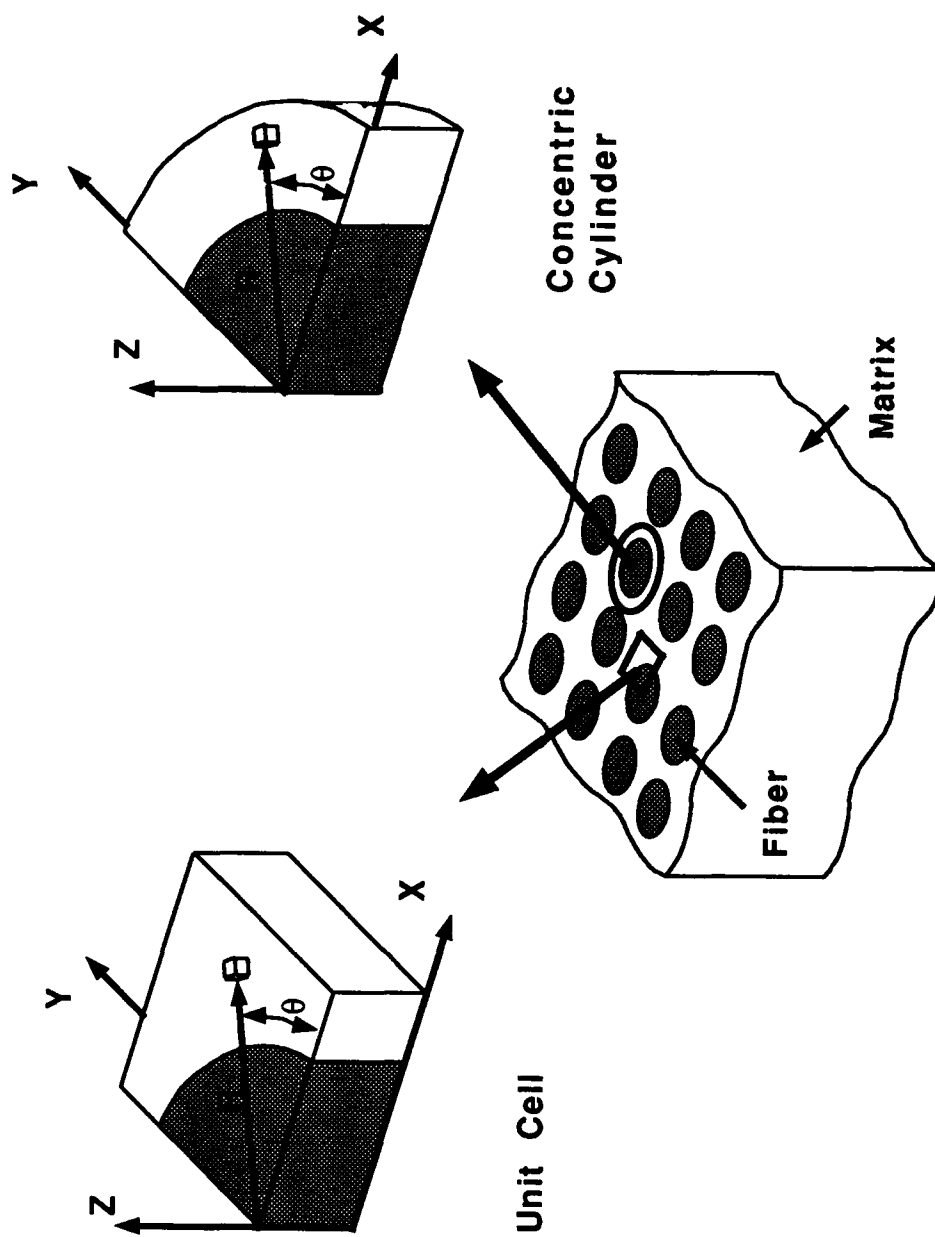


Fig. 4.3.1-1 Concentric cylinder and unit cell representation of MMCs.

(axial/radial) plane with axisymmetric elements, while the unit cell model was constructed with three dimensional solid elements. The degree of freedom in the axial-direction (z-direction) was restricted to give uniform axial strain state throughout the fiber and the matrix. The unit cell model had additional constraints to satisfy geometric symmetry conditions.

Many of the metal matrix materials considered exhibited temperature dependent material behavior, as illustrated by the unidirectional stress-strain response of a typical temperature dependent material, Ti-24Al-11Nb [Titanium Aluminide Composites], in Fig. 4.3.1-2. The properties of elastic modulus, the initial yield strength, and plastic hardening rate were temperature dependent. All the results presented in this section (4.3) except for those in Section 4.3.4.3 were based on the matrix properties illustrated in Fig. 4.3.1-2 and fiber properties listed in Table 4.2.2-1.

A finite element code incorporating temperature dependent effects was required for a realistic description of these materials. After considering the capabilities of widely available finite element codes (NASTRAN, COSMOS, ADINA...), implementation of temperature dependent behavior [Bushnell; Hunsaker et al.] into an in-house code, MAGNA [Brockman], was more cost effective than obtaining, learning, and modifying a new finite element package. As a result, special user-supplied subroutines were written and implemented into MAGNA's 8 or 9 noded axisymmetric and the 16 noded three-dimensional solid elements.

Another advantage for choosing MAGNA was that it also contained special contact elements used to model complex fiber/matrix interfaces. These elements allowed frictionless sliding between the matrix and the fiber. These elements transmit compressive loads between the fiber and matrix when in contact, while tensile and shear loads are not transferred.

4.3.2 Results for Thermal Changes

Due to the mismatch of thermal properties between the fiber and the matrix, stress states were induced within a composite subjected to temperature changes. Of interest, was the state of residual stress generated during the materials processing and subsequent cyclic thermal loads. This residual stress state has been found to significantly influence composite mechanical behavior and its failure mechanisms [Adams; Prewo and Kreider; Wismon].

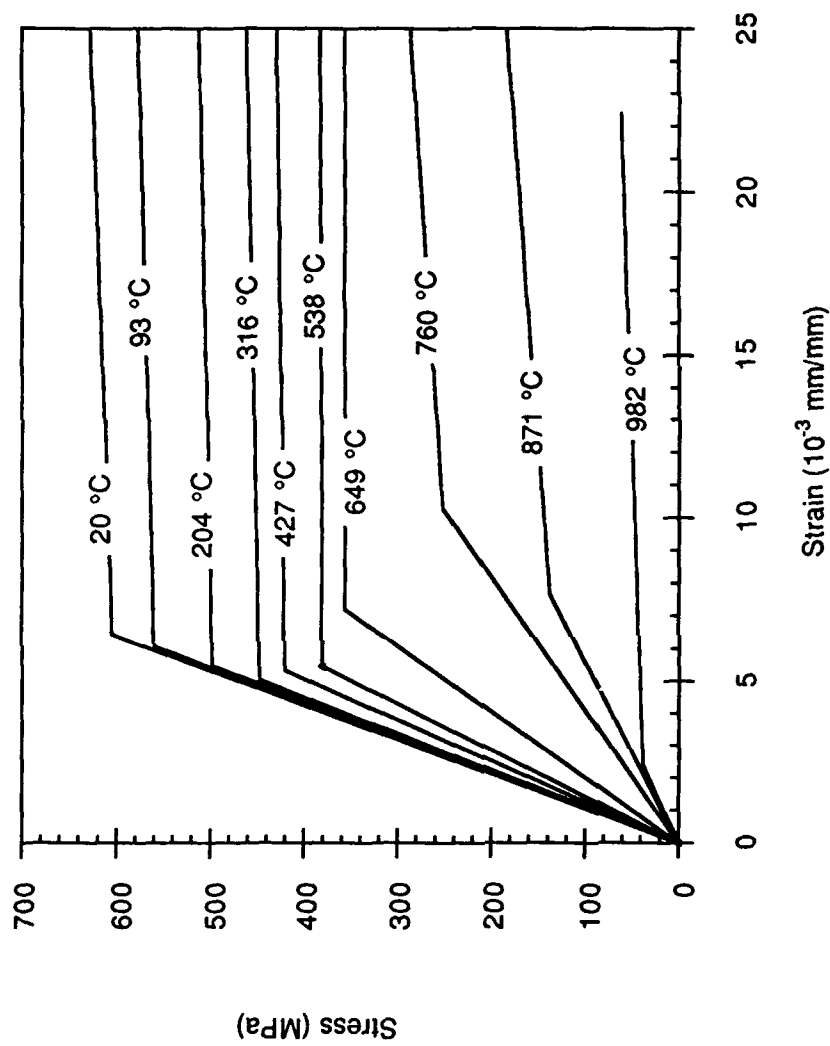


Fig. 4.3.1-2 Temperature dependent material properties of titanium aluminide Ti-24Al-11Nb [Titanium Aluminide Composites].

4.3.2.1 Material Processing

Investigations were conducted to determine the state of residual stress generated during the initial cool down of the composite after the material's consolidation. Composite consolidation consisted of a high isostatic pressure (HIP) at elevated temperatures to guarantee the complete flow of matrix material around the fiber. During the initial cool-down from this consolidation process, residual stresses developed within the composite.

The finite element method was successfully used to predict the residual stress state due to material processing for both the concentric cylinder and unit cell models with a number of composite material systems and with various initial processing temperatures. The analysis considered the composite model with an initial state of zero stress and strain at the elevated temperature processing conditions. Stresses were developed as the model was cooled to room temperature. The resulting residual stress state at room temperature (25°C) of a typical SCS-6 Ti-24Al-11Nb composite for the concentric cylinder geometry is shown in Fig. 4.3.2.1-1. During the cool down, the matrix has shrunk around the fiber, since the matrix generally contracts more rapidly than the fiber for a drop in temperature. The resulting matrix radial stress was compressive, while the hoop and axial stresses were tensile. In the fiber, the radial, hoop and axial stresses are compressive. The region of highest effective stress in the matrix was at the fiber/matrix interface. At the fiber/matrix interface, the effective stress reached the matrix material yield strength at an intermediate temperature during the cooling process illustrated in Fig. 4.3.2.1-2. The effective stress remained at the yield strength for the completion of the cooling cycle.

The state of residual stress was also determined for unit cell models. The unit cell models accounted for equally spaced and unequally spaced fiber arrays in the composite. Equally spaced fibers were represented with a square unit cell and unequally spaced fibers were represented with a rectangular array. The general residual stress state was similar to that found in the concentric cylinder model; however, the stresses were distributed differently. The distributions of process-induced residual effective stress are shown for the square and rectangular cells in the relief plots of Fig. 4.3.2.1-3. The effective stress is plotted as the distance from the X-Y plane, and representative values are labeled. With the unit cell models, variation of the residual stresses around the fiber could be demonstrated. Matrix stress levels above 602 MPa indicate regions where plastic deformation has occurred during the cool-down.

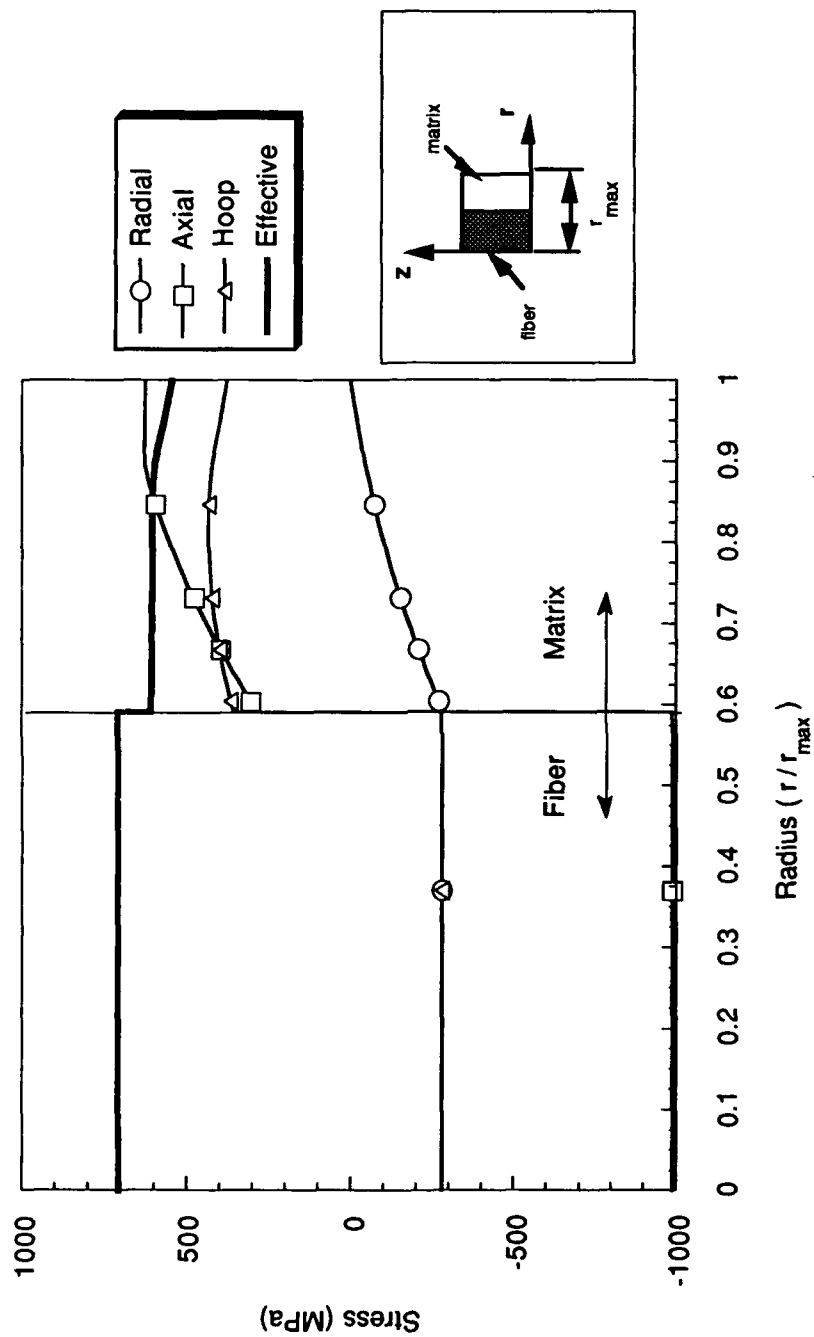


Fig. 4.3.2.1-1 Process induced residual stress prediction at room temperature with concentric cylinder model.

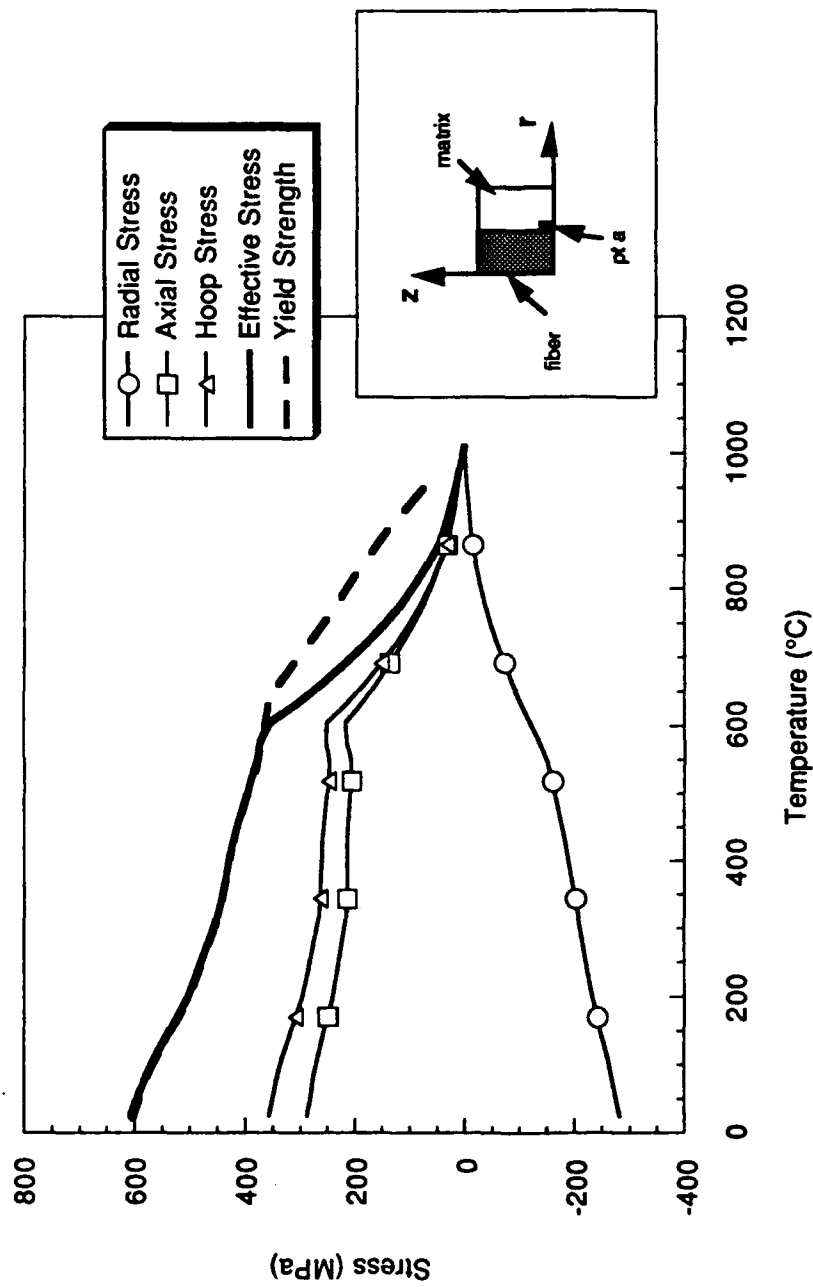
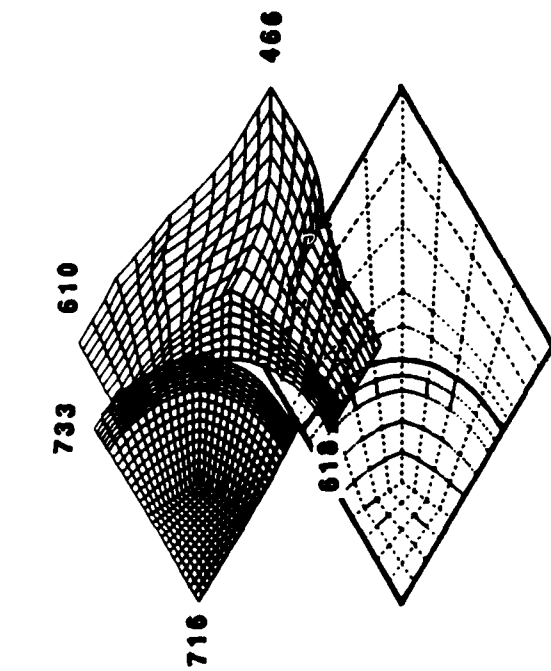
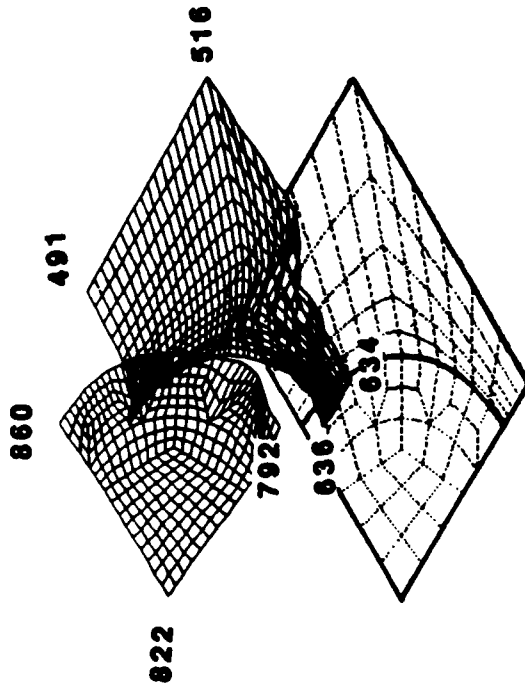
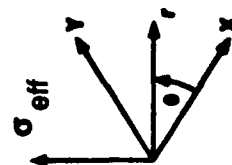


Fig. 4.3.2.1-2 Matrix stress at the fiber/matrix interface (pt a) during cool down from initial processing temperature.



Square



Rectangular

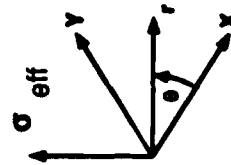


Fig. 4.3.2.1-3 Process induced residual effective stress at room temperature with square and rectangular unit cell models.

4.3.2.2 Cyclic Thermal Conditions

In this analysis, a composite was subjected to a cyclic thermal load with a constant applied axial loading. The response of a concentric cylinder composite model was determined for the same thermal conditions and mechanical load levels used in laboratory experiments [Russ]. The MMC material system was that used in Section 4.3.1.

The applied thermal and mechanical load sequence represented the history of the composite as it was processed and then laboratory tested. The load profile included the initial temperature cool down of the composite from consolidation processing, application of the constant axial load and then the cyclic thermal load. The temperature and applied load profile and the resulting matrix stress history at the fiber/matrix interface are shown in Fig. 4.3.2.2-1. This analysis revealed that matrix plasticity occurred twice during the loading sequence. As a result of plasticity, a simple elastic model would not accurately predict the stress levels produced in the composite. In addition, all the stress components were of significant magnitude to be considered for damage evolution of the titanium matrix material.

4.3.2.3 Combinations of Fiber and Matrix Constituents

Additional cyclic thermal investigations [Munro and Ashbaugh] were conducted to evaluate the performance of a variety of different fiber and matrix composite systems which were subjected to a standard cyclic temperature loading profile. The investigation considered the silicon carbide SCS-6 and boron fibers and a number of matrix systems including gamma titanium aluminides, Inconel 909, Haynes 188, and Lockalloy. The selected materials had a wide variety of elastic moduli, yield strengths and coefficients of thermal expansions. The majority of the matrix materials had temperature dependent behavior. The coefficients of thermal expansion (CTE) of the matrix materials were all higher than the fibers. Both fibers were significantly stiffer and stronger than the matrix materials.

The results revealed that the response of the composite was strongly dependent on the magnitude of the CTE mismatch and matrix yield strength. As expected, larger CTE mismatch generated higher stress and strain levels than the smaller CTE mismatches. If the matrix yield strength was high (Inconel 909), the stress levels in the matrix and the fibers were significantly higher than with a low yield strength material (Haynes 188). Matrix materials with sufficiently low yield strength developed plastic deformation during the initial consolidation cool down of the

Cyclic Thermal Loading

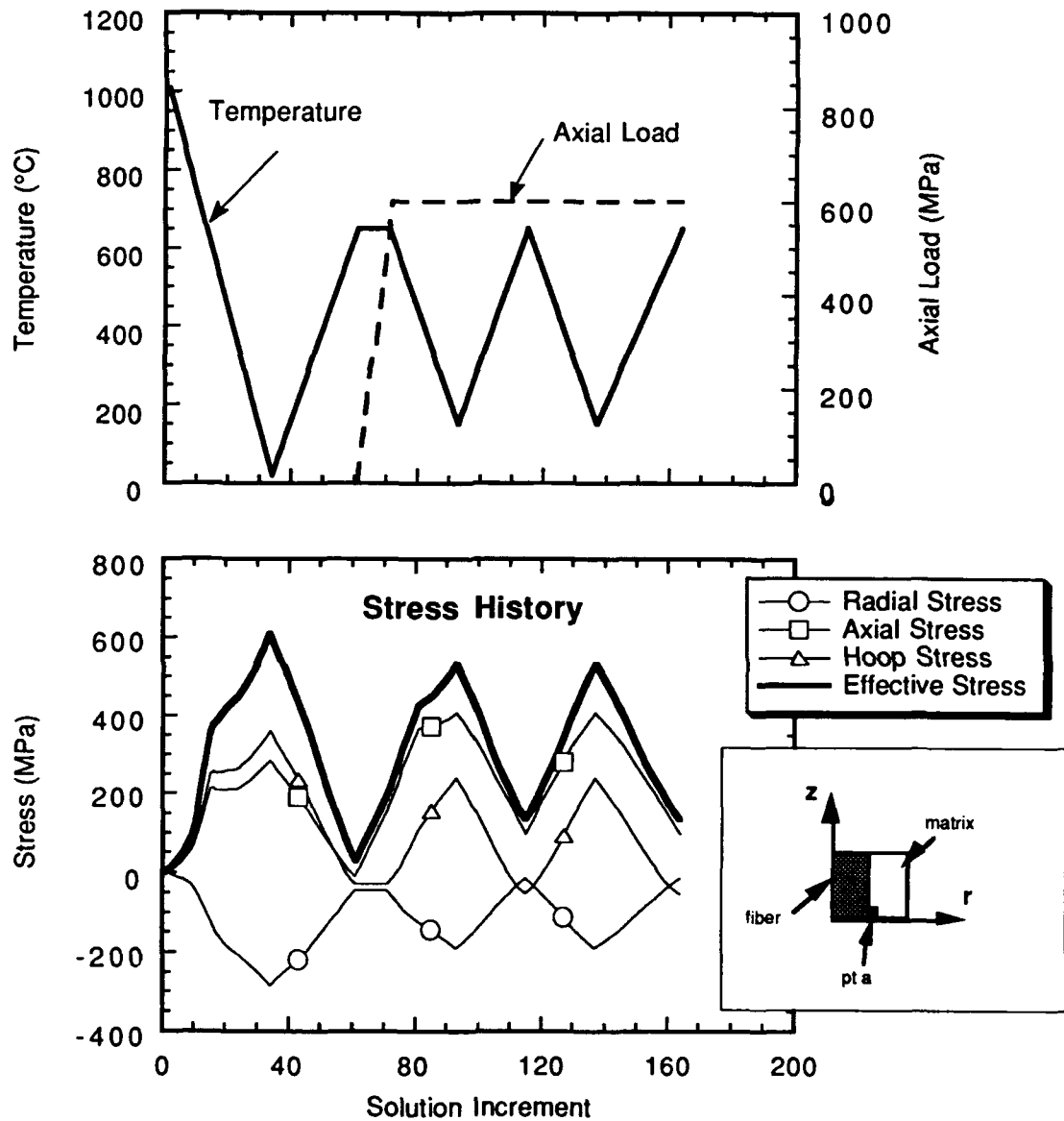


Fig. 4.3.2.2-1 Cyclic thermal with constant axial stress loading and associated matrix stress history at fiber/matrix interface (pt a).

composite. Reversed cyclic plasticity during cyclic thermal loads occurred when the yield strength at elevated temperatures was sufficiently low.

4.3.3 Results for Axial Loads and Thermal Changes

In addition to changing thermal conditions, MMC materials will be exposed to cyclic mechanical loads. Composite response has been determined for the concentric cylinder geometry subjected to mechanical loads for a number of simultaneous thermal and mechanical load conditions [Kroupa]. Two load cases discussed here are cyclic axial loads and thermo mechanical fatigue loads.

4.3.3.1 Cyclic Mechanical Loads

The response of a concentric cylinder composite model was determined for the same thermal conditions and mechanical load levels used in laboratory experiments [Russ]. The MMC composite material system was the same as that described in Section 4.3.1. The load profile included the initial temperature cool down of the composite from consolidation processing, reheating of the composite to an elevated temperature and then, application of the cyclic axial load. The applied load profile and the resulting matrix stress history at the fiber/matrix interface are shown in Fig. 4.3.3.1-1. This analysis revealed that matrix plasticity only occurred during consolidation processing and the remainder of the analysis was in elastic conditions. The axial stress was the only stress component to change with the cyclic axial load, since the Poisson's ratios of the fiber and matrix were the same. The stress levels and ranges were significantly lower than the cyclic thermal load case, as the fiber carried much of the load and the reheating of the composite reduced the initial residual stress state.

4.3.3.2 Thermomechanical Fatigue

The previous analyses considered the responses of the composite to either changing thermal conditions or mechanical cyclic loading conditions. The target of this research was to determine the response of these materials when subjected to simultaneous changes in thermal and mechanical loads. Numerous thermomechanical fatigue experimental investigations on this and similar composite materials had noted the different failure modes with phase and levels of thermal conditions and mechanical loading [Gabb et. al.; Majumdar and Newaz; Russ et al.]. Some combinations of loading conditions resulted in failure of the fiber, while other combinations

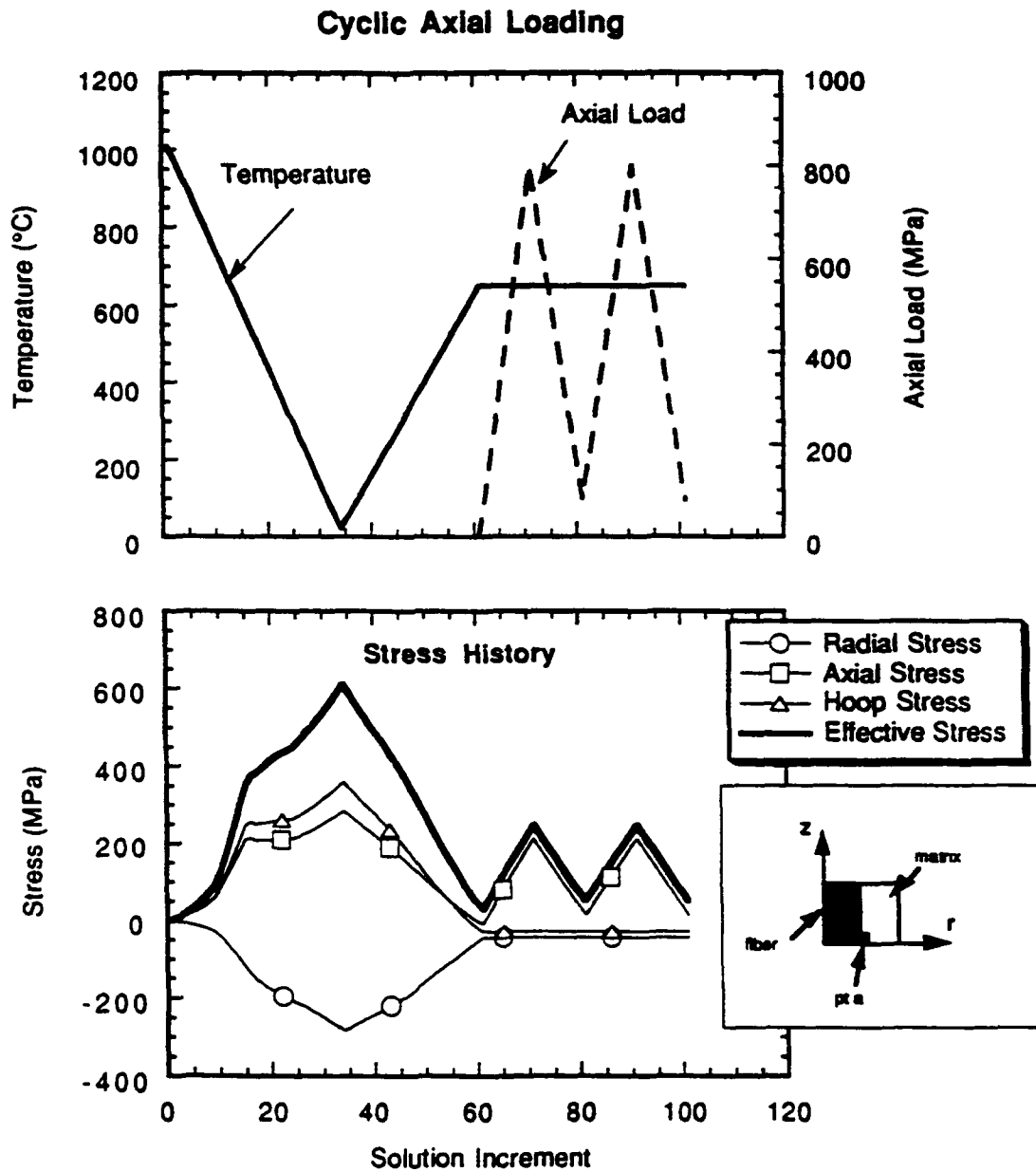


Fig. 4.3.3.1-1 Cyclic axial stress with constant thermal loading and associated matrix stress history at fiber/matrix interface (pt a).

resulted in failure of the matrix material. Various investigations have been conducted to determine the distribution of stresses within the composite to support these experimental findings.

Analyses were completed for the stress distributions within a SCS-6/Ti-24Al-11Nb composite for in-phase and out-of-phase loading. The two thermal and mechanical load profiles and the resulting average axial stress history are shown for in-phase loading in Fig 4.3.3.2-1 and out-of-phase loading in Fig. 4.3.3.2-2. For this composite material system and loading conditions, the stress range of the fiber was larger for the in-phase case than the out-of-phase case. Thus, one might expect a more fiber dominated failure for the in-phase TMF loading. The opposite was true for the out-of-phase case as the stress range in the matrix was significantly larger in the out-of-phase loading than in the in-phase loading. Thus, one might expect a more matrix dominated failure in the out-of-phase case.

4.3.4 Results for Transverse Loading

In many applications, MMCs were being designed in cross-ply layups of unidirectional laminates. The use of these cross-ply layups was limited due to the unidirectional laminate's inherent low transverse strength. Experimentally, the transverse response of a unidirectional composite has been found to be dependent on a number of parameters, including: matrix yield strength, fiber/matrix bond strength and residual stress state [Adams; Prewo and Kreider; Wismon]. Since the effects of these parameters on the composite response are difficult to quantify experimentally, numerical investigations were conducted to determine the effects of the residual stresses and the fiber/matrix bond condition on the transverse response.

Two fiber/matrix interface models were considered -- a perfectly bonded interface and a frictionless sliding interface. The room temperature transverse response was determined in the absence and presence of process induced residual stresses to isolate the effects of residual stresses on the behavior. Additional investigations were conducted to predict the transverse behavior of a unidirectional MMC composite at room and elevated temperatures. The information obtained from this numerical investigation enhanced our understanding of the interaction of residual stress, matrix yield strength, and matrix/fiber separation during transverse loading. This improved understanding of the composite was an aid in the design of future experimental investigations.

In-Phase TMF Loading

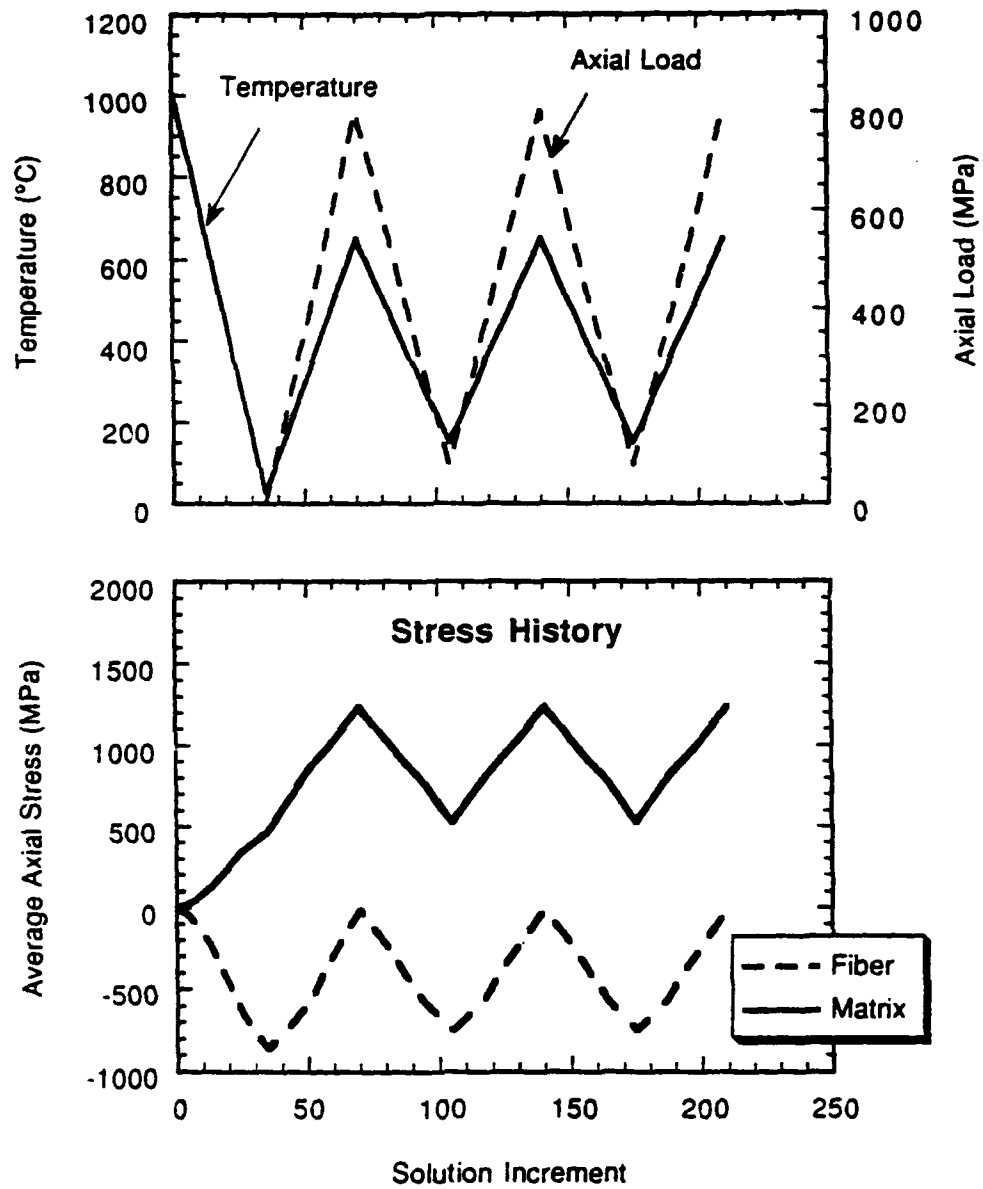


Fig. 4.3.3.2-1 In-phase TMF loading and associated axial stress history in fiber and matrix.

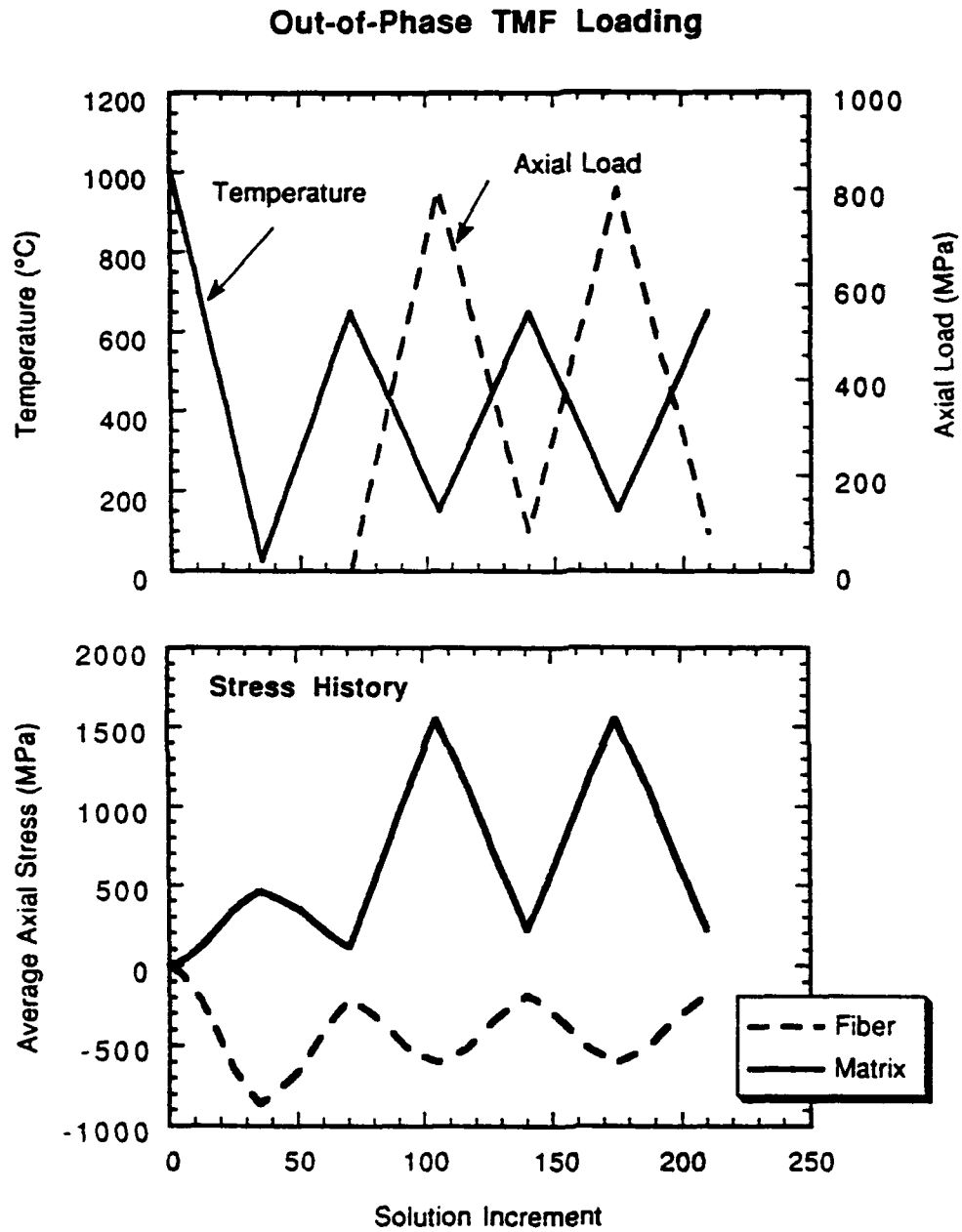


Fig. 4.3.3.2-2 Out-of-phase TMF loading and associated axial stress history in fiber and matrix.

4.3.4.1 Perfect Interface Bond

The perfect interface condition was considered an extreme case of a high strength bond between the matrix and the fiber. The perfect interface condition assumed no separation or sliding (continuous stresses and displacements) between the fiber and the matrix. A square unit cell representation of a unidirectional composite, described in Section 4.3.1, was assumed.

The transverse response, shown in Fig. 4.3.4.1-1, was determined in the presence and absence of processed-induced residual stress to isolate the effects of these residual stresses on the transverse response. The process induced residual stress state had a slight effect on the transverse response. The difference in the transverse behavior was due to the redistribution of stresses due to the presence of residual stresses, as illustrated in Fig. 4.3.4.1-2. Without the residual stress state, the application of transverse loading developed a high hydrostatic pressure within the composite which restricted plastic deformation of the matrix material to Region A under a significantly high applied stress level of 600 MPa. Since the fiber's high stiffness restricted internal strains of the composite, the aggregation strain was concentrated in a highly strained region in the matrix.

In the transversely loaded unit cell with the residual stresses, the application of the loading reduced the compressive radial stress which developed in Region A during processing. Plastic deformation occurred in Region B, which had an initially high residual hoop stress.

4.3.4.2 Frictionless Sliding Interface

A frictionless sliding interface was considered as the worst case situation for an imperfect fiber/matrix interface bond. The frictionless sliding interface condition was satisfied with the special contact element available within MAGNA. The contact element transmitted compressive loads between the fiber and matrix when in contact, but would not transfer tensile or shear loads.

The transverse response was determined for the same SCS-6 and Ti-24Al-11Nb unidirectional composite and square unit cell geometry as in the previous section. The transverse response was determined in the presence and absence of processed-induced residual stress and was compared to the perfectly bonded fiber/matrix interface case in Fig. 4.3.4.2-1. The aggregate transverse stress and stiffness with the frictionless sliding fiber/matrix interface were significantly lower than with the perfect bonded interface. The frictionless contact elements did not transfer

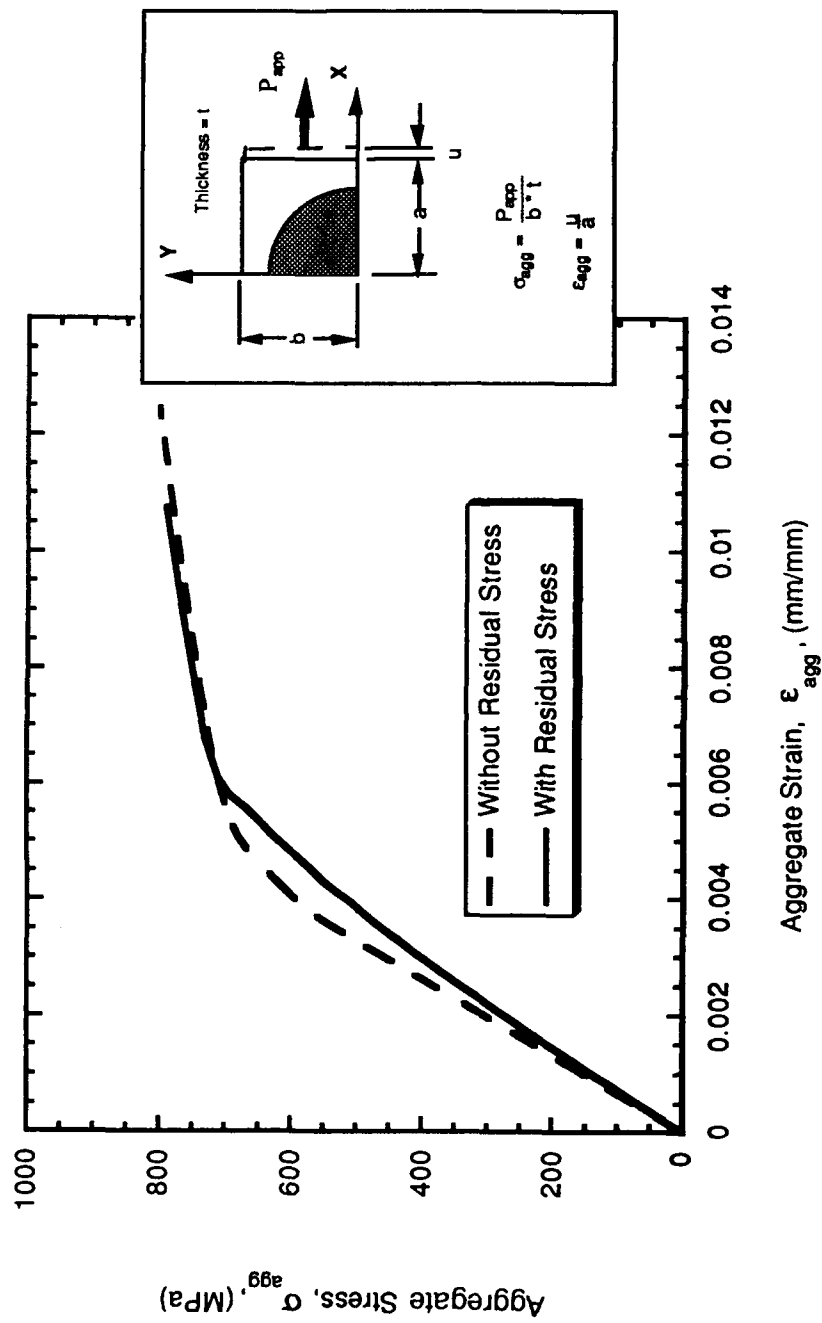


Fig. 4.3.4.1-1 Transverse response with a perfectly bonded fiber/matrix interface.

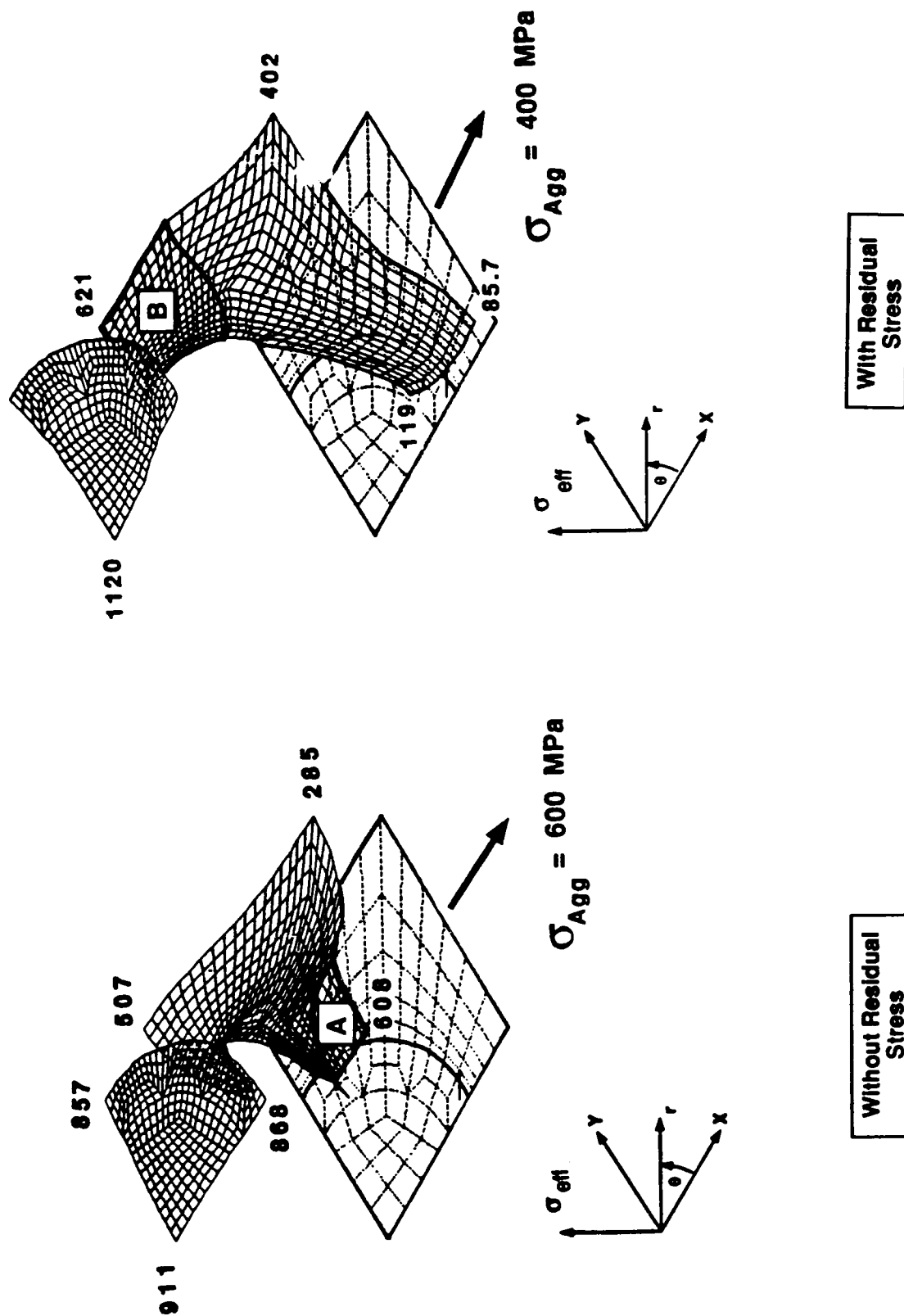


Fig. 4.3.4.1-2 Effective stress state of square unit cell with perfectly bonded fiber/matrix interface with application of transverse load (stress in MPa).

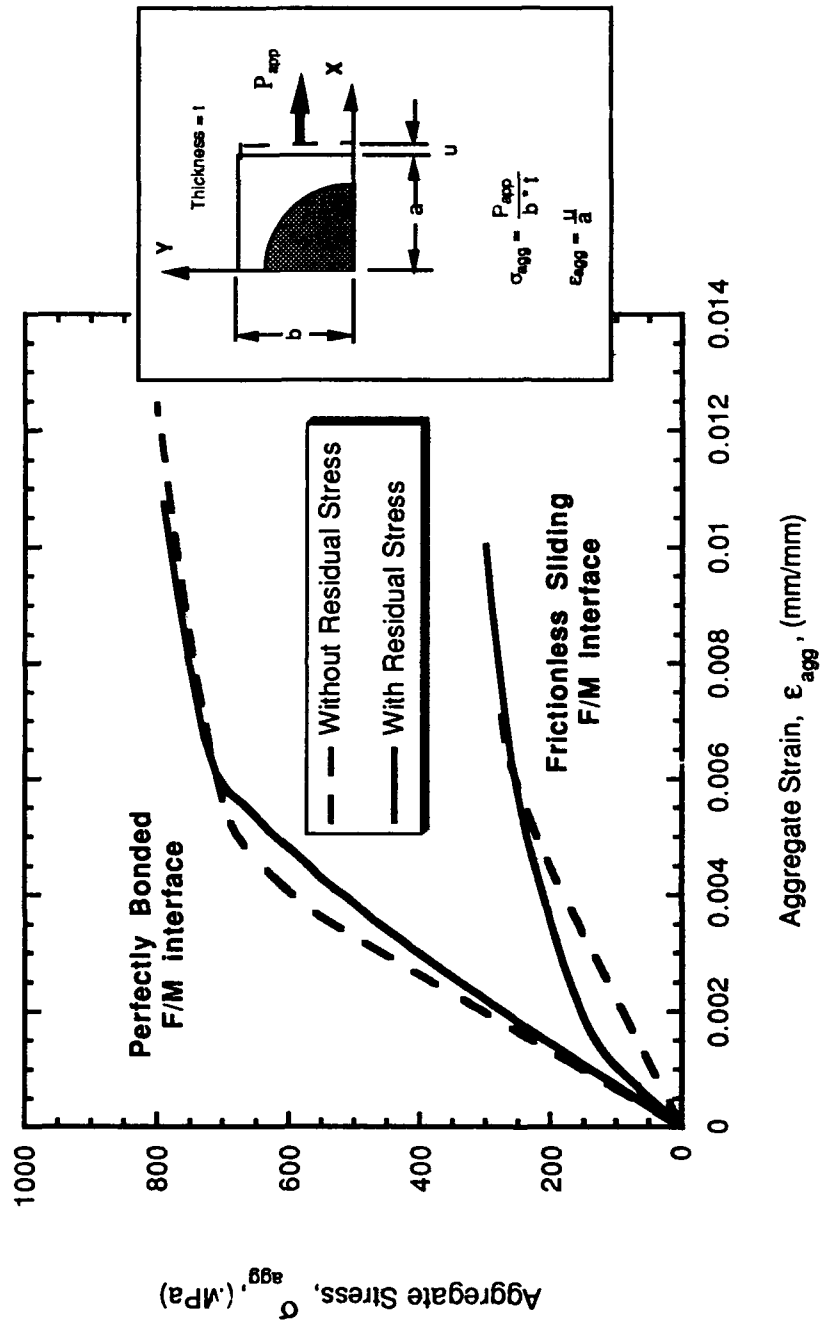


Fig. 4.3.4.2-1 Transverse response with a perfectly bonded and frictionless sliding fiber/matrix interface.

the tensile load previously carried by the perfect fiber/matrix interface. Separation of the matrix from the fiber also enhanced matrix plasticity as a state of hydrostatic pressures never developed within the unit cell.

The residual stress state had a significant effect on the initial modulus of the transverse response. Inspection of effective stress at a transverse load level of 250 MPa revealed a similar stress distribution with or without residual stress states, as illustrated in Fig. 4.3.4.2-2. Initial matrix plastic deformation occurred in Region B for both residual stress cases; however, the size of the matrix yielded regions was not the same. The initially high residual hoop stress resulting from processing promoted yielding of the matrix. The higher transverse modulus for the residual stress state was due to the delay in matrix/fiber separation which occurred when the aggregation stress overcame the matrix's compressive radial stress on the fiber.

4.3.4.3 Transverse Response at Room and Elevated Temperatures

Previous experiments [Gambone] on this composite system only reported the transverse response with little information of the material's failure behavior. The numerical investigation was used to predict possible failure behavior and to aid in the design of additional transverse loaded experiments on the composite.

Extensive efforts were made to characterize the properties of the SCS-6 silicon carbide fiber and the Ti-24Al-11Nb titanium aluminide components of the MMC composite. The thermal coefficients of expansion (see Section 5.1.1.2) and tensile response behavior (see Section 4.2.2) were determined from titanium aluminide matrix material which was cross rolled into foils, layed-up and processed at elevated temperatures in the same manner as the composite. The matrix material of this investigation was processed differently than the material used in the previous sections. The unit cell aspect ratio of 1.4, b/a in inset of Fig. 4.3.4.3-1, was obtained from measurements of composite cross-sections.

The transverse responses resulting from perfect and frictionless interfaces and presence and absence of residual stresses were determined at room and elevated temperatures and then compared to the experimental results. A better fit to experimental results was obtained when residual stresses were present and a frictionless sliding model characterized the fiber/matrix interface. The transverse stiffness and stress response, illustrated in Fig. 4.3.4.3-1, were reduced with increasing temperatures. The increase in temperature also created more inelastic aggregate

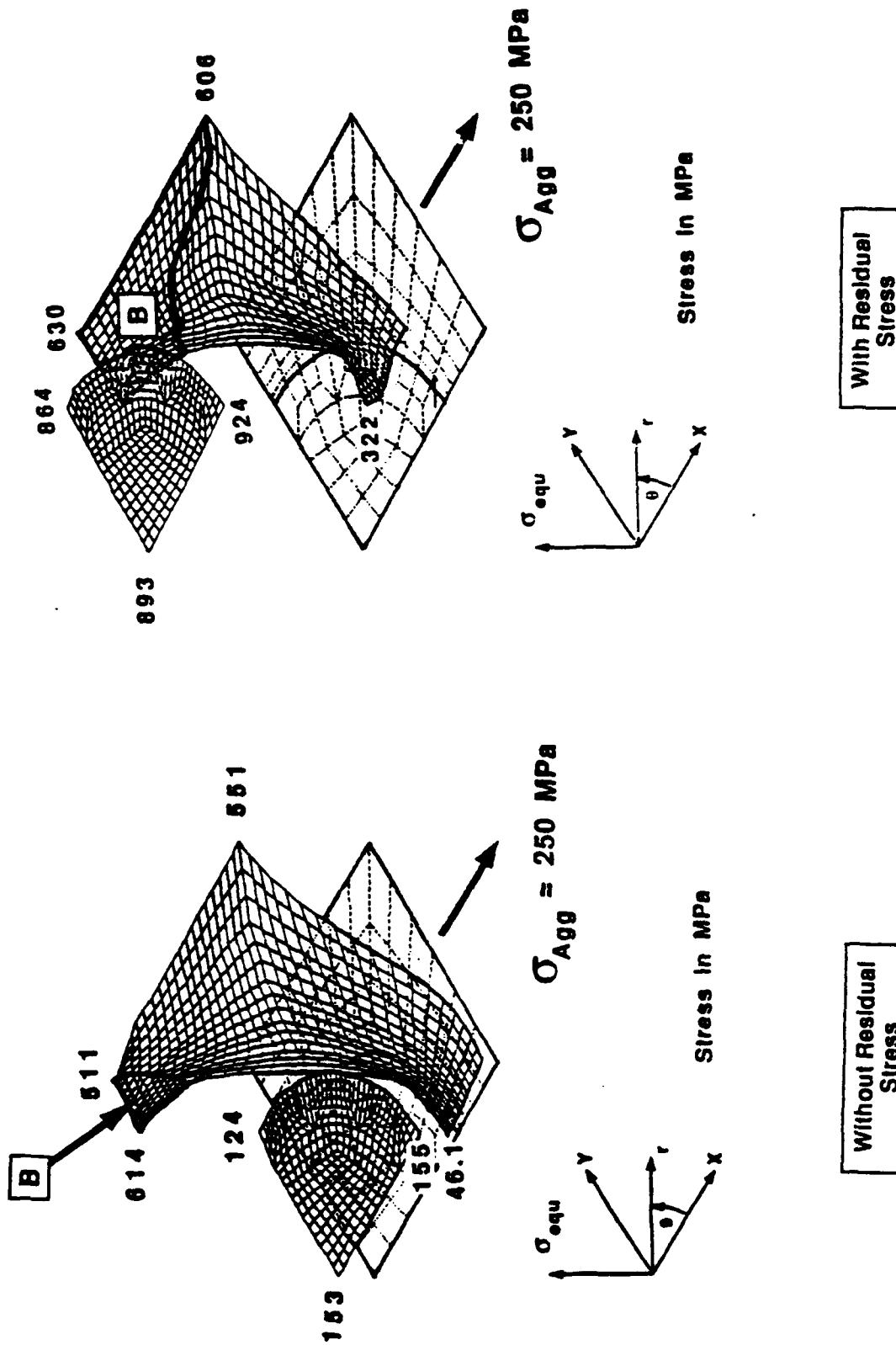


Fig. 4.3.4.2-2 Equivalent stress state of square unit cell with frictionless sliding fiber/matrix interface with application of transverse load (stress in MPa).

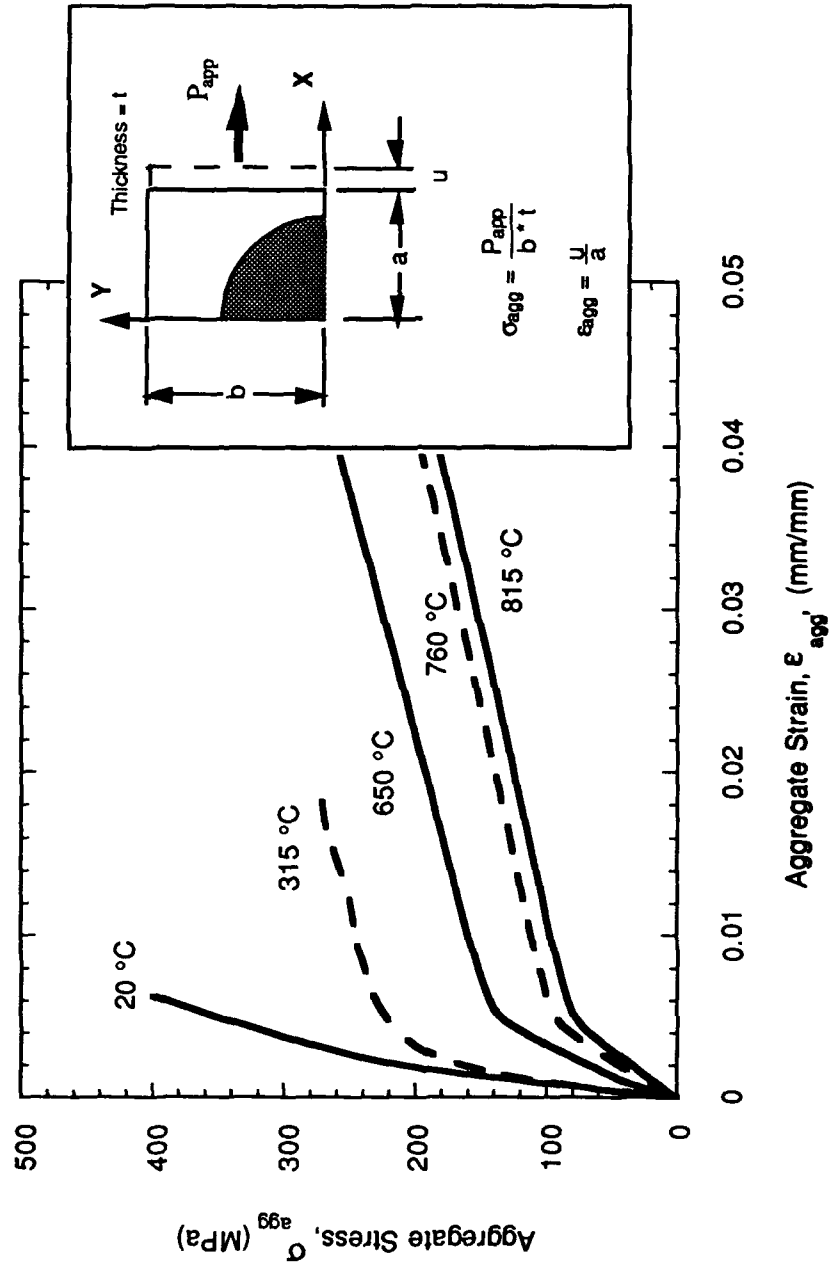


Fig. 4.3.4.3-1 Transverse response at room and elevated temperature with a sliding fiber/matrix interface and residual stress.

strains than observed at lower temperatures. The analytical results correlated well with the experimentally determined response at lower temperature levels, but significant deviations occurred at elevated temperatures. More details of the analysis and the results have been reported [Kroupa et al.].

4.4 Elasticity Results for Cracked Geometries

The following analytical results were generated to aid the interpretation of laboratory data and to support the development of automated test techniques. Linear elastic response and homogeneous isotropic material were assumed.

4.4.1 Center Cracked Panel, M(T)

Even though wide range solutions for stress intensity factors, K , and some selected displacements have been presented in handbooks, accurate results for K and displacements were not readily available for the specially gripped M(T) specimen described in ASTM E647-91, Standard Test Method for Measurement of Fatigue Crack Growth Rates.

Selected K and displacement results for three loading conditions are presented in the next subsection section. Semiempirical relationships for crack length as a function of centerline compliance are given in the second subsection. In the third subsection a closure model for the M(T) specimen is discussed.

4.4.1.1 K and Displacement Values for Selected Boundary Conditions

The stress intensity factors and the displacements along the centerline of an M(T) specimen were determined using a boundary force method and a finite element method. Since the results from the boundary force method were considered to be accurate to better than 1% [Tan et al.], the results from a finite element code were compared to the boundary force results to gain confidence in the code for application to other problems.

Three different loading conditions at the specimen ends, shown with specimen dimensions in Fig. 4.4.1.1-1, were considered -- clamped, uniform displacement and uniform stress. The presence of shear stress and the corresponding lateral displacement constraint at the ends were the differences between the clamped condition and the uniform displacement conditions with no shear stress.

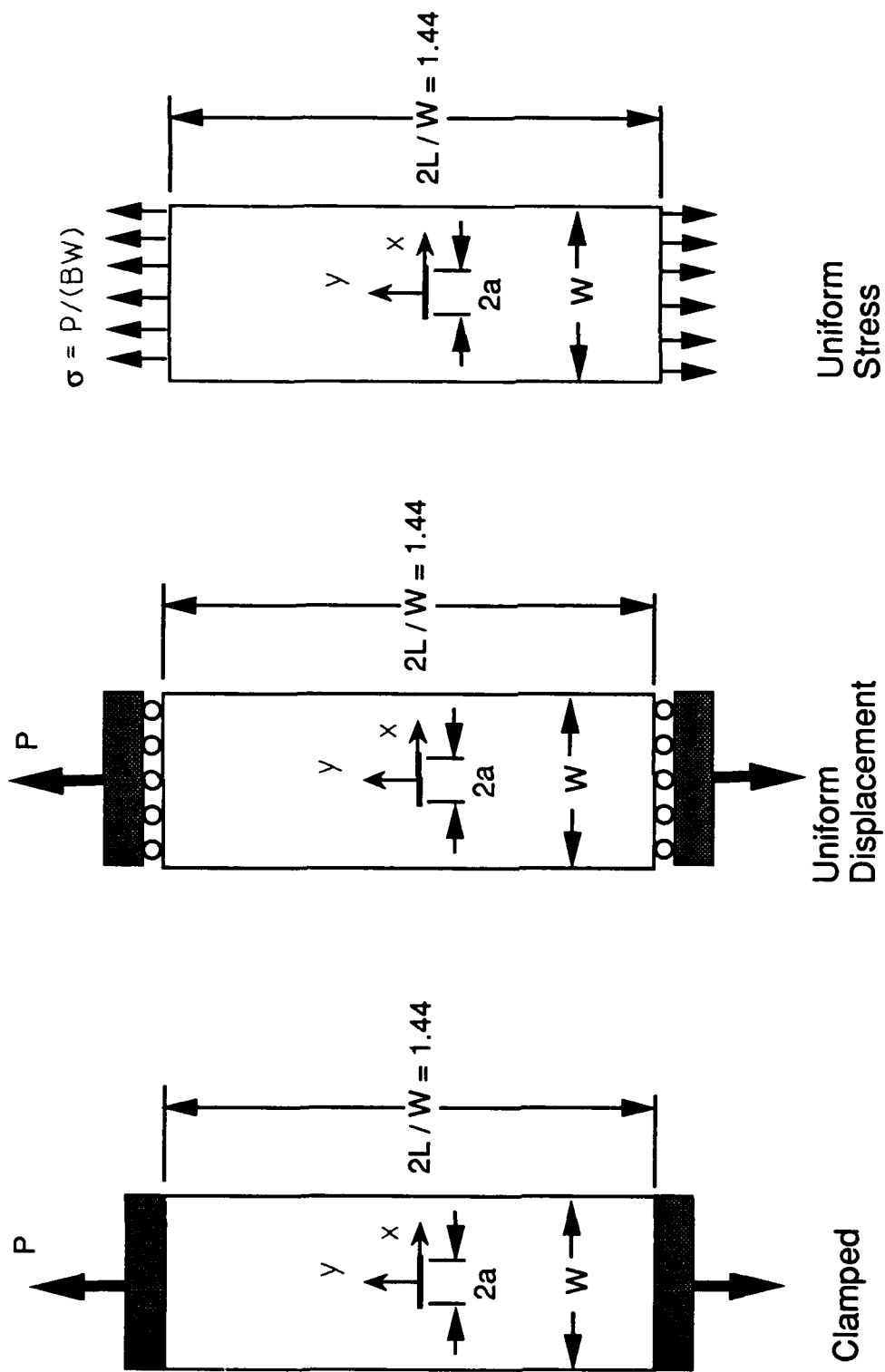


Fig. 4.4.1.1-1 Geometry and load conditions for short M(T) specimen.

The stress intensity factor and centerline displacements, v , given in Table 4.4.1.1-1 for the three loading boundary conditions were determined for a selected crack length. In Table 4.4.1.1-1, the nondimensional displacement values, $2EBv/P$ where E is modulus, B is thickness, and P is load, were determined between points on the specimen centerline a distance, y , above and below the crack. The short crack length was chosen to emphasize the influence of the boundary conditions.

Except for the far-field displacements at $2y/W=1.0$ in the uniform stress loading case, the centerline displacements for all three loadings were within 2.0 percent of each other. The stress intensity values for the three loading were within 2.3 percent of the value 0.575 computed from the accepted equation in ASTM E647-91. The clamped load case displacements and stress

Table 4.4.1.1-1

Centerline Displacements and Stress Intensity Factors for M(T) Specimen
with $L/W = 0.72$ and $2a/W = 0.2$

Nondimensional Centerline Displacements $2EBv/P$ $2y/W$	Clamped	Uniform Displacement	Uniform Stress	Clamped [Tan and Newman]
0.0	0.420	0.410	0.412	0.42
0.2	0.464	0.452	0.455	0.465
0.5	0.654	0.638	0.643	0.655
0.8	0.916	0.898	0.906	0.918
1.0	1.098	1.084	1.525	1.10
	Clamped [Present study]	Uniform Displacement	Uniform Stress	Clamped [Tan and Newman]
Nondimensional Stress Intensity Factor ($K \cdot B \cdot \sqrt{W/P}$)	0.576	0.562	0.565	0.588

intensity factor from the boundary force method and the finite element code used in this investigation compared favorably.

4.4.1.2 Singularity Simulation

During the evaluation of the stress intensity factors for the center cracked panel, an investigation was conducted to determine the effects of finite element meshing on the resulting stress intensity factor. The investigation considered the effects of 1) quarter point singularity elements, 2) singularity element size, 3) singularity element aspect ratio and 4) total number of nodes on the resulting stress intensity factors. The uniform stress loaded M(T) with $L/W = 0.72$ as illustrated in Fig. 4.4.1.1-1 was the basic geometry and a wide number of meshes were generated to determine the meshing effects on the resulting stress intensity factors.

Use of the quarter point singularity element significantly improved the characterization of the singular behavior near the crack tip. Other meshing effects, such as singularity element size, singularity element aspect ratio and total number of nodes gave inconclusive results, as the variations in stress intensity factors were within 1% of an assumed accurate value and beyond the accuracy of the finite element method. These results followed the trends discussed in the literature [Munu; Barsoum; Saouma and Schuremmer] on the effects of finite element meshing on stress intensity factor and the $1/\sqrt{r}$ singularity.

4.4.1.3 Crack Length versus Compliance

Various nonvisual techniques can be used to determine crack length in test specimens. In this report the specimen geometry of interest was the M(T) which is a recommended specimen for fatigue crack growth rate evaluation in ASTM E 647-91. The nonvisual technique, which was considered, was based on the relationship between linear elastic compliance of the specimen and the crack length.

Two types of grips which influence the loading conditions were suggested in E 647-91 for this specimen -- pin loaded and clamped. The load distribution for the two types of grips and for a third hypothetical uniform stress condition are illustrated in Fig. 4.4.1.3-1. The minimum ratios of length to width were 1.5 and 0.72 for the pin loaded and clamped specimens, respectively. As the ratio of length to width for either of the specimens increased, the loading condition approached the uniform stress condition which is represented by the other configuration with a length-to-width ratio of 2.0, shown in Fig. 4.4.1.3-1.

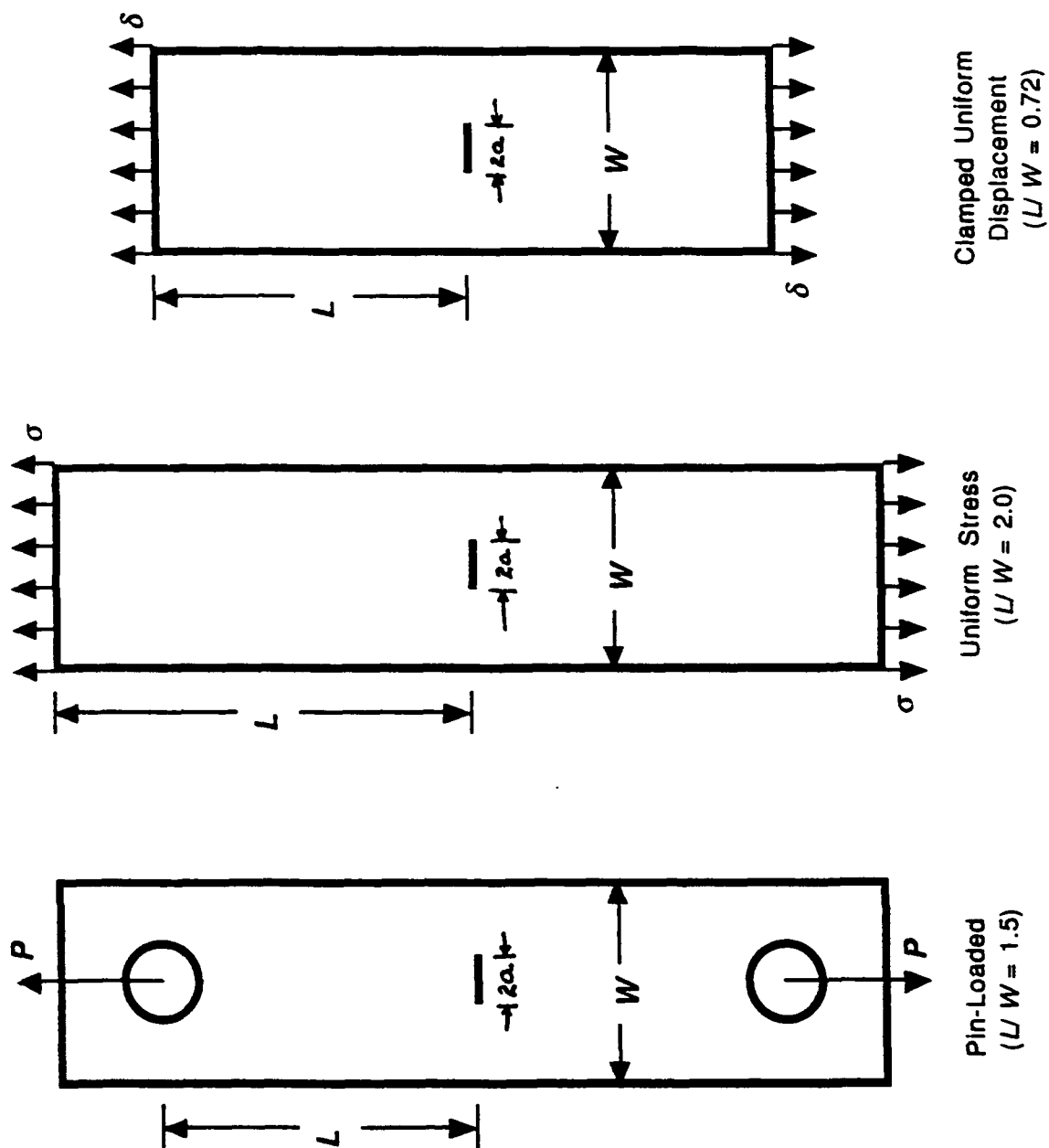


Fig. 4.4.1.3-1 Models of laboratory test specimens.

The compliance for the M(T) specimen is the inverse of the slope of the linear portion of the tensile load vs displacement behavior where the displacement is measured between two points located on the centerline of the specimen and equidistant, y , from the middle of the crack.

In an earlier effort [Ashbaugh], an expression for crack length as a function of compliance and distance between points of displacement measurement was obtained by fitting data which were generated from numerical solutions to appropriate models of the M(T) specimen. Subsequently, sufficient results [Newman; Tan and Newman; Tan et al.] have indicated that the crack length dependence on compliance was significantly different among the three specific specimen configurations. Thus, the following expressions [Ashbaugh and Johnson] were developed:

$$2a/W = 1.06905x + 0.588106x^2 - 1.0185x^3 + 0.361691x^4 ,$$

where:

$$x = 1 - \exp [-((EBC + \eta) (EBC - \eta + C_1\eta + C_2\eta C_3))^{1/2} / 2.141] , \quad (12)$$

$$\eta = 2y / W ,$$

E is an effective modulus of material, B is thickness of specimen, C is the measured compliance, and C_1 , C_2 , C_3 are constants given in Table 4.4.1.3-1.

Table 4.4.1.3-1
Constants for M(T) Compliance

	Pin Loaded	Expressions Uniform Stress	Clamped (Uniform Displ.)
C_1	0.006	0.0	-0.03
C_2	0.0184	0.0	0.013
C_3	3.0	0.0	4.0

4.4.2 Single Edge Cracked Strip, SE(T)

Stress intensity factors for an SE(T) were determined from the finite element analysis to interpret crack growth rate data. The crack growth rate experiments were conducted with pin loaded edge cracked specimens subjected to high frequency loading (>200 Hz). The resulting crack growth rate data obtained from the high frequency loading conditions deviated from data obtained with lower frequency loading.

The loading was introduced into the specimen through rather massive adapters which were clamped to the ends of smooth sided specimens of uniform thickness. The adapters were connected to the loading clevises with pins. Due to the asymmetrical geometry of the SE(T), rotation of the ends of the specimen and, hence, the adapters would normally occur as the load was applied. Since rotational acceleration depends on the square of the frequency, inertial effects of the adapters could modify the apparent pin loading conditions. The inertial resistance of the adapters would create a loading condition which would be similar to a clamped condition with uniform normal displacements. A limited number of strain gages placed on the specimen near the grip adapters indicated that the strain gauge during loading was consistent with the measured load range.

Due to a paucity of information on stress intensity factors for an SE(T) under clamped end conditions, a finite element method was used to compute the stress intensity factors for the uniform displacement loaded SE(T). The high frequency crack growth rate data was then interpreted with the uniform displacement loaded SE(T) stress intensity factors. The resulting crack growth rate data compared favorably to the low frequency data.

4.4.3 Middle Cracked Disk, DM(C)

A schematic of a disk with a middle crack subjected to compressive loading is shown in Fig. 2.3.3.3-1. The available expressions [Atkinson et al.; Yarema et al.] for mode 1 stress intensity factor, K_I , were valid only for $2a/W$ up to 0.60. Tabulated values of K_I were also available up to $2a/W=0.90$ [Tweed et al.]. For the purpose of automated testing, a new expression for K_I was obtained using the results from Tweed et al. for $2a/W \leq 0.9$ and assuming that the limiting behavior at $2a/W = 1.0$ was the same [Tada et al.] as that of the M(T) geometry. The derived expression for K_I is given as:

$$K_I = \frac{P}{B\sqrt{W}} \sqrt{\frac{2}{\pi}} \sqrt{\alpha} F(\alpha) ,$$

where:

$$F(\alpha) = \frac{1 - 0.6188\alpha + 2.6438\alpha^2 - 5.3122\alpha^3 + 6.1794\alpha^4 - 3.0659\alpha^5}{\sqrt{1-\alpha}} , \quad (13)$$

$$\alpha = \frac{2a}{W} ,$$

and a , W , B and P are defined in Fig. 2.3.3.3-1. This equation matched the analytical values of Tweed et al. within 0.5% as shown in Fig. 4.4.3-1. An elastic finite element analysis with quarter-point crack tip elements was conducted to verify the applicability of Eqn. (13) to disks with deep notches. These results correlated well with Eqn. (13) as shown in Fig. 4.4.3.-1 and confirmed its applicability over the range of $0.0 < 2a/W \leq 1.0$.

To conduct compliance based automated fatigue crack growth tests, an expression for the crack length as a function of the crack mouth opening displacement, CMOD at the center of

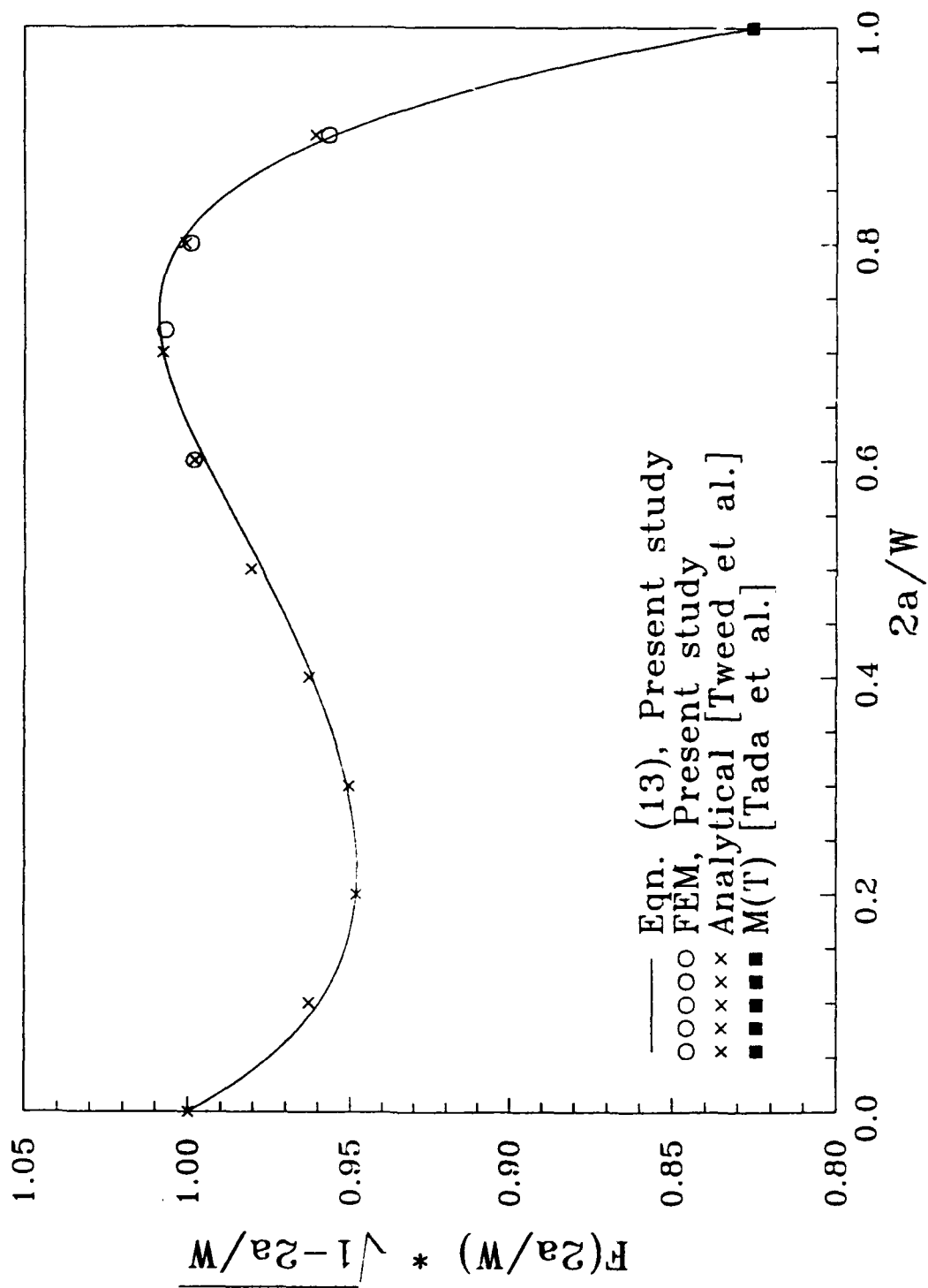


Fig. 4.4.3-1 K_1 geometry correction factor for the DM(C) geometry.

the notch was also required. This expression was derived based on a power series expansion of the crack opening displacement [Fett et al.], and a , W , $CMOD$, B and P are defined in

$$\frac{2a}{W} = (1.8596)S - (1.0572)S^2 - (1.0447)S^3 + (2.2648)S^4 - (1.0195)S^5,$$

where:

(14)

$$S = 1 - \exp\left(-\frac{EBC}{2.141}\right), \quad C = \frac{CMOD}{P},$$

Fig. 2.3.3.3-1, E = Young's modulus, and C = specimen compliance. As shown in Fig. 4.4.3-2, Eqn. (14) correlated well with the finite element results of the present study and that of Ahmad (1988). Hence, Eqn. (14) was also determined to be valid for the range of $0.0 < 2a/W \leq 1.0$. As described in Section 2.3.3.3, elastic verification and fatigue crack growth tests were conducted using aluminum DM(C) specimens over the range $0.40 < 2a/W < 0.80$. During the crack growth, optical crack lengths and the corresponding specimen compliance were measured periodically. As shown in Fig. 4.4.3-2, these data correlated well with the predicted values.

4.4.4 Weight Function Analysis of C(T)

The ASTM standard C(T) shown in Fig. 4.4.4-1, has been used for conducting fracture and fatigue crack growth tests in metals, MMCs, and CMCs. To aid in closure and/or fiber bridging based analysis of these results, a weight function method of analysis [Rice] was applied to the C(T) geometry. If the stress intensity factor, $K_I(a)$, and the related crack opening displacement, $u_r(x,a)$, of a reference load case are known, then K_{WF} can be calculated for an arbitrary stress distribution, $\sigma(x)$, on the crack surfaces:

$$K_{WF} = \frac{E}{K_I} \int_{x=-0.25W}^a \sigma(x) \frac{\partial u_r}{\partial a} dx. \quad (15)$$

Note that $x=0$ corresponds to the load line in Fig. 4.4.4-1.

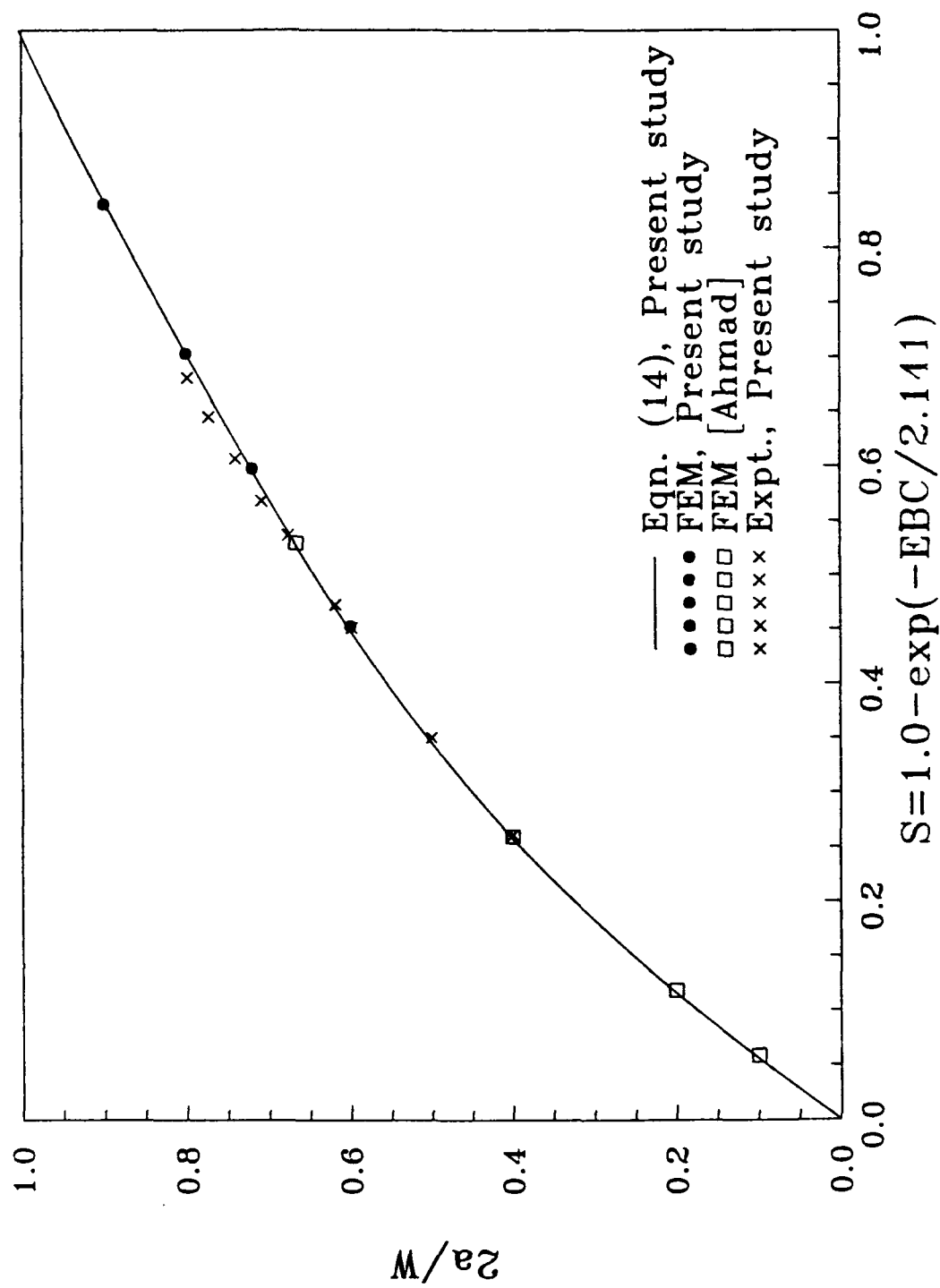


Fig. 4.4.3-2 Crack length versus compliance relationship for the DM(C) geometry.

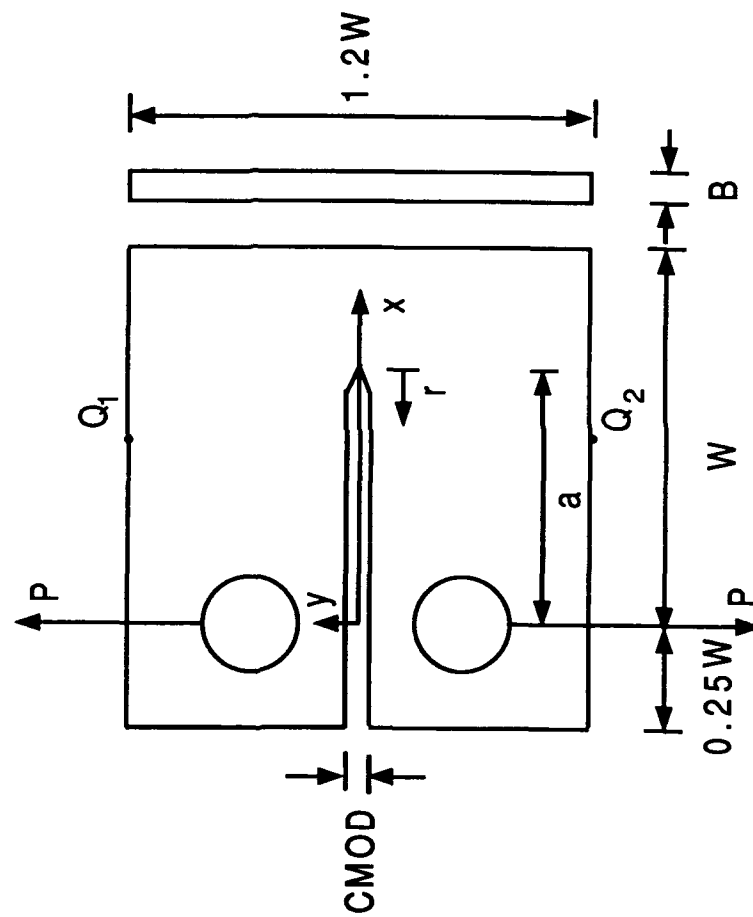


Fig. 4.4.4-1 Schematic of the C(T) geometry.

For the calculations in Eqn. (15), the following expressions [Srawley] for K_I and the crack mouth opening displacement [Saxena and Hudak], CMOD, were used:

$$K_I = K_{ASTM} = \frac{P}{B\sqrt{W}} f\left(\frac{a}{W}\right), \quad (16)$$

and

$$CMOD = \frac{P}{EB} f_1\left(\frac{a}{W}\right), \quad (17)$$

where P , CMOD, a , B and W are defined in Fig. 4.4.4-1, and functions $f(a/W)$ and $f_1(a/W)$ are given in the cited Bibliography. An expression for the crack surface displacement field [Enderle and Ashbaugh], $u_r(x,a)$, corresponding to the reference loading is given by the following equation:

$$\frac{u_r(x,a)}{CMOD} = m_1 + m_2 \frac{r}{W} - \frac{3 m_1}{1 + 2 \exp\left[\frac{12}{\sqrt{2\pi}} \sqrt{\frac{r}{W}} f_2(a/W)\right]}, \quad (18)$$

$$\text{where: } f_2(a/W) = \frac{f(a/W)}{f_1(a/W) m_1},$$

$$m_1 = 0.024 + 0.457\left(\frac{a}{W}\right) - 0.897\left(\frac{a}{W}\right)^2 + 0.445\left(\frac{a}{W}\right)^3, \quad (19)$$

$$m_2 = 2.696 - 4.279\left(\frac{a}{W}\right) + 2.582\left(\frac{a}{W}\right)^2,$$

$r = a - x$ is the distance from the crack tip, and CMOD is given by Eqn. (17). The polynomial expressions for m_1 and m_2 were determined by a least square fit to extensive crack opening displacement results from finite element analysis. Equations (18) and (19) were determined to be applicable over the ranges of $0.25 \leq a/W \leq 0.80$ and $0 \leq r/W \leq a/W + 0.25$ with an accuracy of $\pm 4\%$.

Based on Eqns. (15)-(19), a FORTRAN code was developed to calculate K_{WF} for arbitrary stress distributions. The Chebyshev scheme was used to numerically integrate Eqn. (15). An interpolation scheme was provided to read a tabulated stress distribution obtained from a finite element analysis. Another version was configured to calculate K_{WF} from a polynomial (or any other function) form of stress distribution typically required in a fiber bridging analysis.

For the verification of this code, a linear elastic finite element analysis with 8 node quadrilateral elements was conducted for the standard C(T) geometry with a width $W = 101.6$ mm. The stress distributions along the x-axis in the absence of a crack were determined for two loading cases -- a load, $P=4.45$ kN, applied in the holes at $(x,y) = (0.0, \pm 40.6)$ mm (identical to conventional pin loading) and, in the second case, at $(37.9, \pm 61.0)$ mm. The latter case corresponded to loads applied at points Q_1 and Q_2 in Fig. 4.4.4-1. The finite element stress distributions for the two cases are plotted in Fig. 4.4.4-2. A simple bending analysis neglecting the hole and assuming that the behavior of C(T) was similar to an infinitely long SE(T) yielded an estimate of the stress distribution, also plotted in Fig. 4.4.4-2. Interestingly, the actual stress distribution in the C(T) was significantly different from the bending analysis near the hole but almost identical at the far end of the specimen.

Using the finite element stress distribution for the C(T) loaded in the hole, K_{WF} was calculated for $a/W = 0.25$ to 0.80 and compared to values from Eqn. (16). The percentage error between K_{WF} and those of Eqn. (16) (K_{ASTM}), plotted as a dashed line in Fig. 4.4.4-3, varied between $+8$ to -5% .

To improve the accuracy of the prediction, higher degree polynomial expressions for m_1 and m_2 were determined:

$$m_1 = -0.1352 + 1.9048\left(\frac{a}{W}\right) - 5.5428\left(\frac{a}{W}\right)^2 + 6.7029\left(\frac{a}{W}\right)^3 - 3.0043\left(\frac{a}{W}\right)^4 \quad (20)$$

$$m_2 = 3.9867 - 14.671\left(\frac{a}{W}\right) + 31.5863\left(\frac{a}{W}\right)^2 - 33.6028\left(\frac{a}{W}\right)^3 + 13.7871\left(\frac{a}{W}\right)^4$$

These new equations were then incorporated in the weight function code and the predicted values of K_{WF} were compared with those of Eqn. (16). The error between K_{WF} and K_{ASTM} , shown by the solid line in Fig. 4.4.4-3, improved to $\pm 1.6\%$. Also, using Eqn. (20) instead of Eqn. (19), the

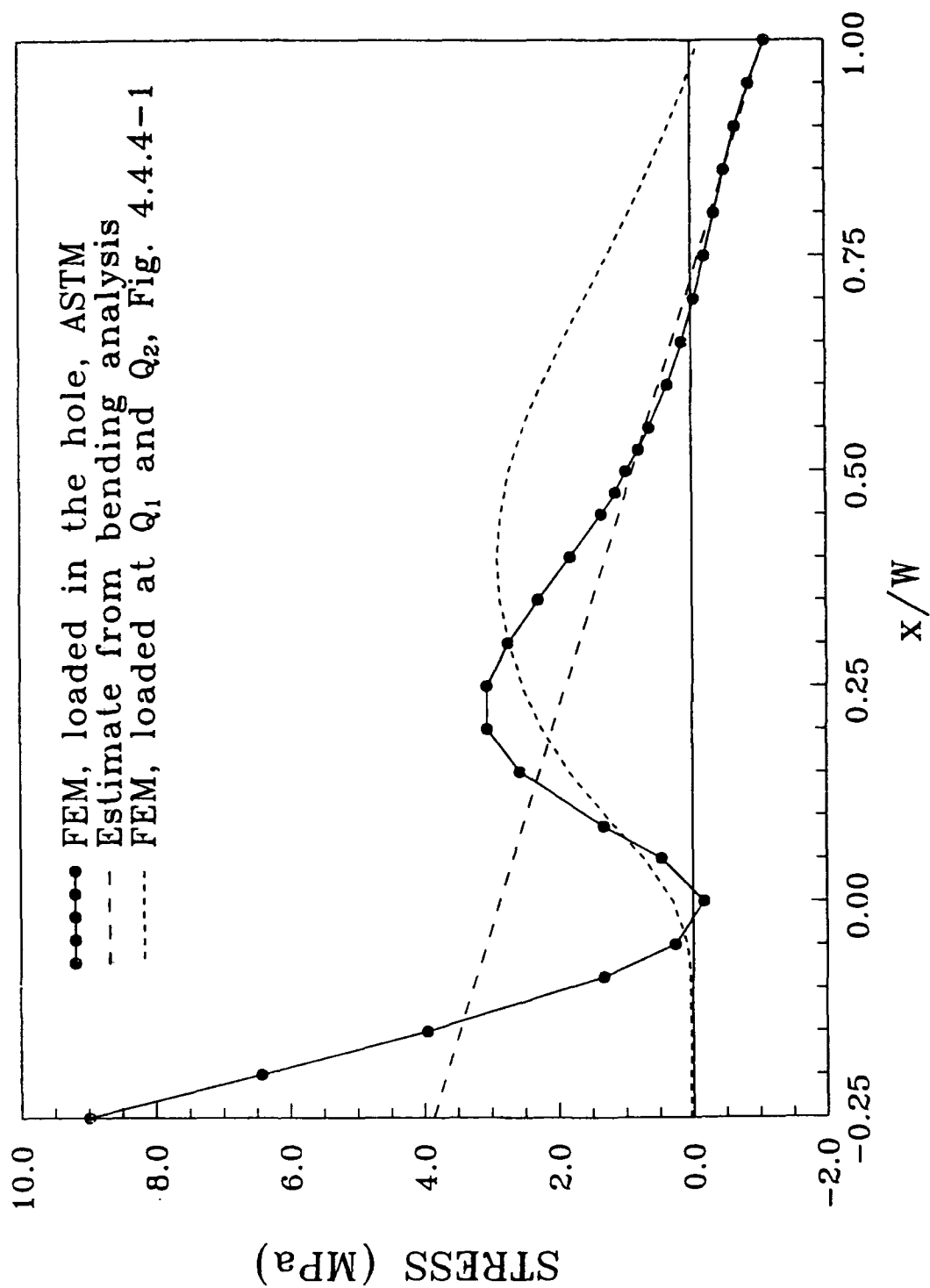


Fig. 4.4.4-2 Stress distribution along the x-axis in an uncracked C(T).

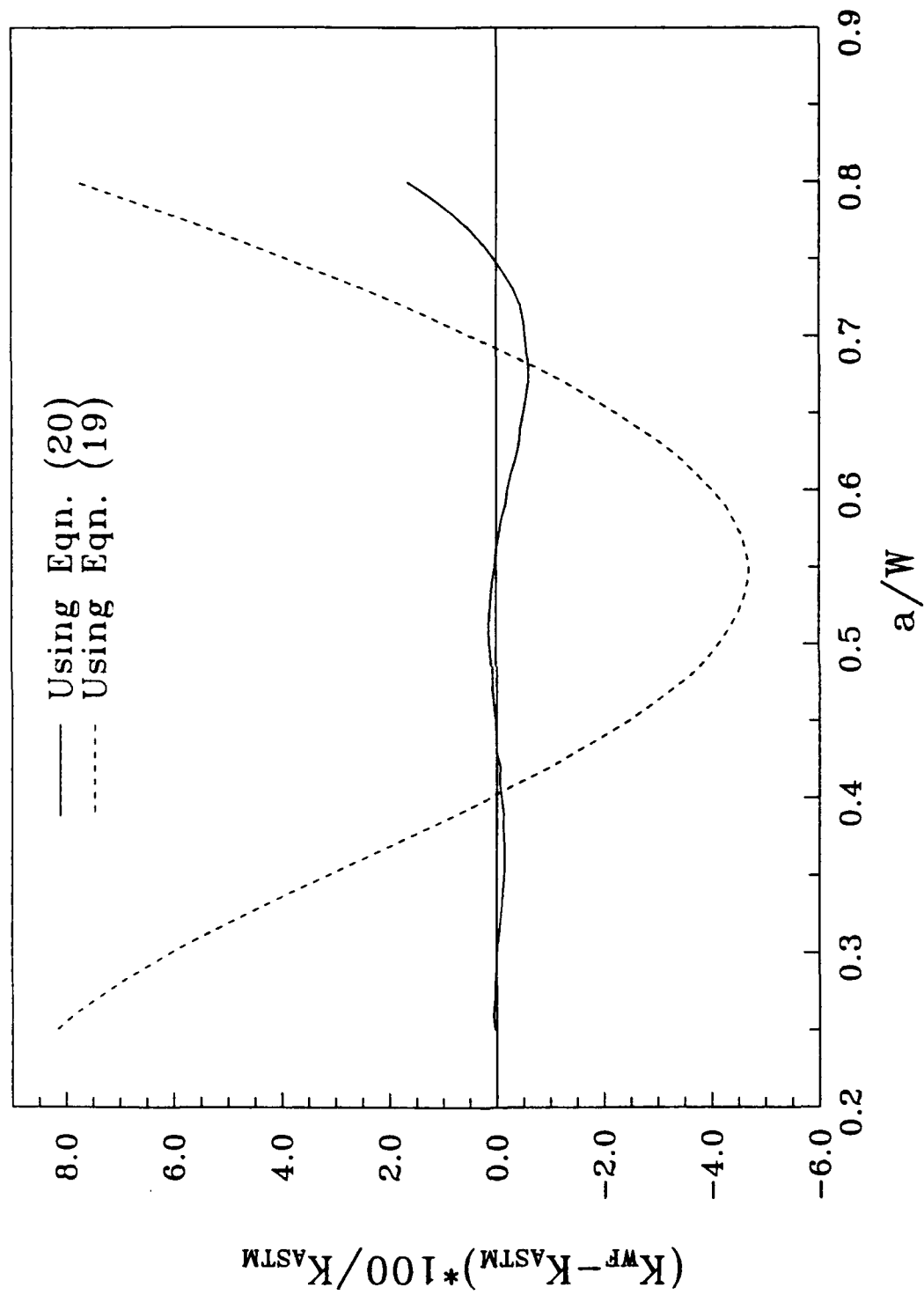


Fig. 4.4.4-3 Error between the weight function method, K_{WF} and ASTM expression, K_{ASTM} .

accuracy of fitting the crack opening displacement data from the finite element analysis improved from $\pm 4\%$ to $\pm 2.6\%$.

For further verification, the second loading case with the stress distribution shown as a dashed line in Fig. 4.4.4-2 was analyzed. The stress intensity values computed with both the finite element code having quarter point singular elements around the crack tip and the weight function method were 2.41 and 2.42 MPa $\sqrt{\text{m}}$, respectively, for $a/W = 0.50$. The close agreement between the two values confirmed the applicability of the weight function method for analyzing cases with arbitrary stress distributions. This method was verified for the ranges $0.25 \leq a/W \leq 0.80$ and $0.0 \leq r/W \leq a/W + 0.25$ and could be used to analyze with confidence the contribution of fiber bridging during fracture and fatigue crack growth in CMCs and MMCs.

4.5 Review of Laminate Analyses

Literature on laminate analysis techniques of high temperature composites was reviewed. The approach used by most authors to laminate analysis was very similar. Initially an incremental load was applied to the composite laminate. Laminated plate theory was then used to compute the stress state in each layer. The layer response was determined from unidirectional micromechanical models or experiments. Finally, the layer stiffnesses were used to compute the new composite stiffness.

Two approaches to micromechanical modeling exist in the literature. The first approach which was more commonly employed was the assumption of constant stress and strain distribution in the phases. This approach was taken with square fiber in square matrix models [Aboudi; Sun et al.; Hopkins and Chamis] and vanishing fiber diameter model [Dvorak and Bahei-El-Din]. Rule of mixture relations were used for the stresses and the strains in these lamina models:

$$\begin{aligned}
\sigma_{ij}^c &= \sigma_{ij}^f = \sigma_{ij}^m, & i, j & \neq 3,3, \\
\sigma_{33}^c &= V_f \sigma_{33}^f + V_m \sigma_{33}^m, \\
\epsilon_{ij}^c &= V_f \epsilon_{ij}^f + V_m \epsilon_{ij}^m, & i, j & \neq 3,3, \\
\epsilon_{33}^c &= \epsilon_{33}^f = \epsilon_{33}^m.
\end{aligned} \tag{21}$$

where c, f and m represent the composite, fiber and matrix, respectively, 3 is the fiber direction, and V_f and V_m are volume fractions of the fiber and matrix, respectively. The second approach accounted for variable stress and strain distributions in the phases and, typically, uses the concentric cylinder model [Barrett and Buesking; Pagano and Tandon]. The analyses of these models are briefly reviewed in the following paragraphs.

A combined micromechanical and macromechanical analysis was developed to investigate the behavior of metal matrix fiber reinforced laminates [Barrett and Buesking; Barrett]. A composite cylinder assemblage with thermoplastic material properties was analyzed at the micromechanical level to determine constituent stresses in the layers. Effective lamina properties were computed using the phase average model. A nonlinear macromechanical analysis was then conducted based on an incremental form of classical lamination theory in which the laminate was loaded by residual stresses, thermal loads and edge stress resultants.

A multidirectional coated continuous fiber composite was analyzed by means of a three phase concentric cylinder model in which the constituents were assumed to be linear elastic materials [Pagano and Tandon]. This model was incorporated into a PC compatible menu driven computer code called NDSANDS. This code can handle different constituent materials, arbitrary fiber orientations and multiaxial loading conditions. It can be used to study the change in effective properties and stress distribution as a result of different input parameters.

A vanishing fiber model was developed where the presence of the fibers was assumed not to affect the transverse stresses [Dvorak and Bahei-El-Din]. The model predicted longitudinal stresses along the fiber when the composite was thermally loaded or mechanically loaded in the fiber direction. The vanishing fiber diameter model was implemented into AGLPLY [Bahei-El-Din]

to predict average stresses in the constituents and in a symmetric composite laminate subjected to thermomechanical loading. The model accounted for thermoplastic properties for the matrix and elastic properties for the fiber.

A model based on a square fiber in a square matrix subcell was developed using first order displacement expansions [Aboudi]. Explicit constitutive relations were used to predict the overall behavior of unidirectional fiber reinforced composites with temperature dependent elastoplastic phases. In the elastic region, effective elastic moduli and coefficients of thermal expansion were given by closed form expressions. In the inelastic region, the unified theory of Bodner-Partom was used to compute inelastic strains. In addition, imperfect bonding was represented by a thin elastic film whose shear stress depended on the relative tangential displacement at the interface and normal bond stress was proportional to the relative normal displacement. This model was implemented into a computer code EPC [Herakovich et al.].

A macromechanical one parameter plastic model was developed for nonlinear stress-strain behavior of laminates [Sun et al.]. Micromechanical modeling used a square fiber in a square matrix and the stresses were computed using a strength of materials approach. The fiber was assumed to be orthotropic linear elastic and the matrix was isotropic elastic and followed a von Mises plasticity surface. Fiber/matrix separation and one-dimensional thermal stress effects were taken into account.

A strength of materials approach for a square fiber in a square matrix model with an interphase was used to predict mechanical and thermal properties of the composite and obtain expressions for the constituent microstresses [Hopkins and Chamis]. These expressions were modified based on uniaxial lamina behavior but did not include Poisson's ratio contributions. The model incorporated thermoviscoplastic nonlinear constitutive relations that consisted of products of terms with unknown exponents which were determined from experimental data. This model was implemented into the code METCAN [Chamis and Hopkins] to be used in conjunction with large structural analysis programs on a mainframe computer.

An elastic laminate analysis code, GENLAN, was written to calculate the strain and stress at a point in a plate based on the laminated plate theory taking into account anisotropy and the layered structure of the plate [Tsai]. GENLAN computes stiffness and strength of unsymmetric hybrid laminates subjected to complex, in-plane loads and bending moments applied to the edge of the plate.

Numerical results for elastic constituent properties, shown in Table 4.5-1, were obtained from the available codes for a temperature change of -517°C. Results from AGLPLY, METCAN and EPC codes were reviewed in detail and compared with a finite element unit cell model consisting of a circular fiber and square matrix [Bigelow et al.]. In addition, AGLPLY and METCAN codes were executed for an independent evaluation. The combined results for fiber and matrix stresses are shown in Table 4.5-2.

Table 4.5-1
Elastic Properties for the Fiber and Matrix and their Volume Fraction in the Composite

	E(GPa)	$\alpha(10^{-6}/^{\circ}\text{C})$	ν	V o l u m e Fraction
Matrix	92.3	9.25	0.36	0.675
Fiber	400	4.86	0.25	0.325

Table 4.5-2
Axial Stresses in the Fiber and Matrix for Thermal Cool Down

Models	Fiber Stress MPa	Matrix Stress MPa
METCAN ^(a)	-180	140
EPC ^(a)	-340	145
AGLPLY ^(a)	-294	142
Finite Element Model ^(a)	-370	170
METCAN ^(b)	-425	140
AGLPLY (SCM) ^(b)	-340	164
Concentric Cylinder Model	-371	178
Rule of Mixtures	-294	142

(a) [Bigelow et al.]. (b) Independent evaluation.

The difference in METCAN results was attributed to a programming mistake in the version used for the literature results. AGLPLY had an option for scaling the values using the self consistent model (SCM) and the results from this option are shown as AGLPLY (SCM). The concentric cylinder model results which were calculated using FIDEP (Section 4.2) were in good

agreement with finite element model results using the square cell model. AGLPLY and rule of mixtures gave identical values for the stresses and were significantly different from the finite element model results.

The laminate properties computed from METCAN, EPC, and AGLPLY [Bigelow, et al.] were found to be in agreement with the finite element unit cell results but the same consistency was not observed in the predicted micromechanical stresses in Table 4.5-2. This discrepancy was attributed to the fact that these codes do not predict a three dimensional stress state or variable stress distribution in the composite.

4.6 Crack Near Interface in 2-D Composite

The elastic problem of a crack normal to a bimaterial interface is addressed in the context of unidirectional fiber composites [Ahmad]. The structure of asymptotic crack-tip stress fields is obtained numerically. The numerical results are then analyzed to formulate criteria for assessing cracking normal to the fiber, interface splitting, and fiber pull-out.

4.7 Fiber Pullout Analysis

The bridging fibers across a crack in a matrix of a composite could significantly lower the stress intensity factor at the crack tip. The amount of bridging fibers across a crack ligament is dependent on many factors. A preliminary investigation of a simple fiber pullout geometry, shown in Fig. 4.7-1, was conducted to enhance our understanding of the pullout phenomenon and of the generation of bridging stress which could influence matrix crack advancement.

The materials for fiber pullout consisted of an SCS-6 fiber in a titanium aluminide matrix with assumed linear elastic material behavior. The length of the debonded region of the matrix from the fiber, "a", was 2.54 mm. The fiber was then far-field loaded with a uniform displacement load of 0.127 mm. A finite element representation of the geometry was created and solved with the MAGNA finite element package [Brockman]. This displacement resulted in an equivalent aggregate stress loading of 13.0 GPa on the fiber. The matrix stress profile along the fiber/matrix interface near the initial debonded regions is shown in Fig. 4.7-2. The solution produced an osculating singularity, but more resolution of the finite element mesh would be required to illustrate the nature and magnitude of the singularity. The stress profile was in general agreement with other known elasticity solutions [Muki and Sternberg; Luk and Keer].

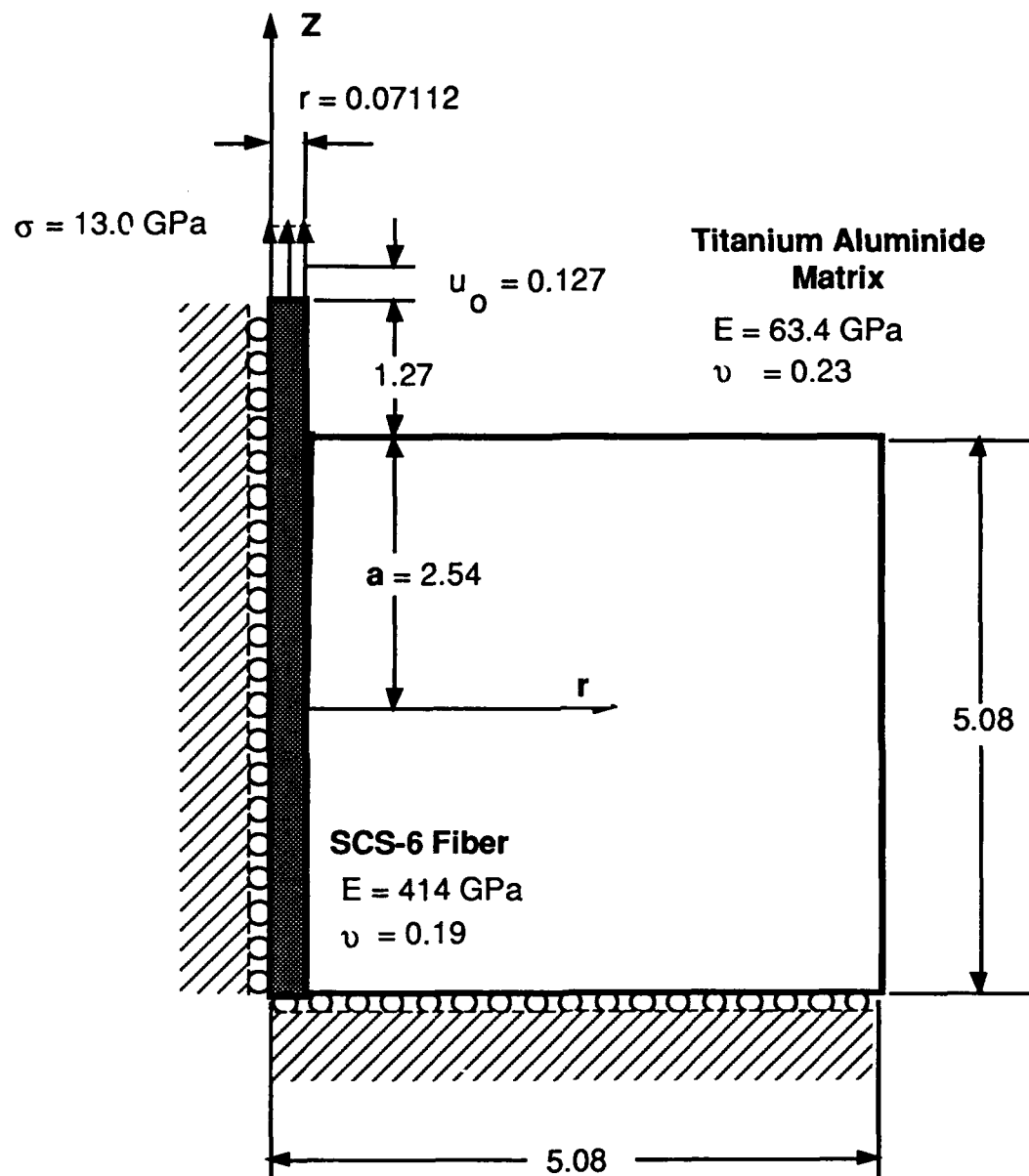


Fig. 4.7-1 Fiber pull-out geometry (dimensions in mm).

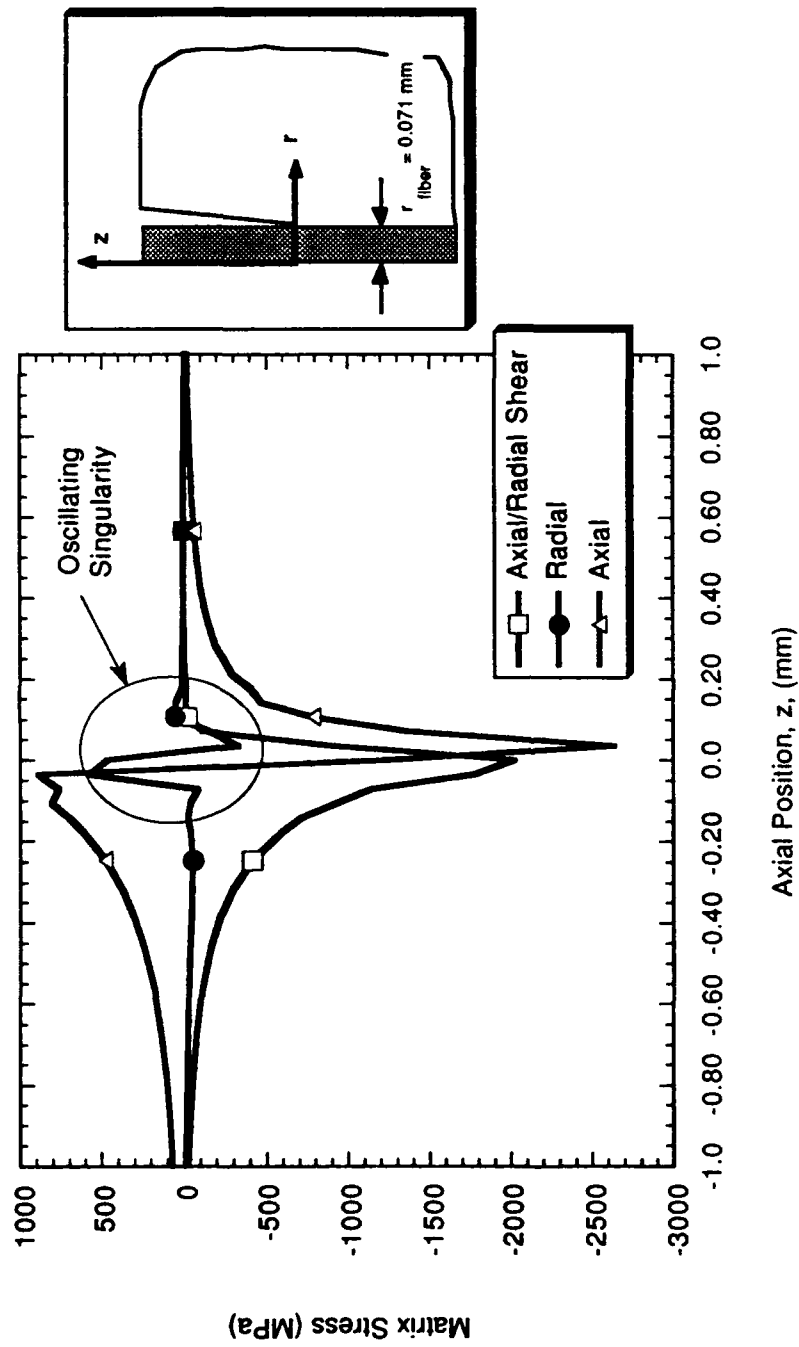


Fig. 4.7-2 Resulting matrix stress profile at fiber/matrix interface near the crack tip.

In a complimentary analysis [Ahmad and Papaspyropoulos], pullout problem with no crack at the interface and with two crack lengths at the interface have been reported using a highly refined mesh in the vicinity of the stress singularities.

4.8 Surface and Embedded Flaws in Unidirectional Composites

Three problems concerning flaws in brittle matrix composites with unidirectional fibers were analyzed. The first problem involved a single internal flaw normal to the fibers and the applied load. The second problem considered a surface flaw again normal to the fibers and the load. Finally, a series of periodic flaws were analyzed in a unidirectional composite.

In the first problem, an analytical model [Dharani and Chai, a] was developed for the determination of displacement and stress distributions in a finite three-dimensional unidirectional composite with broken fibers forming an embedded planar crack, normal to the fibers and the loading. In order to reduce the complexity of the elasticity formulations, some assumptions were made as to the physically significant stresses to be retained; fibers carry the tensile load and the matrix carries only the shear force. These assumptions simplified the partial differential equations into a set of differential-difference equations. The governing equations were solved for various crack configurations as the composite material was subjected to a uniform tensile load along the fiber direction. The results for different shapes of the embedded crack indicated that a crack tended to extend first at the centers of its straight edges and eventually attained circular shape.

The second investigation considered a particular class of unidirectional composites whose matrix and fiber have comparable stiffnesses with internal and surface flaws created during processing and in service. A three-dimensional consistent shear lag model was developed for a stress analysis of a finite three-dimensional composite containing various embedded and surface flaw geometries in a composite subjected to a uniform tensile load along the fiber direction. The governing equations consisted of a set of ordinary coupled differential-difference equations in which the axial and transverse displacements were the unknowns. The displacement and stress fields [Chai and Dharani] were obtained to predict the mode of crack propagation based on a point stress failure criterion.

In a third analysis, a three dimensional unidirectional composite with fibers aligned along the loading direction and containing planar multiple cracks was analyzed for its fracture behavior. The stresses and displacements were determined using a consistent shear lag formulation that

accounts for the load carrying capacity of the matrix in the longitudinal and transverse directions. The cracks were of equal size and are distributed uniformly along the load axis. The change in compliance and energy release rates were obtained as functions of crack size (area) and spacing (crack density). The results [Dharani and Chai, b] indicated that the growth of existing cracks occurred more easily than the formation of new cracks.

4.9 Elastic-Plastic Analysis of Deeply Notched Tensile Specimen

An evaluation of the failure of a notched specimen of niobium-silicide alloy was attempted through a correlation of analytical results and experimental behavior. The finite element analysis was conducted for the annular notch geometry shown in Fig. 4.9-1. An isothermal elastic-plastic model was based on the uniaxial stress-strain response in Fig. 4.9-2. A finite element representation of the notch geometry was created and solved with the MAGNA finite element package [Brockman].

The stress components and possible failure criterion parameters on the notch plane ($z=0$) were computed. The resulting stress distribution for an applied load of 20 ksi and three failure criteria -- maximum normal stress, effective stress (Eqn. (9)) and the maximum shear stress are illustrated in Fig. 4.9-3. A high tensile hydrostatic stress (mean stress) was noted near the root of the notch. Testing of the notched specimens has not been completed for correlation of these analytical results with experimental data.

4.10 Electric Potential Analysis of C(T)

The electric potential method was employed to monitor the crack growth rate in thermo-mechanical fatigue experiments of Inconel-718 compact specimens. To reduce the amount of scatter in the experimental results, great care was taken in the placement of electric potential probes and current source locations. Post experimental inspection of the results revealed significant amounts of scatter in the data. Known parameters, which can account for such scatter, included variations in the placement of current sources and electric potential probe locations [Druce and Booth; Ritter and Ritchie; Klintworth and Webster]. This investigation resolved the extent of these parameter's effects on the measured electric potential. The effect of the nonuniform electric conductivity distribution across the specimen (due to a nonuniform temperature distribution) was also determined.

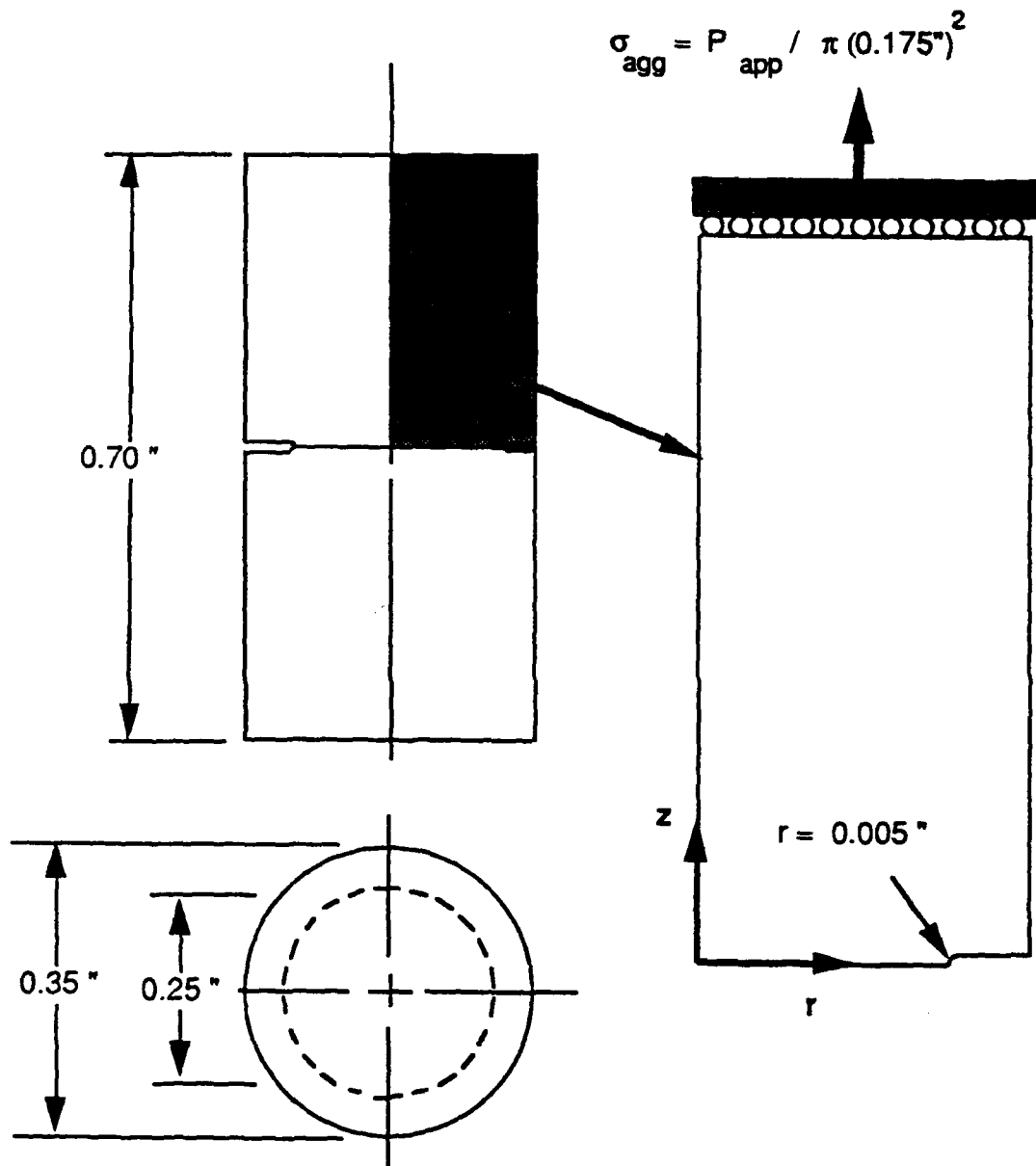


Fig. 4.9-1 Notched tension test specimen.

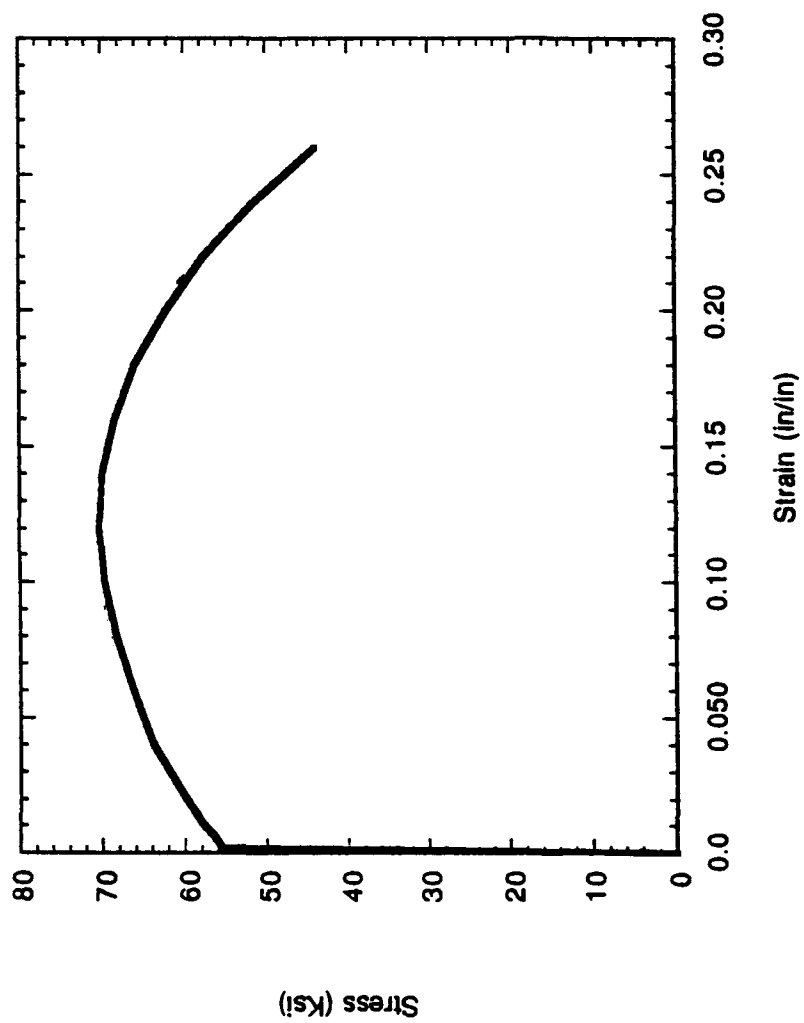


Fig. 4.9-2 Uniaxial stress-strain response of niobium-silicide at room temperature.

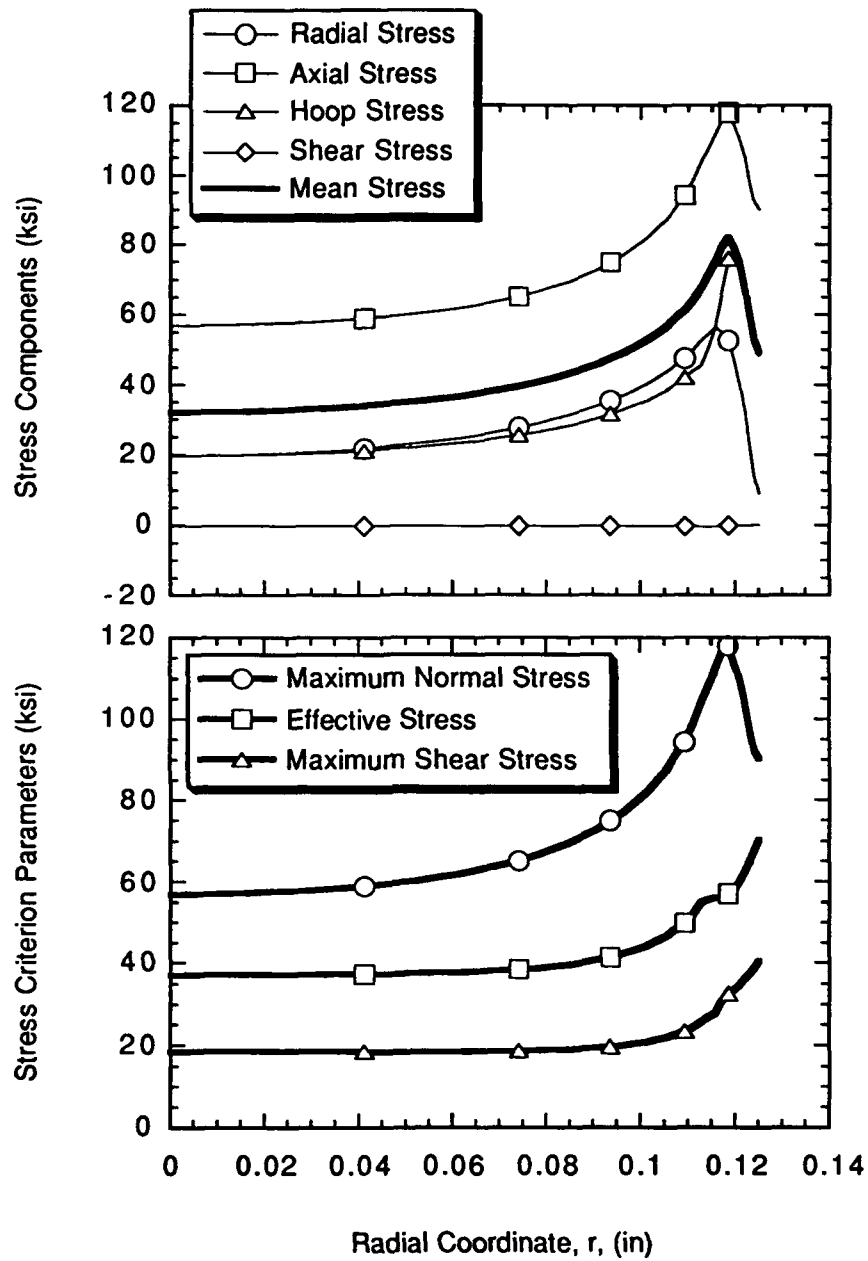


Fig. 4.9-3 Stress profile and failure criterion parameters on notched plane ($z = 0$).

The geometry used in this study was a standard compact specimen, as shown with dimensions in Fig. 4.10-1 and with a thickness, B , of 2.41 mm (0.095 inch). The plus signs, $+$, mark the locations where the electric potential probes monitored the crack growth. A steady current source of ten amps was applied to the specimen at the locations marked with darkened circles.

During five thermomechanical crack growth experiments, the electric potential was measured near the crack tip within a region of uniform heating of 649°C. The electric potential measurements and base-line finite element results versus crack length are plotted in Fig. 4.10-2. To illustrate the effects of the experimental scatter on measured crack length, an electric potential line was drawn from 0.01 and intercepted the calibration curves over a range of 0.41 to 0.44 for a/W . The uncertainty of 0.03 a/W ($\pm 0.015 a/W$) could lead to significant errors in automated crack growth experiments. The base-line finite element analysis was conducted with a uniform conductivity of 758.7 /ohm-mm [Inconel Alloy 718] for the temperature of 649°C. The experimental and the finite element results showed good agreement, indicating a reasonable amount of accuracy in the analytical solution.

From postexperimental measurements of the compact specimens, variations in the location of the electric potential leads and the current sources were determined to be approximately ± 0.7 mm. To determine the effects of these small shifts in the electric potential probe location on the measured electric potential, the electric potential was sampled at five locations; one in the center and four in out-lying points. The probe location shifts of ± 0.7 mm in the X- and Y- directions and the resulting electric potential deviations from the base-line solution are shown in Fig. 4.10-3. The base-line solution was the measured electric potential at the center location. The electric potential deviations were scaled by the base-line electric potential at the corresponding crack length.

A similar investigation was conducted to determine the effects of slight shifts in the current source locations. In this study, the electric potential was sampled at the base-line location of the previous investigation and current source was shifted ± 0.7 mm from its center location. The current source shift location, directions and resulting electric potential deviations from the base-line solution are shown Fig. 4.10-4. The deviations in electric potential between the unshifted and shifted current source are also scaled by the base-line electric potential at the

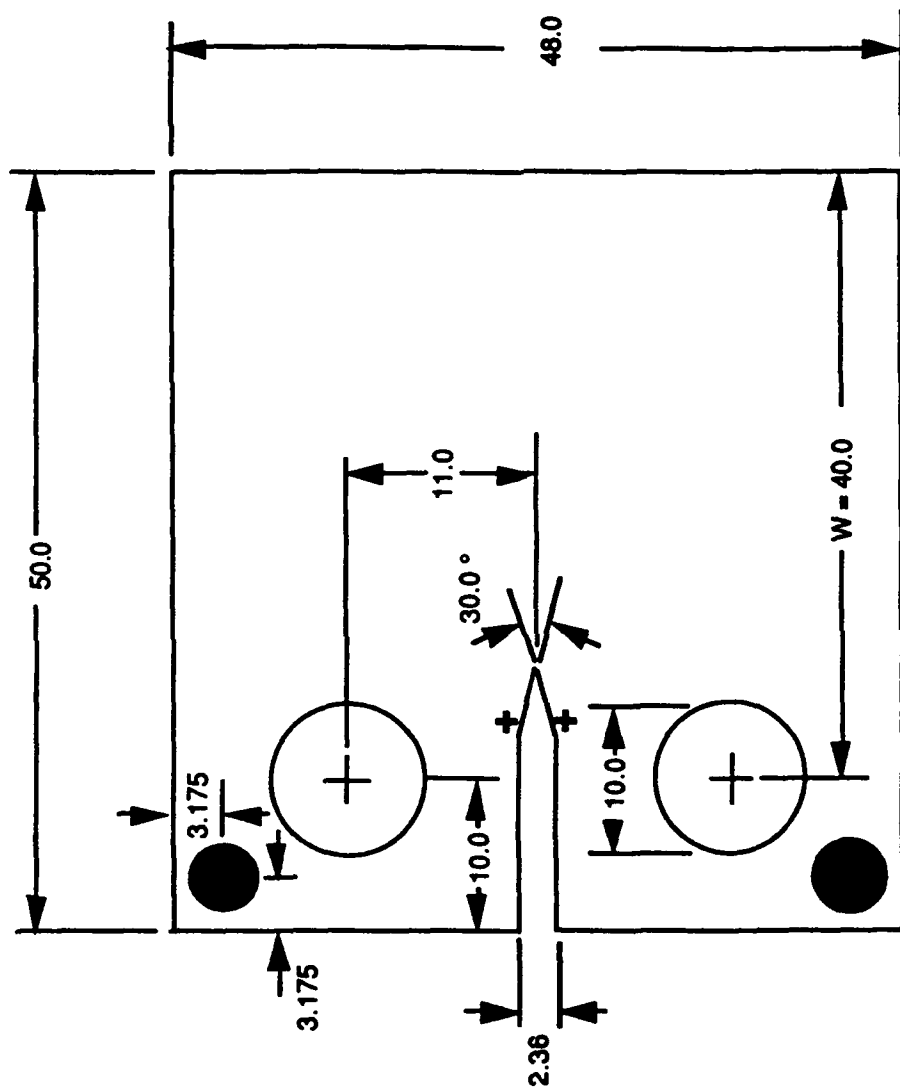


Fig. 4.10-1 Compact specimen with "+" as current source locations and "-" as electric potential probe locations.
(dimensions in mm)

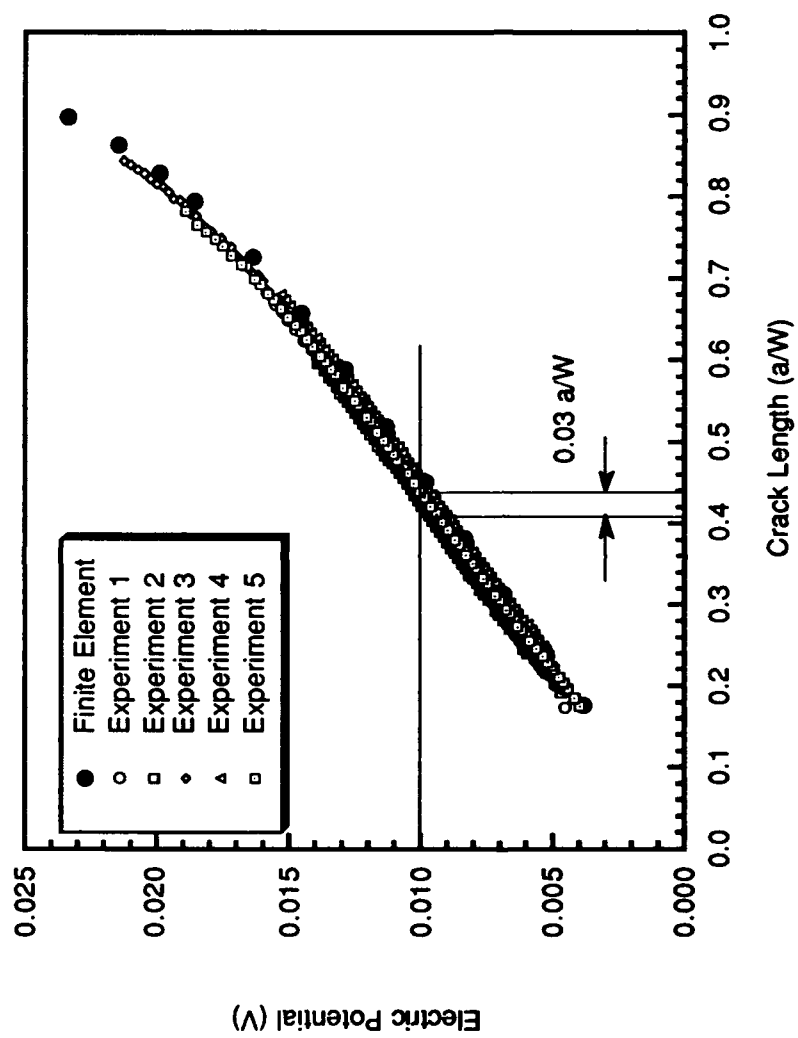


Fig. 4.10-2 Experimental electric potential calibration curves and base-line finite element solution.

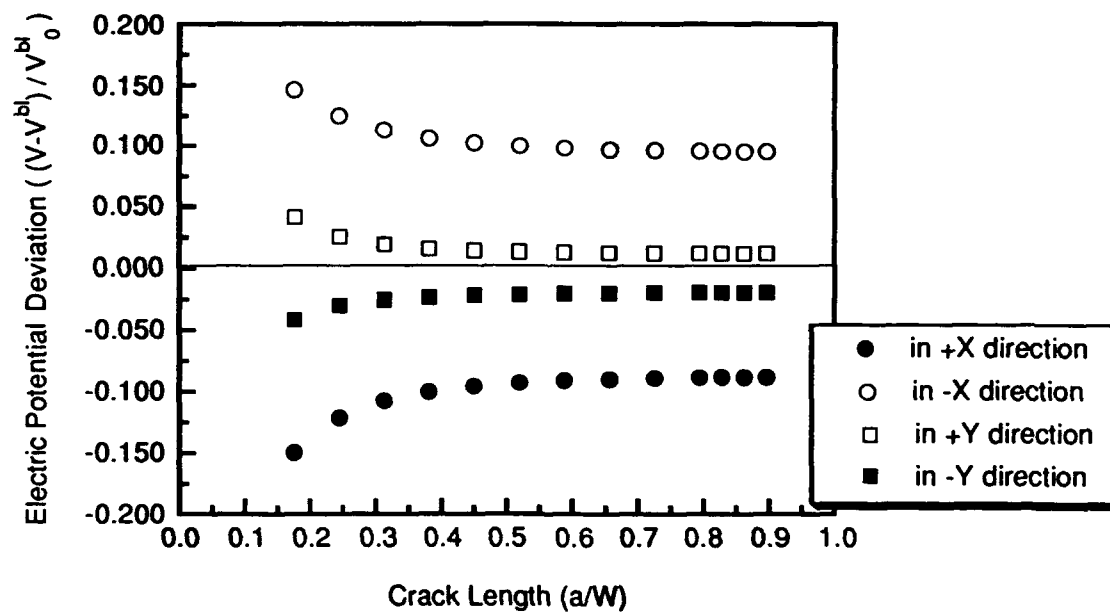
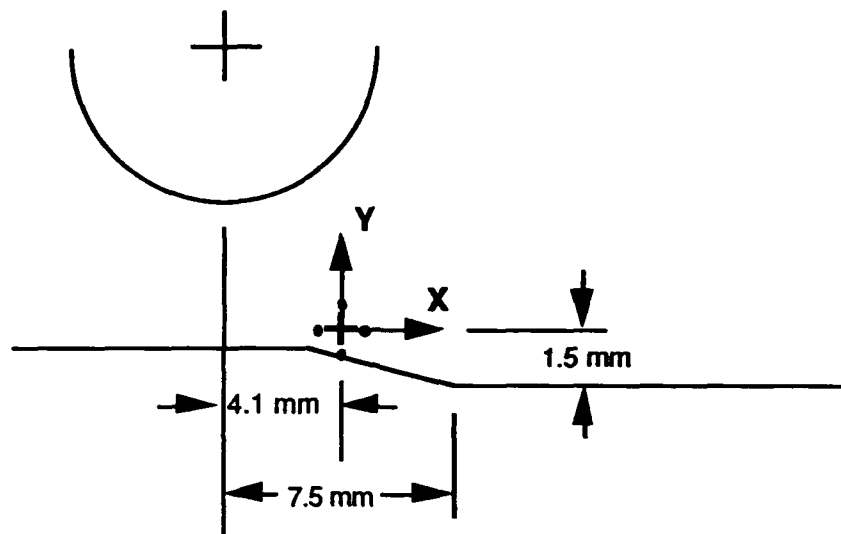


Fig. 4.10-3 Electric potential probe location shifts (± 0.7 mm) and resulting electric potential deviation from base-line electric potential.

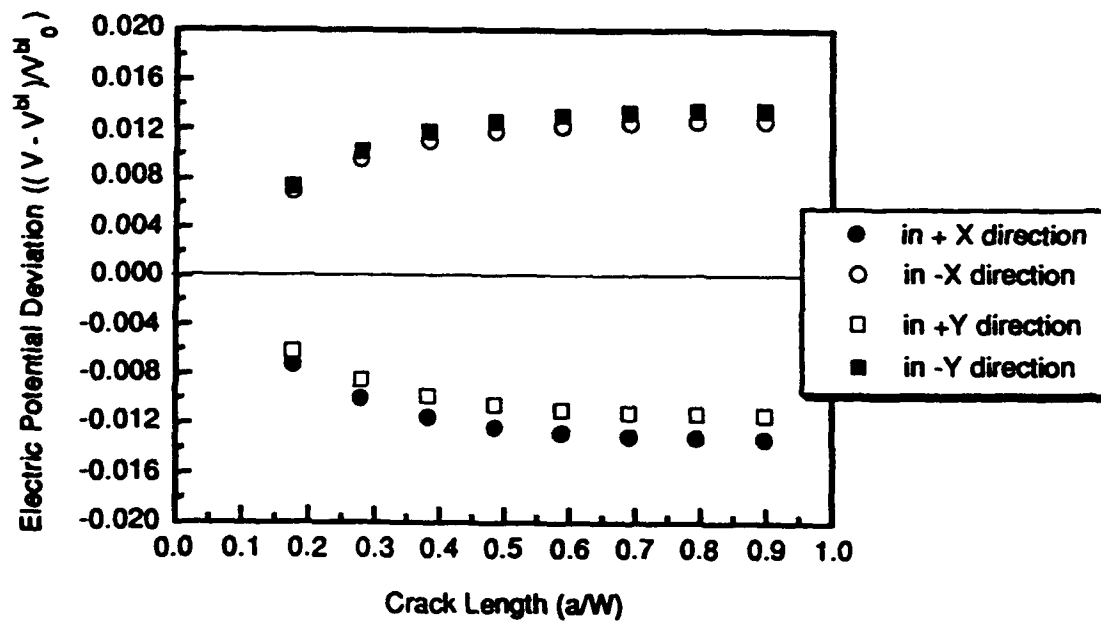
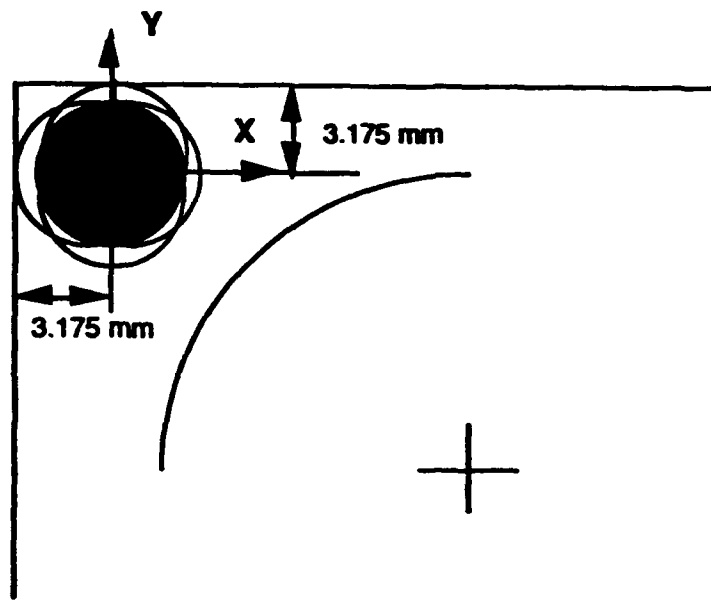


Fig. 4.10-4 Current source location shifts and resulting electric potential deviations from base-line electric potential.

corresponding crack length. The shifts in the current source locations has a lesser effect on resulting electric potential measured as compared to electric potential probe shifts.

In the last investigation, the effects of a nonuniform temperature distribution on the measured electric potential were determined. Only the center region of the specimen was heated to a uniform temperature of 649°C. To account for the nonuniform temperature distribution, a finite element analysis was completed with the temperature dependent material properties of Inconel-718 varying from element to element. An estimate of the temperature distribution was determined from a finite difference analysis of the experimental specimen. The temperature distribution and the resulting electric potential deviations of the nonuniform temperature case from uniform temperature case (649°C) are plotted in Fig. 4.10-5. The electric potential from two locations on the compact specimen were sampled in this investigation, one at the base-line location (Pt A) and the other on the front edge of the specimen (Pt B). This nonuniform temperature distribution had the least effect on the resulting electric potential of all the investigations.

The analysis considered the effects of electric potential probe location, current source location and nonuniform temperature distribution on the measured electric potential. The effect of shifts in the electric potential probes had the most significant effect on the resulting electric potential. Shifts in the location of the current sources had less of an effect on the resulting electric potential than the electric potential probe shift. The nonuniform temperature distribution had the least effect on the electric potential of all the results found in this investigation. The combination of these results could not reasonably produce the experimental variations observed, (Fig. 4.10-2). Time did not permit investigation of effects of other variables including machining of loading holes, initial crack length, initial crack tip shape, and blunting on the measured electric potential.

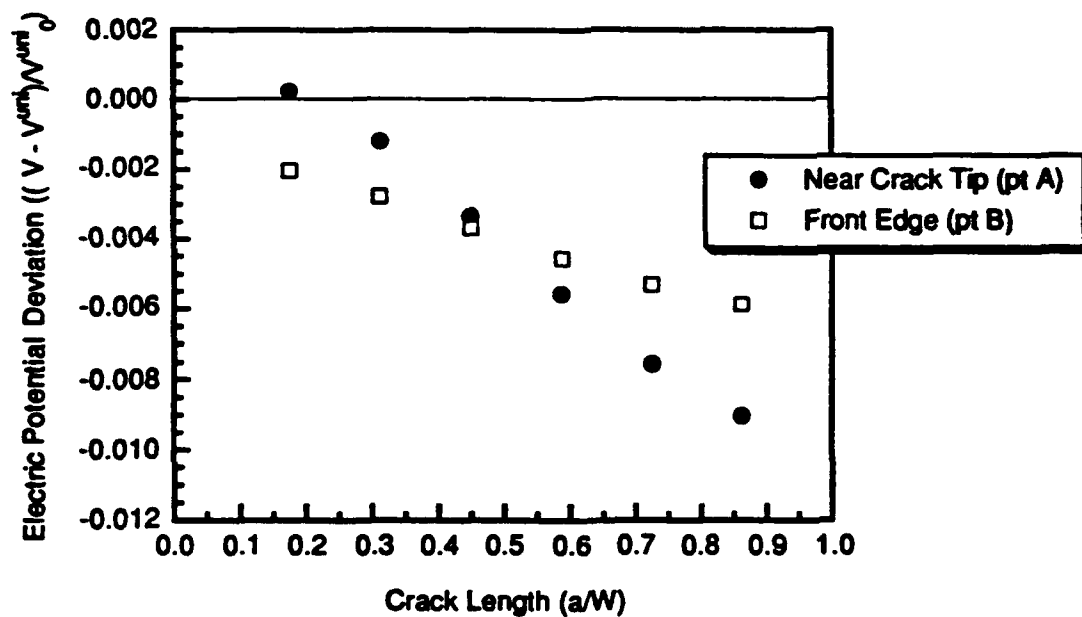
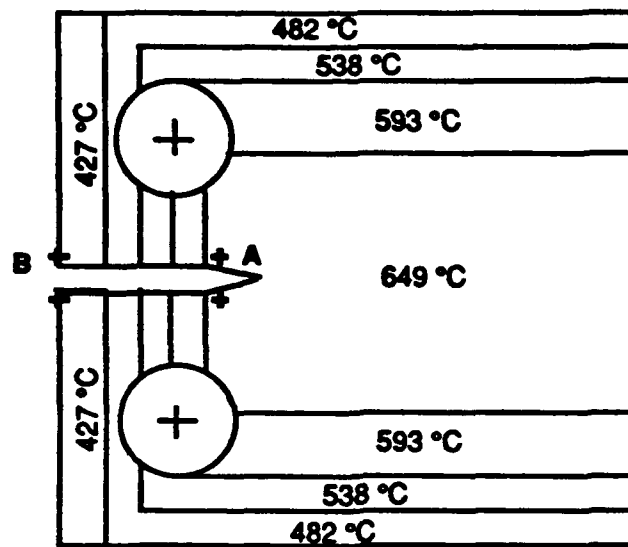


Fig. 4.10-5 Nonuniform temperature distribution and resulting electric potential deviation from baseline electric potential.

Section 5

Data Archival and Test Support Activities

5.1 Mechanical Property Data

Various tests were conducted in the laboratory to provide basic mechanical property data and material responses of existing and developmental materials. The procedures set forth in the ASTM Standard Test Methods were followed for these tests unless otherwise specified by the engineer/scientist.

The types of tests that have been performed were fatigue crack growth at room and elevated temperatures, axial fatigue, fracture toughness, fiber fragmentation, crack growth resistance, and tensile tests at room temperature to 980°C. These tests were performed on numerous alloys of titanium, some aluminum alloys, composites, and selected fibers. After each test, the data were analyzed, documented, and reported to the respective project engineer.

5.1.1 Coefficient of Thermal Expansion (CTE)

5.1.1.1 Uniaxial Test Procedure

An experimental study was undertaken to determine the coefficient of thermal expansion (CTE) of various materials using a standard type tensile specimen. The test specimen was loaded in a servo-hydraulic test machine and maintained at zero load. An MTS air-cooled extensometer with an 0.5 inch gage length was placed on the test specimen. Woven fiberglass tubes were placed on the extensometer rods to minimize spurious strain readings caused by thermal gradients in the rods. Water-cooled load train sections above and below the specimen avoided heating of the load cell and actuator assemblies, respectively.

Thermocouples were welded onto the sample so that the test temperature could be controlled. A single zone furnace maintained the temperature of the gage length within $\pm 2^\circ\text{C}$ of the set point temperatures. To provide consistent displacement data on heating and returning

to room temperature, an initial thermal cycle was applied to the specimen. The temperature range for this initial shake-down cycle was about that of the range for the test.

An initial voltage reading was taken of the displacement while the test specimen was at room temperature. The test specimen was initially heated from room temperature to 150°F, where another voltage reading was recorded. The test temperature was increased in 100°F increments up to 1450°F, while taking readings at each increment. Data were recorded in the same fashion as the temperature was decreased. The secant CTE at reference temperature, T_o , was determined in the following manner:

$$CTE = \frac{(V - V_o) * Cal.Factor}{G.L * (T - T_o)} \quad (22)$$

where V is the displacement voltage at temperature, V_o is the initial room temperature displacement voltage, the Cal. Factor is the calibration factor for the extensometer, G.L. is the reference extensometer gage length, and T is the test temperature.

This uniaxial test for CTE was conducted on two nickel-base superalloys, IN718 and Waspaloy, to evaluate the procedure. The results, shown in Figs. 5.1.1.1-1 and 5.1.1.1-2, indicated fairly good agreement with an independent source [Aerospace Structural Metals Handbook].

5.1.1.2 Results for Ti-24Al-11Nb Foil

When a tensile test sample of a material could not be fabricated and only small samples were available, a dilatometer was used to determine CTE. For Ti-24Al-11Nb neat foil material, thermal expansion tests were conducted in three perpendicular directions; longitudinal, transverse and thickness. Thermal expansion tests were conducted on single crystal sapphire [Hahn] to determine temperature dependent calibration factors for the dilatometer for both secant and tangent CTE as a function of temperature.

The strain-temperature data from the thermal expansion tests for Ti-24Al-11Nb are shown in Fig. 5.1.1.2-1 in the transverse (curves 1 and 3), longitudinal (curve 2) and thickness (curves 4-6) directions. The strains in in-plane, i.e., the transverse and longitudinal directions, showed a similar trend whereas a significant difference was noted between the strains in the in-plane directions and the thickness direction.

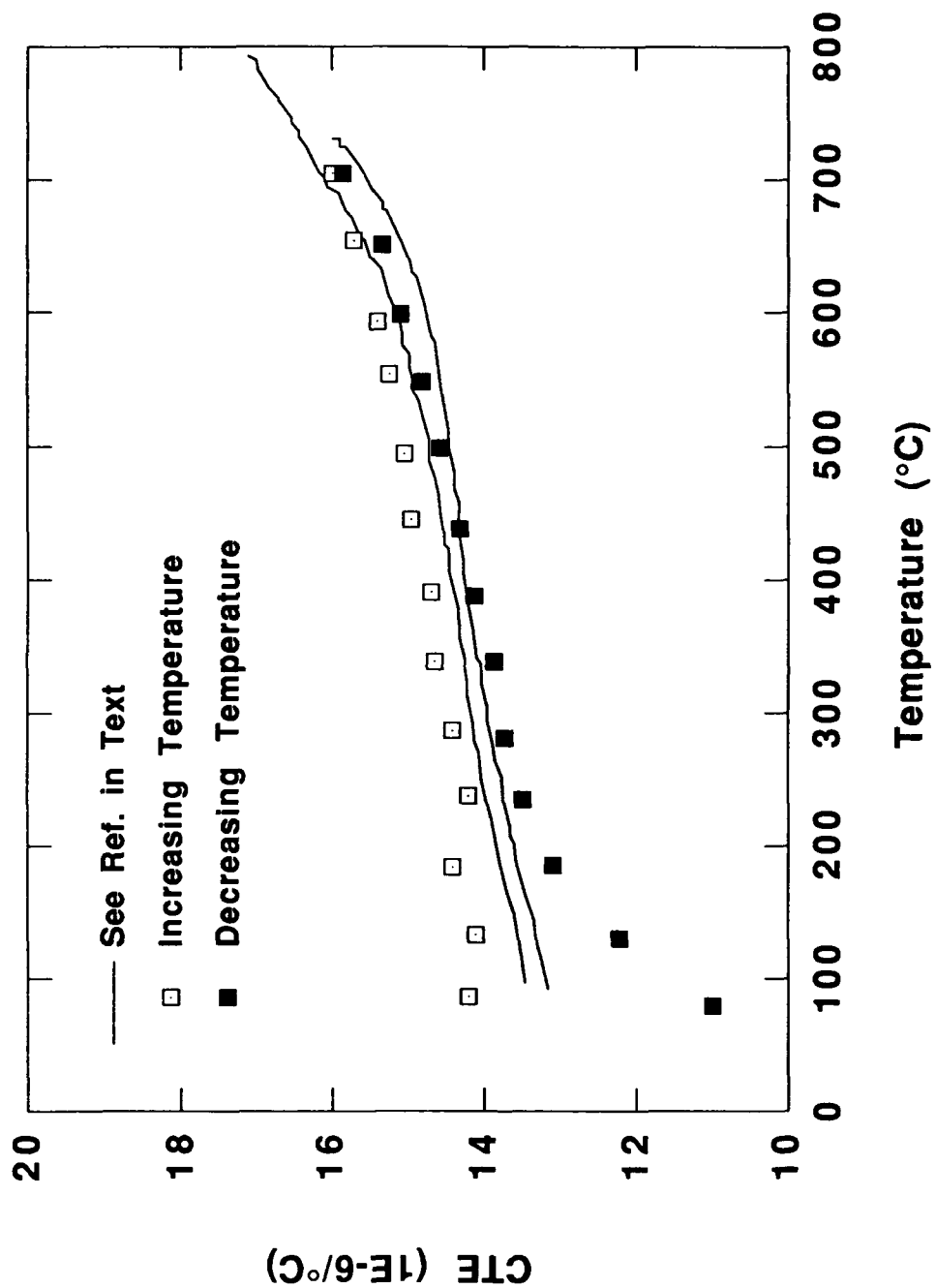


Fig. 5.1.1.1-1 IN-718 - secant α .

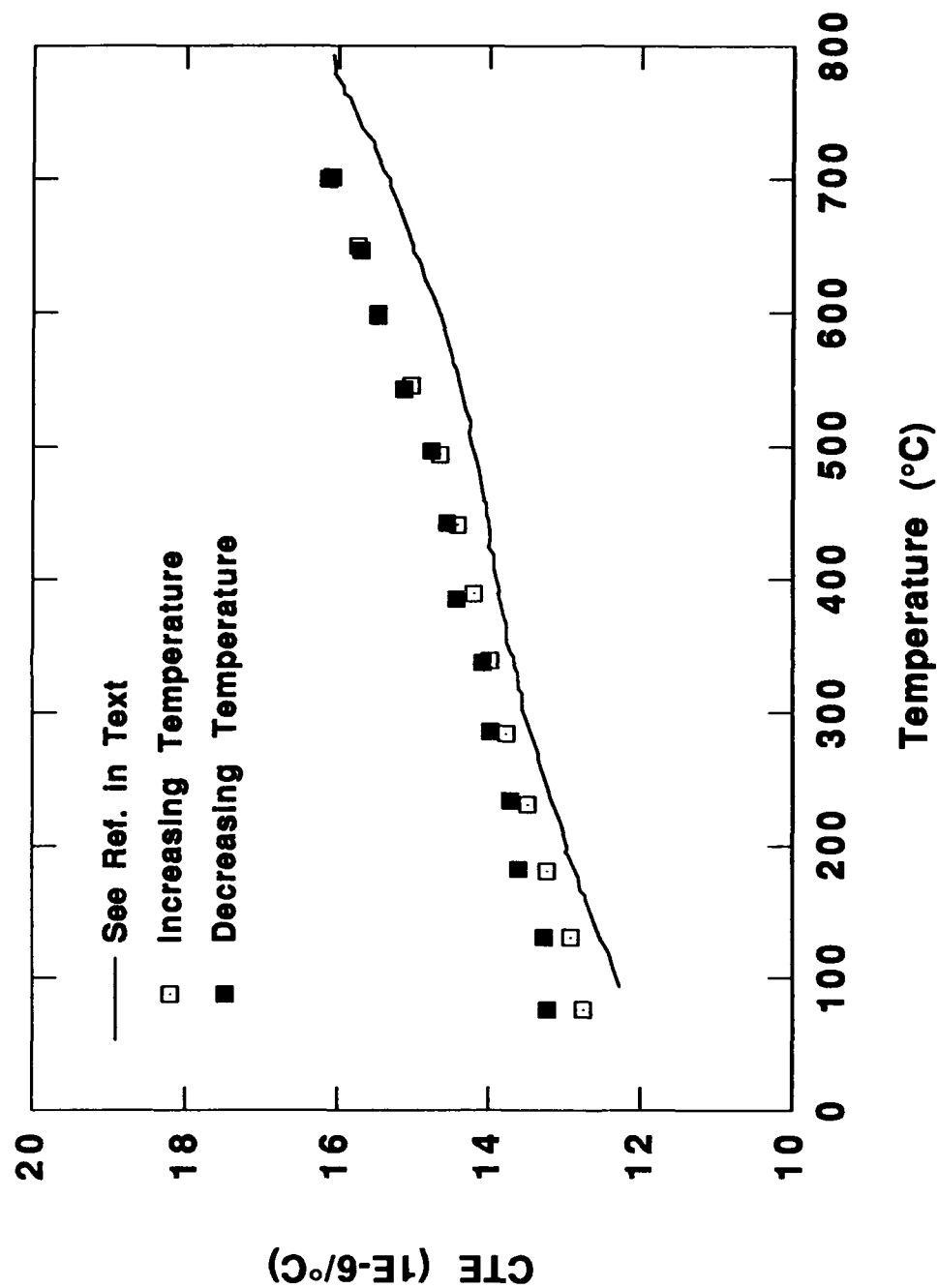


Fig. 5.1.1.1-2 WASPALLOY - secant α .

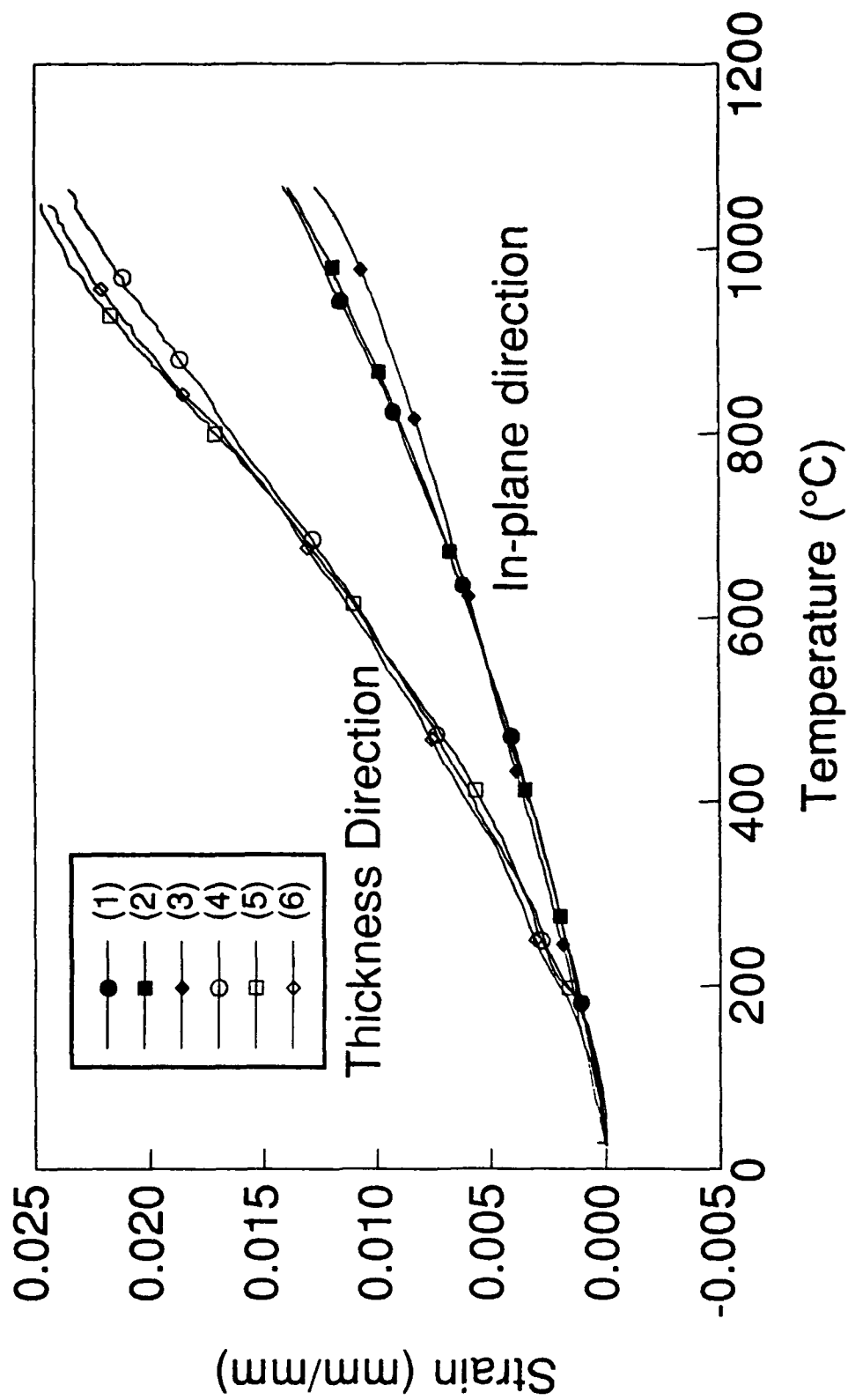


Fig. 5.1.1.2-1 Thermal expansion plots for Ti3Al in the in-plane and thickness directions.

The secant CTE was computed with respect to the processing temperature of 1010°C using the equation:

$$\alpha_s = (\epsilon(T) - \epsilon(1010)) / (T - 1010) \quad (23)$$

where ϵ is the strain and T is the temperature. The tangent CTE was determined by taking the derivative of least square error curve fits to the strain-temperature data. The secant and tangent CTEs in the in-plane and thickness directions are plotted as a function of temperature in Figs. 5.1.1.2-2 and 5.1.1.2-3, respectively, with corresponding polynomial curve fits. These CTE values are also tabulated in Table 5.1.1.2-1.

Table 5.1.1.2-1 Secant CTE and Tangent CTE for Ti-24Al-11Nb Foil in the In-Plane and Thickness Directions

Temperature (°C)	Secant CTE In-Plane (°C)	Secant CTE Thickness (°C)	Tangent CTE In-Plane (°C)	Tangent CTE Thickness (°C)
20	1.131E-05	2.148E-05	8.705E-06	8.110E-06
100	1.150E-05	2.222E-05	9.829E-06	1.311E-05
200	1.169E-05	2.296E-05	1.052E-05	1.746E-05
300	1.186E-05	2.349E-05	1.079E-05	2.046E-05
400	1.204E-05	2.383E-05	1.088E-05	2.252E-05
500	1.226E-05	2.400E-05	1.095E-05	2.384E-05
600	1.255E-05	2.399E-05	1.113E-05	2.454E-05
700	1.293E-05	2.382E-05	1.152E-05	2.471E-05
800	1.344E-05	2.350E-05	1.221E-05	2.440E-05
900	1.408E-05	2.303E-05	1.327E-05	2.364E-05
1000	1.488E-05	2.241E-05	1.480E-05	2.248E-05
1010	1.498E-05	2.234E-05	1.498E-05	2.234E-05
1050	1.536E-05	2.205E-05	1.575E-05	2.175E-05

5.1.2 Tensile Behavior of Titanium Aluminides

The tensile behavior has been determined for a number of titanium aluminide intermetallics at temperatures ranging from room temperature to 980°C. Most of these tensile characterizations were used to determine the effect of heat treatment and alloying variations on the strength and ductility properties of the materials. Two alloys of particular interest were Ti-25Al-10Nb-3V-1Mo and Ti-25Al-25Nb. The tensile properties of Ti-25Al-10Nb-3V-1Mo were

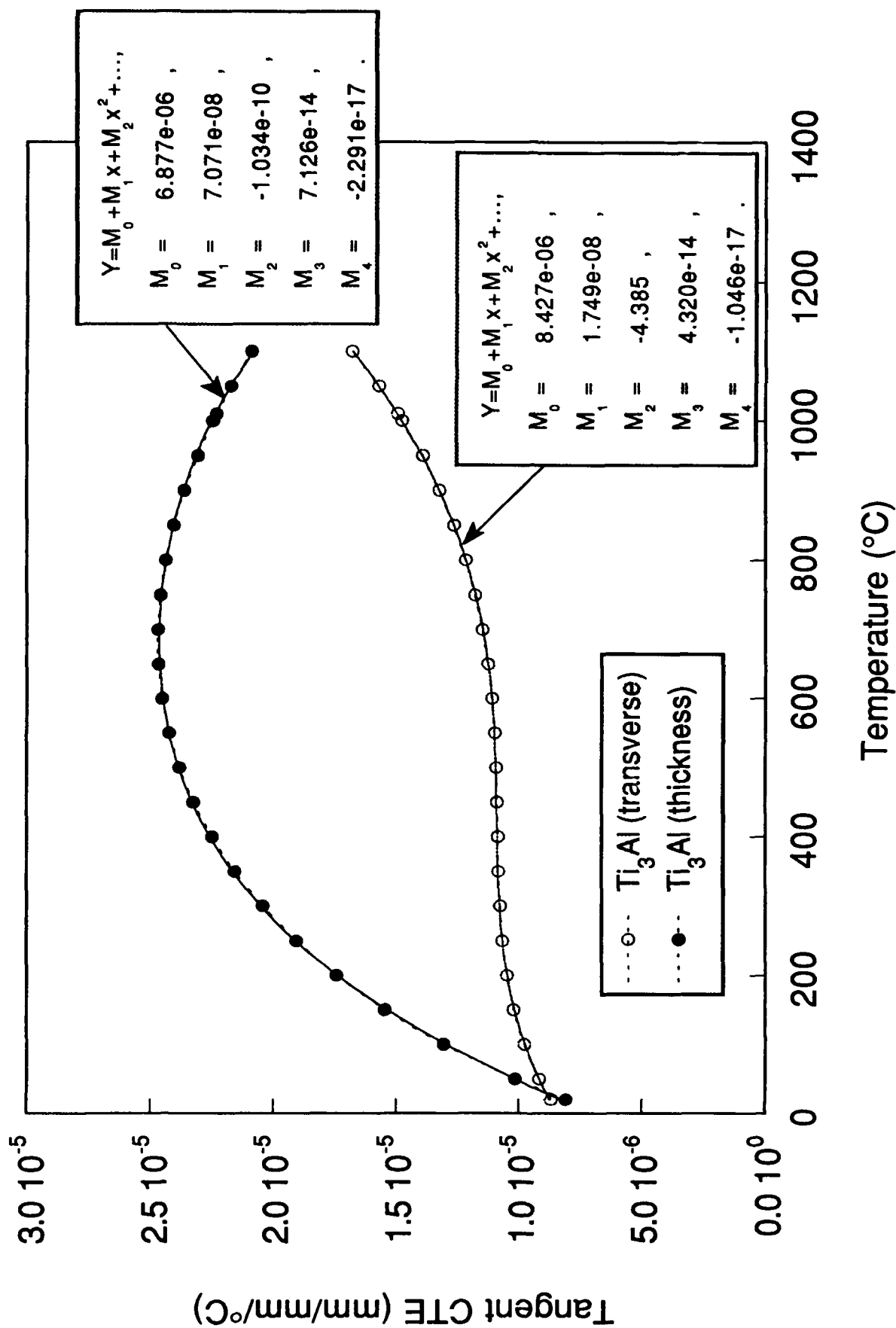


Fig. 5.1.1.2-2 Secant CTE (with $T_{ref}=1010^\circ\text{C}$) for Ti_3Al in the in-plane and thickness directions and associated curve fits.

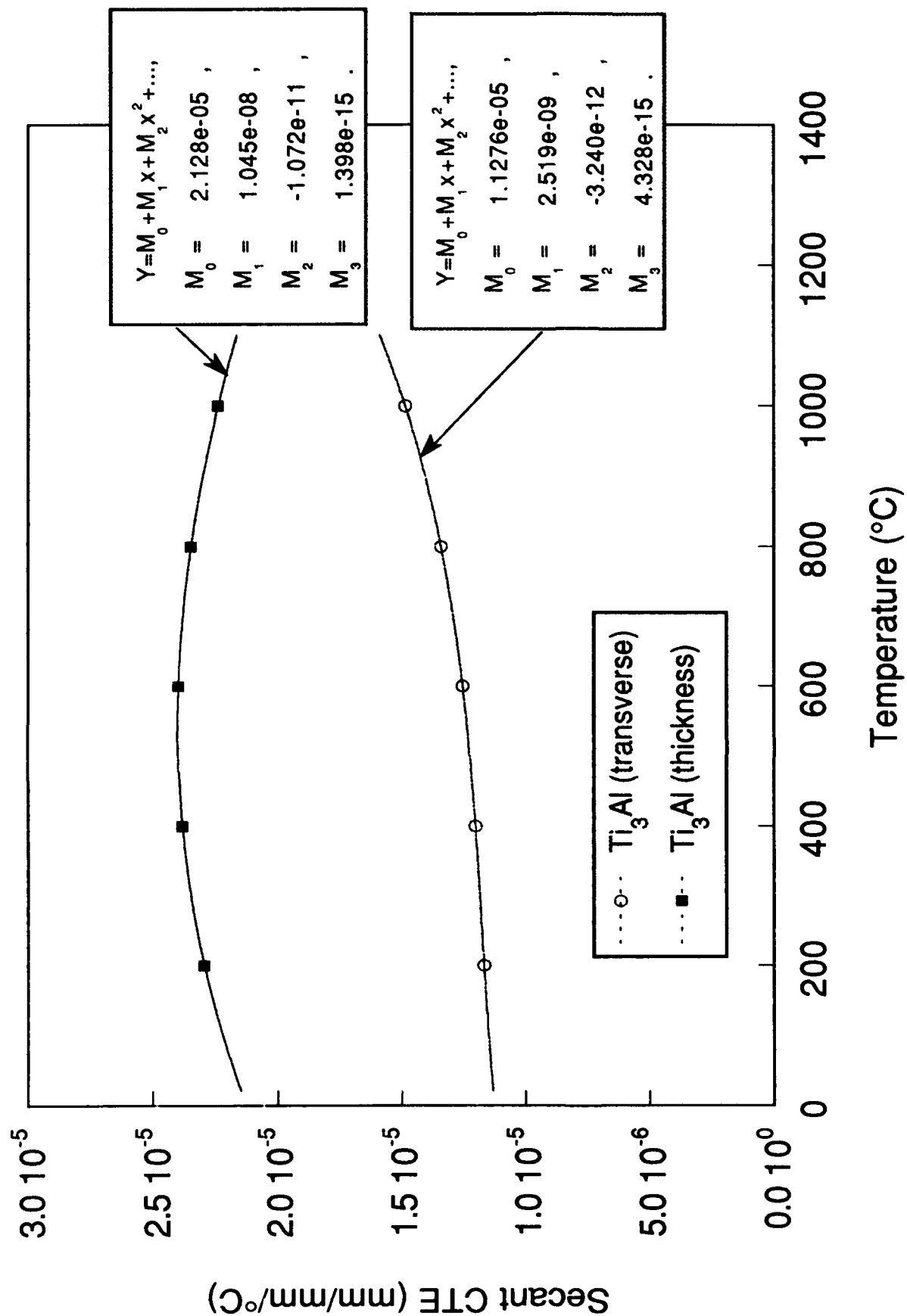


Fig. 5.1.1.2-3 Tangent CTE for Ti_3Al in the in-plane and thickness directions and associated curve fits.

dramatically affected by the microstructure [Ward et al.]. The tensile properties of Ti-25Al-25Nb were completed as part of a study of a high niobium, orthorhombic alloy and these results will be published in the future.

5.1.3 R-Curve of Particulate Composite

R-curve tests were conducted on a niobium particulate toughened niobium silicate composite, in accordance with ASTM Standard E561-86, "Standard Practice for R-Curve Determination." The test specimens were precracked to an a/W of 0.55 on a standard servo-hydraulic test machine using constant stress intensity control. R-curve tests were then conducted using stroke control. Data were collected using an automated test program and autographically on an X-Y plotter. The results of this test series are being interpreted by the engineer and will be published at a later date.

5.1.4 Fragmentation Test for MMC

The fragmentation of fibers in a continuously reinforced metal matrix composite was studied by testing tension specimens with a single fiber consolidated in a titanium aluminide matrix. Load-displacement traces and acoustic emission were used to determine failure of the fiber within the matrix. SEM analysis was used to determine fiber/matrix/interface failure mechanisms. The data are being analyzed and the results will be published in the future.

5.1.5 S-N Behavior of Titanium Alloy

Titanium alloy castings, particularly Ti-6Al-4V, have been widely accepted and utilized by the aerospace industry in applications requiring moderate strength and light weight. However, applications where high strength, corrosion resistant materials are needed have generally used castings of precipitation-hardened stainless steels, often at a considerable weight penalty. Currently, high strength beta titanium alloy castings are being considered as replacement to precipitation-hardened stainless steels due to their high strength-to-weight ratios, excellent corrosion resistance, high fatigue strengths, and relative low cost when compared to wrought products. Previous work has demonstrated that high tensile and fatigue strength levels can be obtained in metastable beta alloy castings. However, wide scatter of tensile elongation and high cycle fatigue results were measured; the result of occasional premature failures.

This research [Porter] investigated the tensile and fatigue behavior of Ti-15V-3Al-3Cr-3Sn (Ti-15-3) investment castings, with a special emphasis on the reasons and mechanisms of

crack initiation. The hot isostatically pressed (HIP'd) and solution treated and aged cast parts displayed tensile and fatigue strengths above those commonly found in alpha+beta titanium alloys. The nature of the tensile and fatigue fractures were studied in detail. Grain boundary alpha (GB α) phase was identified as playing a major role in determining the tensile ductility and the fatigue crack initiation.

5.1.6 Tensile Properties of Fibers

The UDRI has developed the capability to determine tensile properties of high-modulus single filament materials. The filament testing system utilizes a laser extensometer to measure fiber elongation during the test.

This system was used to conduct tension tests on SCS-6 silicon carbide fibers extracted from consolidated composites. The effects of the composite consolidation and thermal cycling on the tensile properties of the fiber were investigated [Revelos and Smith].

5.1.7 K_{Ic} of Titanium Aluminides and Particulate Composite

Plane-strain fracture toughness testing, in accordance with ASTM E399, has been performed on several brittle materials including gamma titanium aluminides and silicide particulate reinforced niobium composite. The data from these materials are being analyzed and will be published in the future.

5.1.8 Fatigue Crack Growth of Titanium Alloys

The fatigue crack growth rate of a near alpha titanium alloy, IMI-834, was studied as a function of temperature, frequency, and superimposed hold times a maximum load. It was the intent of this investigation to determine if da/dN versus ΔK accurately describes crack growth rate, or if a summation approach using da/dN (cyclic term) + da/dt (time dependent term) in a linear cumulative damage model in more appropriate [Zawada].

The fatigue crack growth rates of high temperature titanium alloys -- Ti-1100, Ti-6242, Ti-6242S beta, and Ti-6242S alpha + beta -- were studied as a function of temperature at a frequency of one hertz. The results of these tests will be compared to the fatigue crack growth rates of IMI-834 titanium alloy. The results will be published at a later date.

5.2 Electronics Fabrication

Maintaining a state-of-the-art mechanical test laboratory involved the development and use of advanced measurement devices, some of which were constructed in-house. The UDRI has supported these activities in the MLLN laboratories by designing, assembling, and installing various electronic devices, interfaces, and systems. Examples of this work included:

- 1) a TTL relay driver board to accept TTL level inputs and to drive either internal or external relays. The board was capable of using either positive or negative input logic.
- 2) a closed loop proportional/integral controller designed to control the applied loads on a load frame by varying the air pressure in a pneumatic cylinder. The controller included limits, a multifunction display, and external command input.
- 3) a laser power supply/controller/signal conditioner system used in conjunction with a solid-state laser interferometric displacement gage system [Hartman and Nicholas].

5.3 SiC/1723 Processing

Test panels of a ceramic matrix composite, consisting of SiC fibers consolidated into a 1723 aluminosilicate matrix were processed in-house. The test panels were fabricated in various thicknesses and fiber orientations as desired. The tensile strength for this composite was over 800 MPa for unidirectional specimens. This high tensile strength was attributed to the use of a state-of-the-art pre-preg winder to prepare the lamina panels and a resulting composite fiber volume fraction of 45%. The pre-preg winder allowed the fibers to be impregnated with the glass matrix material and provided very good parallel orientation of the fibers in the laminae. Other fiber/matrix composites could also be fabricated on the winder.

5.4 Data Maintenance

The primary outputs from the MLLN mechanical test laboratories were the test data. The UDRI has realized that a large amount of time, effort, and money was required to collect this data. Thus, a comprehensive data archival system has been instituted so that the original data in both printed and digital form were maintained within the laboratory. Researchers have complete access to the data, however, the original data may not be removed from the archive. Several

forms of magnetic media were used to archive the data and two copies of all magnetic media containing archived data were maintained at all times.

Working data were maintained on-line on the laboratory MicroVax for immediate access. These data were backed up on a regular basis by the system manager. The system manager allocated system resources as required and individual system users were responsible for the data stored in their accounts.

BIBLIOGRAPHY

Aboudi, J., **"Damage in Composites-Modeling of Imperfect Bonding,"** *Composites Science and Technology*, 28, 1987, pp. 103-128.

Adams, D. F., **"Micromechanical Modeling of Yielding and Crack Propagation in Unidirectional Metal Matrix Composites,"** *Testing Technology of Metal Matrix Composites*, ASTM STP 964, P. R. DiGiovanni and N. R. Adsit, Eds, American Society for Testing and Materials, Philadelphia, PA, 1988, pp. 93-103.

Aerospace Structural Metals Handbook, Vols. 4 and 5, W.F. Brown, Jr., ed., AFML-TR-68-115, 1978 Revision-Supplement XI, June 1978.

Ahmad, J., Private Communication, 1988.

Ahmad, J., **"A Micromechanics Analysis of Cracks in Unidirectional Fiber Composites,"** 91-WA/APM-6, *Journal of Applied Mechanics*, ASME, 1991.

Ahmad, J. and Papaspyropoulos, V., **"Finite Element Analysis of Cracks in Composite Materials,"** Final report to the University of Dayton Research Institute, October 1991.

Ashbaugh, N.E., **"Effects of Load History and Specimen Geometry on Fatigue Crack Closure Measurements,"** *Mechanics of Fatigue Crack Closure*, ASTM STP 982, J.C. Newman, Jr. and W. Elber, Eds., American Society for Testing and Materials, Philadelphia, PA, 1988, pp. 186-196.

Ashbaugh, N.E., **"Crack-Length Expression as a Function of Compliance for Center-Cracked Tension Specimen,"** *ASTM Research Report RR-E24-1012*, June, 1986.

Ashbaugh, N.E. and Johnson, D.A., **"Determination of Crack Length as a Function of Compliance and Gage Length for an M(T) Specimen,"** To be published as an ASTM Research Report, 1991.

Ashbaugh, N. E., Khobaib, M., Hartman, G. A., Coker, D., Kroupa, J. L., John, R., Johnson, D. A., Goodman, R. C., Maxwell, D. A., and Muhic, L. A., **"Mechanical Properties of Advanced Engine Materials,"** - 1989 Annual Report, UDR-TR-90-85, August 1990.

Ashbaugh, N.E. and Nicholas, T., **"Threshold Crack Growth Behavior of Nickel-Base Superalloy at Elevated Temperature,"** *Fracture Mechanics: Perspectives and Directions (Twentieth Symposium)*, ASTM STP 1020, R.P. Wei and R.P. Gangloff, Eds., American Society for Testing and Materials, Philadelphia, PA, 1989, pp. 628-638.

Atkinson, C., Smelser, R.E., and Sanchez, J., **"Combined Mode Fracture via the Cracked Brazilian Disk Test,"** *International Journal of Fracture*, Vol. 18, No. 4, April 1982, pp. 279-291.

Awaji, H. and Sato, S., **"Combined Mode Fracture Toughness Measurement by the Disk Test,"** *Journal of Engineering Materials and Technology*, Vol. 100, April 1978, pp. 175-182.

Bahei-El-Din, Y. A., **"Plastic Analysis of Metal-Matrix Composite Laminates,"** Ph. D. Dissertation, Duke University, 1979.

Balsone, S. J., Maxwell, D. C., Khobaib, M., and Nicholas, T., **"Frequency, Temperature and Environmental Effects On Fatigue Crack Growth in Ti_3Al ,"** *Proceedings of the Fourth International Conference on Fatigue and Fatigue Thresholds*, July 1990.

Balsone, S. J. and Maxwell, D. C., **"Fatigue Crack Growth Behavior of the Titanium Aluminide Ti-25Al-25Nb,"** Submitted for review to ASTM STP of 23rd. National Symposium on Fracture Mechanics, June 1991.

Barrett, D.J., **A Model for Thermoplastic Analysis of Metal Matrix Laminates**, NASP Technical Memorandum 1126, January 1991.

Barrett, D. J. and Buesking, K. W., **Temperature Dependent Nonlinear Metal Matrix Laminate Behavior**, NASA CR-4016, September 1986.

Barsoum, R.S., **"Triangular Quarter-Point Elements as Elastic and Perfectly-Plastic Crack Tip Elements,"** *International Journal for Numerical Methods in Engineering*, Vol. 11, 1977, pp. 85-98.

Beals, J.T. and Bar-ON, I., **"Fracture and Fatigue Crack Propagation of Silicon Nitride with Two Different Microstructures,"** *Ceramic Engineering and Science Proceedings*, American Ceramic Society, Vol. 11, No. 7-8, July-August 1990, pp. 1061-1071.

Bigelow, C. A., Johnson, W. S., and Naik, R. A., **"A Comparison of Various Micromechanics Models for Metal Matrix Composites,"** *Mechanics of Composite Materials and Structures*, J. N. Reddy and J. L. Telpy, Eds., The American Society of Mechanical Engineers, 1989, pp. 21-31.

Bischoff, E., Ruhle, M., Sbaizero, O., and Evans, A.G., **"Microstructural Studies of the Interfacial Zone of a SiC-Fiber-Reinforced Lithium Aluminum Silicate Glass-Ceramic,"** *Journal of American Ceramic Society*, Vol. 72, No. 5, May 1989, pp. 741-745.

Brockman R. A., **"MAGNA: A Finite System for Three Dimensional Nonlinear Static and Dynamic Structural Analysis,"** *Comp. & Struct.*, Vol 13, 1981, pp. 415-423.

Bushnell D., **"A Subincremental Strategy for Solving Problems Involving Large Deflections, Plasticity and Creep,"** *Constitutive Equations in Viscoplasticity - Computational and Engineering Aspects*, AMD - Vol. 20, ASME, 1976.

Butkus, L.M., Zawada, L.P., and Hartman, G.A., **"Fatigue Test Methodology and Results for Ceramic Matrix Composites at Room and Elevated Temperatures,"** *Cyclic Deformation, Fracture, and Nondestructive Evaluation of Advanced Materials*, ASTM STP 1192, American Society for Testing and Materials, 1990.

Chai, L. and Dharani, L.R., **"Embedded and Surface Flaws in Unidirectional Composites,"** *Computers and Structures*, in press.

Chamis, C. C. and Hopkins, D. A., **"Thermoviscoplastic Nonlinear Constitutive Relationships for Structural Analysis of High-Temperature Metal Matrix Composites,"** *Testing Technology of Metal Matrix Composites*, ASTM STP 964, P. R. DiGiovanni and N. R. Adsit, Eds., American Society for Testing and Materials, Philadelphia, PA, 1988, pp. 177-196.

^{a)}Coker, D. and Ashbaugh, N.E., **"Characterization of Fracture in [0.90]₃, SiC/1723 Composites,"** UDR-TR-91-64, Dayton, Ohio, 1991.

^{b)}Coker, D. and Ashbaugh, N. E., **"Finite Difference Analysis of Thermomechanical Cyclic Behavior of Unidirectional Composites,"** To be published as a UDRI Technical Report, 1992.

Dauskardt, R.H. and Ritchie, R.O., **"Fatigue Crack Propagation in Transformation-Toughened Zirconia Ceramic,"** *Journal of American Ceramic Society*, Vol.70, No. 10, October 1987, pp. C-248-C-252.

^{a)}Dharani, L.R. and Chai, L., **"Embedded Flaws in Unidirectional Composites,"** *Composite Structures*, in press.

^{b)}Dharani, L.R. and Chai, L., **"Multiple Cracks in 3-D Unidirectional Composites: Compliance and Energy Release Rates,"** *Journal of Composites Technology and Research*, in press.

Druce, S.G. and Booth, G.S., **"The Effects of Errors in Geometric and Electrical Measurements on Crack Length Monitoring by the Potential Drop Technique,"** *The Measurement of Crack Length and Shape during Fracture and Fatigue*, Ed. Beevers, Chameleon Press LTD., 1980.

Dvorak, G. J. and Bahei-El-Din, Y. A., **"Plasticity Analysis of Fibrous Composites,"** *Journal of Applied Mechanics*, June 1982, Vol. 49, pp. 327-335.

Enderle, P.R. and Ashbaugh, N.E., **"Two Compliance Expressions for Arbitrary Locations Across a Crack in a CT Specimen,"** AFWAL-TR-85-4074, Wright Laboratory, Wright-Patterson Air Force Base, OH, June 1985.

Fett, T., Matheck, C., and Munz, D., **"On the Calculation of Crack Opening Displacement from the Stress Intensity Factor,"** *Engineering Fracture Mechanics*, Vol. 27, No. 6, 1987, pp. 697-715.

Gabb, T.P., Gayda, J. and MacKay, R.A., **"Isothermal and Nonisothermal Fatigue Behavior of a Metal Matrix Composite,"** *J. Comp. Mat.*, Vol. 24, 1990, pp. 667-686.

Gambone, M.L., **"Fatigue and Fracture of Titanium Aluminides,"** WRDC-TR-89-4145, Vol. II, *Final Report*, Materials Directorate, Wright Laboratory, WPAFB, OH, February 1990.

Hartman, G.A. and Ashbaugh, N.E., **"A Fracture Mechanics Test Automation System for a Basic Research Laboratory,"** *The Applications of Automation Technology to Fatigue and Fracture Testing*, ASTM STP 1092, A. Braun, F. Smith and N. Ashbaugh, Eds, American Society for Testing and Materials, Philadelphia, PA, 1990.

Hartman, G.A. and Ashbaugh, N.E., **"Load Pin Size Effects in the C(T) Geometry,"** To be published in an ASTM Research Report, American Society for Testing and Materials, Philadelphia, PA, 1991.

Hartman, G.A. and Nicholas, T., **"An Enhanced Laser Interferometer for Precise Displacement Measurements,"** *Journal of Experimental Mechanics*, February 1987, pp. 24-26.

Herakovich, C.T., Aboudi, J., and Lee, S-W., **"Nonlinear Composite Materials Micromechanics Model,"** Report on GE P.O.#200-14-14P94319, General Electric Company, September 1987.

Hopkins, D. A. and Chamis, C. C., **"A Unique Set of Micromechanics Equations for High-Temperature Metal Matrix Composites,"** *Testing Technology of Metal Matrix Composites, ASTM STP 964*, P. R. DiGiovanni and N. R. Adsit, Eds., American Society for Testing and Materials, Philadelphia, PA, 1988, pp. 159-176.

Hunsaker B., Haisler W.E., and Stricklin J.A., **"On the Use of Two Hardening Rules of Plasticity in Incremental and Pseudo Force Analysis,"** *Constitutive Equations in Viscoplasticity-Computational and Engineering Aspects*, AMD - Vol. 20, ASME 1976.

"Inconel Alloy 718," *Huntington Alloys Handbook*, Huntington, West Virginia, Fifth Ed., 1970.

Jata, K-V and Coker, D., **"Fracture Mechanisms in SCS-6/Ti-24Al-11Nb Composite,"** To be submitted to Materials Science and Engineering, 1992.

Jayaraman, N. and Rangaswamy, P., **"Residual Stresses in Ti₃Al-SCS6 Fiber Reinforced Metal Matrix Composites,"** *Titanium Aluminide Composites*, WL-TR-91-4020, P.R. Smith, S.J. Balsone and T. Nicholas, Eds., Materials Directorate, Wright Laboratory, WPAFB, OH, February, 1991.

Jenkins, M.G., Kobayashi, A.S., Sakai, M., White, K.W., and Bradt, R.C., **"Fracture Toughness Testing of Ceramics Using a Laser Interferometric Strain Gage,"** *American Ceramic Society Bulletin*, Vol. 66, No. 12, December 1987, pp. 1734-1738.

John, R. and Ashbaugh, N.E., **"Fatigue Crack Growth in a Silicon Carbide/Titanium Aluminide Composites,"** *Elevated Temperature Crack Growth, MD-Vol. 18*, ASME, S. Mall and T. Nicholas, Eds., November 1990, pp. 149-153.

^{a)}John, R. and Ashbaugh, N.E., **"Fatigue Crack Growth Parallel to Fibers in Unidirectional Metal Matrix Composites,"** *Titanium Aluminide Composites, WL-TR-91-4020*, P.R. Smith, Balsone, S.J. and T. Nicholas, Eds., Materials Directorate, Wright Laboratory, WPAFB, OH 45433, February 1991, pp. 497-510.

^{b)}John, R. and Ashbaugh, N.E., **"Fatigue Crack Growth in Ceramics and Ceramic Matrix Composites,"** *Cyclic Deformation, Fracture and Nondestructive Evaluation of Advanced Materials, ASTM STP*, American Society for Testing and Materials, Philadelphia, PA, Accepted for publication, 1991.

Johnson, D.A. and Ashbaugh, N.E., "**A Crack-Surface-Contact Model for Determining Effective-Stress-Intensity Factors**," Accepted by ASTM for publication in an STP.

Kantzos, P., Telesman, J. and Ghosn, L., "**Fatigue Crack Growth in a Unidirectional SCS-6/Ti-15-3 Composite**," *NASA Technical Memorandum 103095*, November 1989.

Khobaib, M., "**Creep Behavior of SCS-6/Ti-24Al-11Nb Composite**," *Titanium Aluminide Composites*, WL-TR-91-4020, P.R. Smith, S.J. Balsone and T. Nicholas, Eds., Materials Directorate, Wright Laboratory, Wright-Patterson AFB, Ohio, February 1991.

Khobaib, M., Ashbaugh, N.E., Hartman, G.A., Weerasooriya, T., Maxwell, D.C., and Goodman, R.C., "**Research on Mechanical Properties for Engine Life Prediction**," Final report for period covering August 1984 through September 1987, AFWAL-TR-88-4062, May 1988.

Khobaib, M., Ashbaugh, N.E., Hartman, G.A., Coker, D., Kroupa, J., Johnson, D., Maxwell, D.C., and Goodman, R.C., "**Mechanical Properties for Advanced Engine Materials**," UDR-TR-89-43, University of Dayton Research Institute, Dayton, Ohio, February 1989.

Khobaib, M. and Vahldiek, F.W., "**High Temperature Oxidation Behavior of Ti₃Al Alloys**," *2nd International SAMPE Metals and Metals Processing Conference*, 2-4 August 1988, Dayton, Ohio, pp. 262-270.

Khobaib, M. and Zawada, L., "**Tensile and Creep Behavior of a Silicon Carbide Fiber-Reinforced Aluminosilicate Composite**," *Ceram. Eng. Sci. Proc.* 12 [7-8], pp. 1537-1555, 1991.

Klintworth, G.C. and Webster, G.A., "**Optimization of Electric-Potential Methods of Measuring Crack Growth**," *Journal of Strain Analysis*, Vol 14, No 4, 1979, pp. 187-192.

Kortyna, B., "**Characterization of SCS-6/Ti-24Al-11Nb Composite at Elevated Temperature**," UDR-TR-92-52, University of Dayton Research Institute, Dayton, Ohio, April 1992.

Kortyna, B.R. and Ashbaugh, N.E., "**Fatigue Characteristics of a Titanium Aluminum Composite**," *Titanium Aluminide Composites*, WL-TR-91-4020, P.R. Smith, S.J. Balsone and T. Nicholas, Eds., Materials Directorate, Wright Laboratory, Wright-Patterson AFB, Ohio, February 1991.

Kroupa, J. L., "**Elastic-Plastic Finite Element Analysis of MMC Subjected to Thermomechanical Fatigue**," *Titanium Aluminide Composites*, WL-TR-91-4020, P.R. Smith, S.J. Balsone and T. Nicholas, Eds., Materials Directorate, Wright Laboratory, Wright-Patterson AFB, Ohio, February 1991.

Kroupa, J.L., Ashbaugh, N.E., Munro, S.D., and Coker, D., "**Transverse Response of Titanium Aluminide MMCs at Room and Elevated Temperatures**," Technical Report UDRI-TR-91-50, University of Dayton Research Institute, Ohio, 45469, April 1991.

Larsen, J.M., Williams, K.A., Balsone, S.J., and Stucke, M.J., **"Titanium Aluminides for Aerospace Applications,"** *High Temperature Aluminides and Intermetallics*, C.T. Liu, D.G. Pettifor, D.P. Pope, V.K. Sikka, J.O. Stiegler, S.H. Wang, and M. Yamaguchi, Eds., TMS/ASM International, Warrendale, PA, 1990, pp. 521-556.

Luh, E.Y., Dauskardt, R.H. and Ritchie, R.O., **"Cyclic Fatigue-Crack Growth Behavior of Short Cracks in SiC-Reinforced Lithium Aluminosilicate Glass-Ceramic Composite,"** *Journal of Materials Science*, Vol. 9, September 1990, pp. 719-725.

Luk, V.K. and Keer, L.M. **"Stress Analysis for an Elastic Half Space Containing an Axially-Loaded Ridge Cylindrical Rod,"** *International Journal of Solids and Structures*, Vol. 15 1979, pp. 805-827.

MacKay, R.A., Brindley, P.K. and Froes, F.H., **"Continuous Fiber-Reinforced Titanium Aluminide Composites,"** *The Journal of The Minerals, Metals and Materials and Society, JOM*, Vol. 43, No. 5, May 1991, pp. 23-29.

Majumdar, B.S. and Newaz, G.M., **"Thermo-mechanical Fatigue of an Angle-Ply Metal Matrix Composite,"** Presented at ASTM Third Symposium on Composite Materials: Fatigue and Fracture, Orlando, FL, ASTM STP 1110, November 1989.

Mendelson, A., *Plasticity: Theory and Application*, Robert E. Krieger Publishing Co., Florida, 1968.

Mikata, Y. and Taya, M., **"Stress Field in a Coated Continuous Fiber Composite Subjected to Thermo-Mechanical Loadings,"** *Journal of Composite Materials*, Vol. 19, November 1985, pp. 554-578.

Muki, R. and Sternberg, E., **"On the Diffusion of an Axial Load from an Infinite Cylindrical Bar Embedded in an Elastic Medium,"** *International Journal of Solids and Structures*, Vol. 5, 1969, pp. 587-605.

Munro, S.D. and Ashbaugh, N.E., **"Stress Analysis of Metal Matrix Composite Subject To Thermal Loading,"** Technical Report UDRI-TR-91-48, University of Dayton Research Institute, Ohio, 45469, April 1991.

Munu, C., **"Complete Quadratic Isoparametric Finite Elements in Fracture Mechanics Analysis,"** *International Journal for Numerical Methods in Engineering*, Vol. 21, 1985, pp. 1547-1553.

Newman, J.C., Jr., **"Crack-Opening Displacements in Center-Crack, Compact, and Crack-Line Wedge-Loaded Specimens,"** NASA TN D-8268, National Aeronautics and Space Administration, Washington, DC, July 1976.

Nicholas, T. and Ashbaugh, N.E., **"Fatigue Crack Growth at High Load Ratios in the Time-Dependent Regime,"** *Fracture Mechanics: Nineteenth Symposium, ASTM STP 969*, T.A. Cruse, Ed., American Society for Testing and Materials, Philadelphia, PA, 1988, pp. 800-817.

Pagano, N. J. and Tandon, G. P., **"Elastic Response of Multi-Directional Coated Fiber Composites,"** *Composites Science and Technology*, Vol. 31, 1988, pp. 273-293.

Parida, B.K. and Nicholas, T., **"Growth of Fatigue Cracks Emanating from Notches in Titanium Aluminide,"** Proceedings International Conference on Fracture of engineering Materials and Structures, FEFG-ICF, 1991, pp. 685-690.

Porter, W.J., III, **"Crack Initiation in Beta Titanium Alloy Castings,"** Thesis, Submitted to Graduate Engineering and Research School of Engineering, University of Dayton, Dayton, Ohio, July 1990.

Prewo, K.M. and Kreider, K.G., **"The Transverse Tensile Properties of Boron Fiber Reinforced Aluminum Matrix Composites,"** *Metal Trans.* Vol 3, August 1972, pp. 2201-2211.

Reece, M.J., Guio, F. and Sammur, M.F.R., **"Cyclic Fatigue Crack Propagation in Alumina under Direct Tension-Compression Loading,"** *Journal of American Ceramic Society*, Vol. 72, No. 2, February 1989, pp. 348-352.

Revelos, W. C. and Smith, P. R., **"Effect of Environment on the Thermal Fatigue Response of a Ti-24Al-11Nb/SCS-6 Composite,"** Published in *Met. Trans.*, Vol 23A, February 1992.

Rice, J.R., **"Some Remarks on Elastic Crack Tip Fields,"** *International Journal of Solids and Structures*, Vol. 8, 1972, pp. 751-758.

Ritter, R.O. and Ritchie, G.G., **"On the Calibration, Optimization and use of d.c. Electric Potential Methods for Monitoring Mode III, Crack Growth in Torsionally-loaded Samples,"** *Mat. and Struct.*, Vol. 5, No. 1, 1982, pp. 91-99.

Russ, S.M., **"Thermal Fatigue of Ti-24Al-11Nb/ SCS-6,"** *Metall. Trans.*, Vol. 21 A, 1990, pp. 1595-1602.

Russ, S.M. and Nicholas, T., **"Thermal and Mechanical Fatigue of Titanium Aluminide Metal Matrix Composites,"** *Titanium-Aluminide Composites*, WL-TR-91-4020, P.R. Smith, S.J. Balsone, and T. Nicholas, Eds., WPAFB, Ohio, April 1991.

Russ, S.M. and Nicholas, T., **"Thermomechanical Fatigue of SCS-6/Ti-24Al-11Nb Metal Matrix Composite,"** To be Published in the Proceedings of ASME Symposium, Atlanta, Georgia, December, 1991.

Russ, S.M., Nicholas, T., Bates, M., and Mall, S., **"Thermomechanical Fatigue of SCS-6/Ti-24Al-11Nb Metal Matrix Composite,"** To be submitted to ASTM, 1991 ASME Winter Annual Meeting.

Saouma, V.E. and Schwemmer, D. **"Numerical Evaluation of the Quarter Point Crack Tip Element,"** *International Journal for Numerical Methods in Engineering*, Vol. 20, 1984, pp. 1629-1641.

Saxena, A. and Hudak, S.J., Jr., **"Review and Extension of Compliance Information for Common Crack Growth Specimens,"** *International Journal of Fracture*, Vol.14, October 1978, pp. 453-468.

Sharpe, W.N., Jr., **"Interferometric Surface Strain Measurement,"** *International Journal of Non-Destructive Testing*, Vol. 3, 1971, pp. 59-76.

Sharpe, W.N., Jr., Jira, J.R., and Larsen, J.M., **"Real-Time Measurement of Small-Crack Opening Behavior Using an Interferometric Strain/Displacement Gage,"** *Small-Crack Test Methods*, ASTM STP 1149, J. Larsen and J. Allison, Eds., American Society for Testing and Materials, Philadelphia, PA, To be published, June 1992.

Sherwood, J.A., **"Constitutive Modeling of Metal Matrix Composites,"** Final report to University of Dayton Research Institute, July 1991.

Shetty, D.K., Rosenfield, A.R., and Duckworth, W.H., **"Mixed-Mode Fracture of Ceramics in Diametral Compression,"** *Journal of the Ceramic Society*, Vol.69, No. 6, June 1986, pp. 437-443.

Sundar, R. and Dask, P.K., **"Measurement of Fatigue Crack Closure Through Electron Microscopy,"** *International Journal of Fatigue*, April 1982, pp. 97-105.

Sundar, R., **"Fractographic Observations of Fatigue Crack Closure in an Al-Cu-Alloy,"** *Project Document ST 8902*, National Aeronautical Laboratory, Bangalore 560 017, India, January 1989.

Srawley, J.E., **"Wide Range Stress Intensity Factor Expressions for ASTM Method E399 Standard Fracture Toughness Specimens,"** *International Journal of Fracture*, Vol. 12, 1976, pp. 475-476.

Sun, C. T., Chen, J. L., Shah, G. T., and Koop, W. E., **"Mechanical Characterization of SCS-6/Ti-6-4 Metal Matrix Composite,"** *J. Composite Materials*, Vol. 24, October 1990, pp. 1029-1059.

Tada, H., Paris, P.C., and Irwin, G.R., **The Stress Analysis of Cracks Handbook**, Del Research Corporation, Hellertown, PA, 1976.

Tan, P.W., Raju, I.S., and Newman, J.C., Jr., **"Boundary Force Method for Analyzing Two-Dimensional Cracked Bodies,"** NASA Technical Memorandum 87725, National Aeronautics and Space Administration, Langley Research Center, Hampton, Virginia, May 1986.

Tan, P.W. and Newman, J.C., Jr. of NASA Langley Research Center, Private communication with G.L. Petrak (WL/MLSE) USAF Materials Directorate, 9 February 1987.

Timoshenko, S. P. and Goodier, J. N., *Theory of Elasticity*, McGraw-Hill, 1970.

Titanium Aluminide Composites, Third Interim report for contract F33657-86-C-2136 submitted by GE to Material Laboratory Air Force Aeronautical Laboratories, Wright-Patterson AFB, Oh, 45433, September 1988.

Tsai, S.W., "**Composites Design**," Think Composites, Dayton, Ohio, 1988.

Tweed, J., Das, S.C., and Rooke, D.P., "**The Stress Intensity Factors of a Radial Crack In a Finite Elastic Disc**," *International Journal of Engineering Science*, Vol. 10, 1972, pp. 323-335.

Vedula, M., Pangborn, R.N., and Queeney, R.A., "**Fiber Anisotropic Thermal Expansion and Residual Thermal Stress in a Graphite/Aluminium Composite**," *Composites*, Vol. 19, No. 1, January 1988, pp. 55-60.

Wang, Y. and Petroski, H.J., "**Fatigue Crack Propagation In Concrete**," *International Journal of Fracture*, Vol. 41, 1989, pp. R55-R58.

Ward, C. H., Williams, J. C., Thompson, A. W., Rosenthal, D. G. and Froes, F. H., "**Fracture Mechanics in Titanium Aluminide Intermetallics**," *Memoires et Etudes Scientifiques Revue de Metallurgie*, Vol. 86, No. 10, October 1989, pp. 647-653.

Wisnom, M. R., "**Factors Affecting the Transverse Tensile Strength of Unidirectional Continuous Silicon Carbide Fiber Reinforce 6061 Aluminum**," *Journal of Composite Materials*, Vol. 24, July 1990, pp. 707-727.

Yarema, S.Y., Ivanitskya, G.S., Maistrenko, A.L, and Zboromirskii, A.I., "**Crack Development in a Sintered Carbide in Combined Deformation of Types I and II**," *Problemy Prochnosti*, No. 8, 1984, pp. 51-56.

Zawada, L.P., "**Effect of Temperature, Frequency and Hold Time on Fatigue Crack Propagation in Ti-Alloy IMI-834**," Thesis, to be submitted to Graduate Engineering & Research School of Engineering, University of Dayton, April 1992.